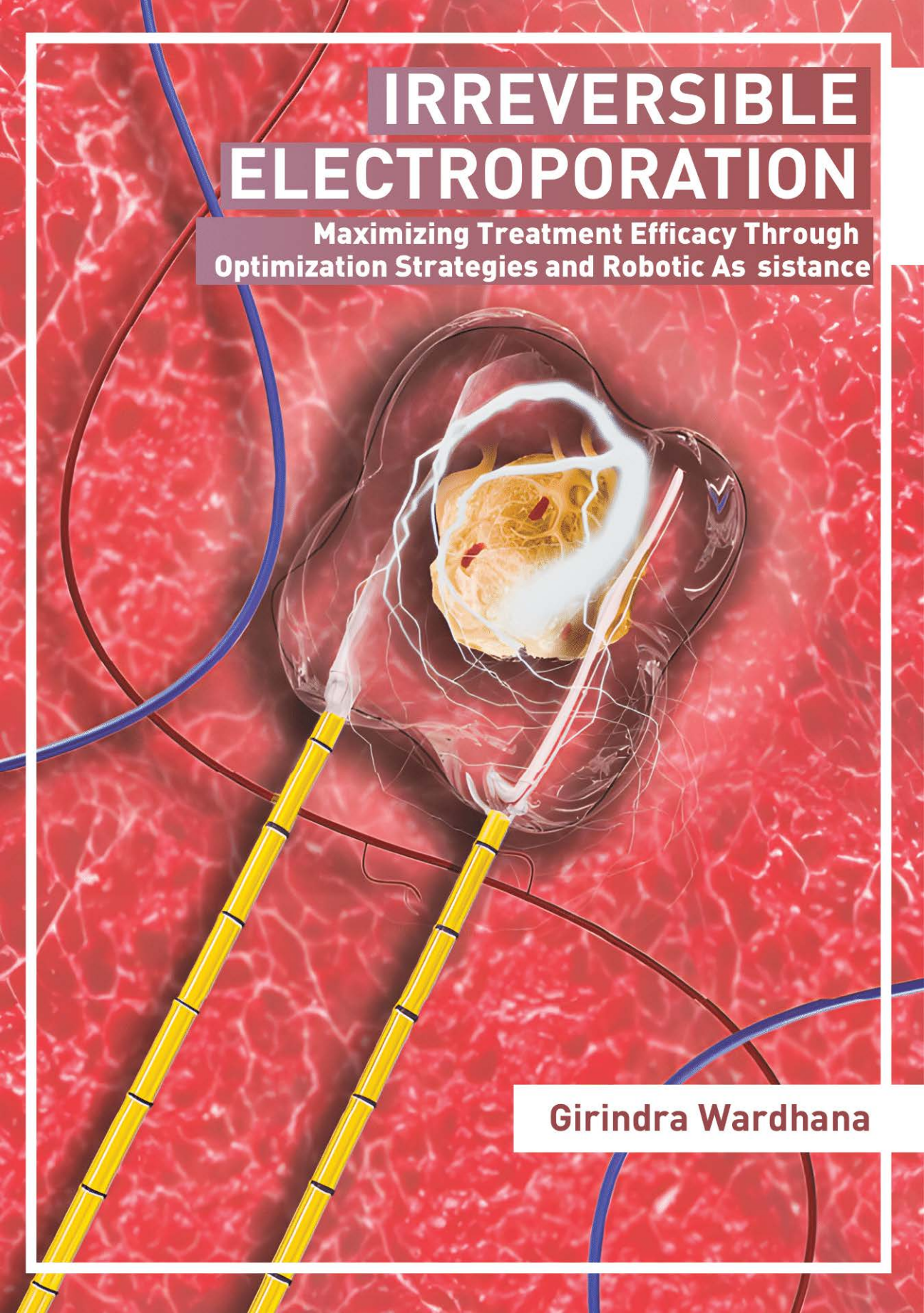


IRREVERSIBLE ELECTROPORATION

Maximizing Treatment Efficacy Through
Optimization Strategies and Robotic Assistance



Girindra Wardhana

**IRREVERSIBLE ELECTROPORATION:
MAXIMIZING TREATMENT EFFICACY
THROUGH OPTIMIZATION STRATEGIES
AND ROBOTIC ASSISTANCE**

Girindra Wardhana

IRREVERSIBLE ELECTROPORATION: MAXIMIZING TREATMENT EFFICACY THROUGH OPTIMIZATION STRATEGIES AND ROBOTIC ASSISTANCE

DISSERTATION

to obtain

the degree of doctor at the University of Twente,

on the authority of the rector magnificus,

prof. dr. ir. A. Veldkamp,

on account of the decision of the Doctorate Board

to be publicly defended

on Tuesday 4 July 2023, at 12.45 hours

by

Girindra Wardhana

born on the 27th of November, 1992

in Praya, Indonesia

This dissertation has been approved by:

Supervisor

prof. dr. ir. J.J. Fütterer

Co-supervisor

dr. ir. M. Abayazid

Cover design: Viriega Fauzia. R.

Printed by: IPSKAMP Printing, Enschede, The Netherlands

ISBN (print): 978-90-365-5674-3

ISBN (digital): 978-90-365-5675-0

URL: <https://doi.org/10.3990/1.9789036556750>

©2023, Girindra Wardhana, The Netherlands. All rights reserved. No parts of this thesis may be reproduced, stored in a retrieval system or transmitted in any form or by any means without permission of the author. Alle rechten voorbehouden. Niets uit deze uitgave mag worden vermenigvuldigd, in enige vorm of op enige wijze, zonder voorafgaande schriftelijke toestemming van de auteur.

Graduation Committee:

Chair / secretary:	prof.dr. J.N. Kok
Supervisor:	prof.dr.ir. J.J. Fütterer Universiteit Twente, EEMCS, Robotics and Mechatronics
Co-supervisor:	dr. M. Abayazid Universiteit Twente, EEMCS, Robotics and Mechatronics
Committee Members:	prof.dr.ir. S. Stramigioli Universiteit Twente, EEMCS, Robotics and Mechatronics prof.dr.ir. H. van der Kooij Universiteit Twente, ET, Biomechatronics and Rehabilitation Technology prof.dr. J. Dankelman TU Delft prof.dr. M. Meijerink Amsterdam UMC dr. J.M. Wolterink Universiteit Twente, EEMCS, Mathematics of Imaging AI



**UNIVERSITY
OF TWENTE.**

The work described in this thesis was carried out in the
Robotics and Mechatronics Group
Faculty of Electrical Engineering, Mathematics and Computer Science
University of Twente, P.O. Box 217,
7500 AE Enschede, The Netherlands.

This work was funded by CMI exploitation Grant.

Summary

Irreversible electroporation is a non-thermal ablation technique that uses an electric field to destroy tumor cells. Compared to thermal ablation methods, irreversible electroporation causes cell death mainly through apoptosis, preserves surrounding tissue, and is not affected by local blood flow. However, because of the varying properties of target tissues, the optimal parameters for irreversible electroporation treatment are still under investigation. To address this challenge, various studies have developed computational models for finding optimal irreversible electroporation protocols that cover the entire tumor region while avoiding unwanted thermal injury.

Electrode placement during irreversible electroporation treatment is a significant challenge for clinicians, with the number of electrodes utilized ranging from two to six, and the distance between each of the electrode pair preferably between 10 and 25 mm. To aid with this task, robotic applications are becoming increasingly popular in assisting clinicians with electrode placement in irreversible electroporation treatment. Studies have shown that robots can reduce intervention time, minimize radiation exposure, and achieve equal or even higher accuracy compared to manual placement.

This thesis presents computational models to investigate the optimal irreversible electroporation protocol by examining the effects of pulse parameters and electrode configurations on the ablation area and thermal damage to the target tissue. Model validation has been conducted on animal and vegetable tissue, with in-depth discussions offered in Chapters 2 and 3. To improve the accuracy of the model, the actual shape of the tissue should be considered during the simulation process. Therefore, an automatic segmentation method using deep learning was proposed to segment liver and tumors from CT images, offering high accuracy and faster processing times compared to manual segmentation, as elaborated in Chapter 4.

Robotic systems have been developed to assist clinicians with the placement of multiple electrodes in target tissues. Two robot designs were proposed and fabricated using 3D printing with plastic material. They were actuated using a pneumatic system, making them suitable for use within an MRI scanner. The initial robot design had four degrees of freedom, and multiple electrode insertions were carried out sequentially while taking into account the orientation of previous electrodes to maintain parallelism between them. The second robot design is an improvement on the first robot, with a grid system employed to accommodate the insertion of multiple electrodes simultaneously while maintaining the distance and parallelism between electrodes. This design has two degrees of freedom, which simplifies robot control and installation by requiring fewer pneumatic tubes. Chapters 5 and 6 present the designs and evaluations of the robot performances. Both designs have demonstrated limited deviation within the acceptable range for irreversible electroporation procedures. The robotic systems have great potential to assist clinicians in accurately placing multiple electrodes into target tissues, ultimately improving treatment outcomes.

In conclusion, the tools proposed in this thesis, including computational models and robotic systems, contribute to the improvement of treatment efficacy using irreversible electroporation. These tools can aid clinicians in developing more patient-specific models, improving treatment planning outcomes, and assisting in electrode placement accuracy.

Samenvatting

Irreversibele elektroporatie (IRE) is een niet-thermische ablatietechniek die een elektrisch veld gebruikt om tumorcellen te vernietigen. In vergelijking met thermische ablatiemethoden veroorzaakt IRE voornamelijk celdood door apoptose, geen schade aan het omliggende weefsel en wordt het niet beïnvloed door de lokale bloedstroom. Vanwege de verschillende eigenschappen van weefsels zijn de optimale parameters voor IRE-behandeling echter nog onderzocht. Om deze uitdaging aan te gaan zijn in diverse studies computermodellen ontwikkeld om optimale IRE-protocollen te vinden die het gehele tumorgebied bestrijken en tegelijkertijd ongewenste thermische schade voorkomen.

De plaatsing van elektroden tijdens IRE-behandelingen is een grote uitdaging voor klinici, waarbij het aantal gebruikte elektroden varieert van twee tot zes naalden en de afstand tussen elk elektrode paar bij voorkeur tussen 10 en 25 mm ligt. Om deze taak te ondersteunen worden robottoepassingen steeds populairder om klinici te helpen bij het plaatsen van elektroden tijdens IRE-behandelingen. Studies hebben aangetoond dat robots de interventietijd kunnen verkorten, de blootstelling aan straling kunnen minimaliseren en een gelijke of zelfs hogere nauwkeurigheid kunnen bereiken in vergelijking met handmatige plaatsing.

Deze thesis presenteert computermodellen om het optimale IRE-protocol te onderzoeken door de effecten van puls parameters en elektrodeconfiguraties op het ablatiegebied en thermische schade aan het doelweefsel te onderzoeken. Modelvalidatie is uitgevoerd op dierlijk en plantaardig weefsel, met diepgaande besprekingen in hoofdstuk 2 en 3. Om de nauwkeurigheid van het model te verbeteren, moet tijdens het simulatieproces rekening worden gehouden met de werkelijke vorm van het weefsel. Daarom werd een automatische segmentatiemethode met behulp van deep learning voorgesteld om zowel de lever als de lever tumoren op CT-beelden te segmenteren, met hoge nauwkeurigheid en snellere verwerkingstijden dan bij handmatige segmentatie, zoals beschreven in Hoofdstuk 4.

Robotsystemen zijn ontwikkeld om clinici te helpen bij het plaatsen van meerdere elektroden in doelweefsels. Twee robotontwerpen werden voorgesteld en vervaardigd door middel van 3D-printen met plastic materiaal. De robots werden aangedreven door een pneumatisch systeem, waardoor ze geschikt waren voor gebruik binnen een MRI-scanner. Het eerste robotontwerp had vier vrijheidsgraden en meerdere elektrode-inserties werden achtereenvolgens uitgevoerd, waarbij rekening werd gehouden met de oriëntatie van de vorige elektroden om onderling parallelisme te behouden. Het tweede robotontwerp is een verbetering ten opzichte van de eerste robot, waarbij een rastersysteem wordt gebruikt om meerdere elektroden tegelijk in te brengen, met behoud van de afstand en het parallelisme tussen de elektroden. Dit ontwerp heeft twee vrijheidsgraden, wat de robotbediening en installatie vereenvoudigt doordat er minder pneumatische buizen nodig zijn. In hoofdstuk 5 en 6 worden de ontwerpen en evaluaties van de robotprestaties gepresenteerd. Beide ontwerpen hebben een beperkte afwijking aangetoond binnen het aanvaardbare bereik voor IRE-procedures. De robotsystemen hebben een groot potentieel om clinici te helpen bij het nauwkeurig plaatsen van meerdere elektroden in de doelweefsels, wat uiteindelijk tot betere behandelingsresultaten zal leiden.

Concluderend dragen de tools die in dit proefschrift worden voorgesteld, waaronder computermodellen en robotsystemen, bijdragen aan de verbetering van de doeltreffendheid van de behandeling met irreversibele elektroporatie. Deze tools kunnen clinici helpen bij het ontwikkelen van meer patiënt specifieke modellen, het verbeteren van de resultaten van de behandelplanning en het helpen bij het nauwkeurig plaatsen van elektroden.

Published work

Journal Articles

1. G. Wardhana, N. M. Raman, M. Abayazid, J.J. Fütterer. "Investigating the effect of electrode orientation on irreversible electroporation with experiment and simulation". In: *International Journal of Computer Assisted Radiology and Surgery*, 17(8):1399–1407, (2022).
2. G. Wardhana, J. P. Almedia, M. Abayazid, J.J. Fütterer. "Development of a thermal model for irreversible electroporation: an approach to estimate and optimize the IRE protocols". In: *International Journal of Computer Assisted Radiology and Surgery*, 16(8):1325–1334, (2021).
3. G. Wardhana, M. Abayazid, J. J. Fütterer. "Toward reliable automatic liver and tumor segmentation using convolutional neural network based on 2.5D models". In: *International Journal of Computer Assisted Radiology and Surgery*, 16:41–51, (2021).

Conference Proceedings

1. G. Wardhana, Y. X. Mak, M. Abayazid, J.J. Fütterer. "Design and Characterization of a Multiple Needle Insertion MRI-guided Robot for Irreversible Electroporation (IRE) Treatment". In: *2022 9th IEEE RAS/EMBS International Conference for Biomedical Robotics and Biomechatronics (BioRob)*, pages:1–6, (2022).
2. G. Wardhana, A. L. V. Tizatl, M. Abayazid, J.J. Fütterer. "Automatic trajectory planning for IRE treatment in liver tumours A numerical study". In: *8th Dutch Bio-Medical Engineering Conference, BME 2021*, (2021).
3. G. Wardhana, H. Naghibi, B. Sirmacek, M. Abayazid. "Liver Classification Implementation For Fast Automatic Liver Segmentation in CT Scan Images". In: *25th Congress of the European Society of Biomechanics*, 25, (2019).

In Preparation

1. G. Wardhana, J.J. Fütterer, M. Abayazid. "IRE Made Easy: Introducing the Robotic Grid System for Multiple Parallel Needle Insertion in Irreversible Electroporation Treatment". *In Preparation*.

Patent

1. G. Wardhana, M. Abayazid, J.J. Fütterer. "MRI compatible robotic device for ablation treatment". (2022).

To my wife, daughter, parents

Contents

Summary	vii
Samenvatting	ix
Published work	xi
1 Introduction	1
1.1 Introduction	3
1.2 IRE Protocols	5
1.3 Robotic approach of IRE treatment	8
1.4 Aim and outline of the thesis	10
2 Development of a Thermal Model for Optimizing IRE Protocols	13
2.1 Introduction	15
2.2 Related Work	16
2.3 Methods	17
2.4 Results	21
2.5 Discussion	28
2.6 Conclusion and Future Research	30
3 Investigating the Effect of Electrode Orientation on IRE	33
3.1 Introduction	35
3.2 Related Work	36
3.3 Methods	37
3.4 Results	44
3.5 Discussion	48
3.6 Conclusions and Future Work	51
4 Liver and Tumor Segmentation Using Deep Learning	53
4.1 Introduction	55
4.2 Materials and Methods	57
4.3 Result and Discussion	64

4.4	Conclusion	72
5	Design and Characterization of an MRI-Guided Robot for IRE	73
5.1	Introduction	75
5.2	Methodology	77
5.3	Experiments and Results	83
5.4	Conclusion	88
6	Robotic Grid System for Parallel Needle Insertion in IRE	89
6.1	Introduction	91
6.2	Methodology	93
6.3	Experiments	97
6.4	Results	101
6.5	Discussion	104
6.6	Conclusion	107
7	General Discussion and Conclusion	109
7.1	Computational Model	112
7.2	Robotic device	116
7.3	Future recommendation toward clinical practice	120
7.4	Conclusion	121
	Bibliography	123
	Acknowledgments	145
	About the author	149

1

Introduction

Irreversible Electroporation (IRE) is one of the available minimally invasive procedures that is used in tumor treatment. It is a non-thermal ablation technique that uses an electric field instead of heat to destroy tumor cells. This is achieved by delivering a series of high-voltage pulses using electrode pairs that are inserted into the surrounding tissue of the target tissue. The process of exposing tumor cells to an electric field is called electroporation, which increases the permeability of the cell membrane. When a specific threshold is exceeded, the electric field irreversibly alters the structure of the cell membrane, resulting in cell death. The phenomenon of inducing tumor cell death using an electric field is referred to as irreversible electroporation.

1.1 Introduction

Electroporation has been a topic of research for many years, particularly due to its impact on the permeability of cell membranes. When an intense electric field is applied to the cell membrane, it increases its permeability. The effect of electroporation on the cell membrane differs depending on the intensity of the electric field and the duration of the pulse. It can range from having no effect at all, to reversibly opening the cell membrane while keeping cell viability, or irreversibly opening the cell membrane, resulting in cell death [1].

At the end of the 20th century, electroporation was increasingly used in different applications, particularly in the medical and food industry. In the fields of medical and biological science, electroporation has been employed for diverse applications, including drug delivery (electrochemotherapy) [2, 3], cell fusion (electrofusion) [4], and DNA transfer (electrotransfer) [5]. Meanwhile, the food industry has adopted electroporation in many aspects of food processing, such as drying, nutrient extraction, and food preservation [6, 7].

In 2005, a study introduced the application of irreversible electroporation as a non-thermal ablation method for tumor ablation [8]. Through a computational model, the researchers demonstrated the effectiveness of IRE, showing results comparable to those of other thermal ablation techniques. The ablation method with IRE involves exposing cells to an intense electric field, generating permeable nanopores in the cell membrane. When the electric field

reaches a certain threshold, the membrane undergoes an irreversible process, permanently opening the pores. This disrupts the cell's homeostasis state, leading to cell death via apoptosis [9].

IRE can theoretically be considered a non-thermal ablation method as it utilizes electrical energy to destroy cells. However, it is important to note that temperature may increase during the procedure, particularly in areas near the electrodes. In addition, if electrodes are not placed in parallel, there is a risk of overcurrent occurring in the area where electrodes are positioned near each other, leading to an increase in temperature [10]. This may result in undesired thermal damage to the tissue if the temperature exceeds a certain threshold. Thermal damage can occur at temperatures above 42°C, particularly if the cells are exposed for an extended period, ranging from seconds to hours [8]. At temperatures between 50-60°C, the rate of thermal damage significantly increases [11]. Therefore, careful planning of IRE treatment is essential to minimize the risk of thermal damage to exposed tissue.

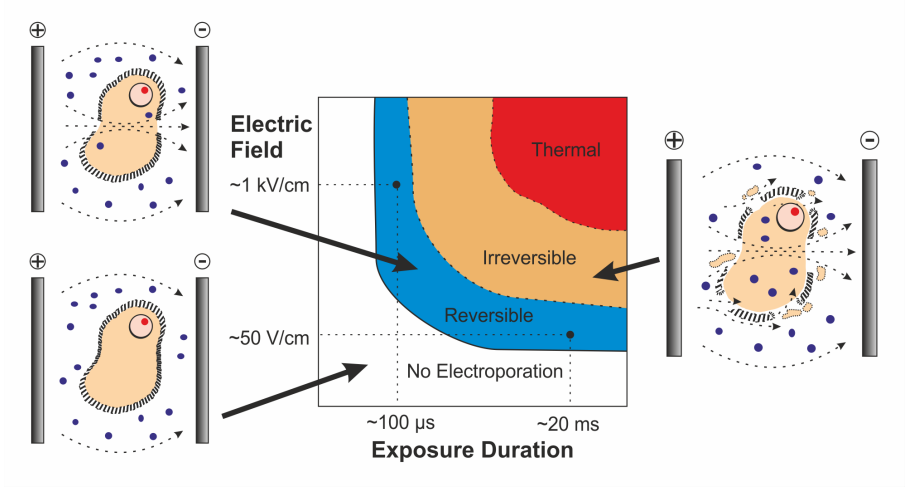


Figure 1.1: Degree of electroporation, including reversible, irreversible, and thermal damage, as a factor of electric field and exposure duration.

Before the implementation of IRE in clinical practice, common modalities for tumor ablation were based on thermal energy. Focused ultrasound uses high-intensity ultrasound beams to introduce high temperature to the undesirable tissue, causing coagulation of the tumor cell. Other techniques use an active electrode inserted into the tissue to heat and destroy cancer cells. The thermal energy source comes from either microwave energy in the microwave ablation method or high-frequency alternating current in radio-frequency ablation. Tumors can also be treated by cooling the tissue to less than -40°C , as in the cryoablation technique. The cooling gas is distributed using a hollow probe that is inserted into the tissue, causing the tissue to freeze and necrosis.

All of these treatment techniques utilize thermal, either extremely hot or cold, to kill tumor cells through necrosis. These techniques are easy to apply, where generally only one needle is required, and the affected area can be easily monitored. However, incomplete ablation may occur, especially in the area close to larger vascular structures due to heat dissipation caused by blood flow (heat sink effect) [12]. Additionally, thermal ablation may cause damage to adjacent structures, which makes it difficult to apply if the tumor is located near vital structures such as veins, arteries, or bile ducts [13].

In contrast to thermal ablation, IRE is independent of thermal energy, where cell death mainly occurs through apoptosis, rather than necrosis. Its effectiveness is not affected by the local blood flow, making it a preferable choice when treating tumors located near blood vessels. Additionally, the ablation area in IRE is determined by the distribution of the electric field to tissue with an electroporation threshold below the applied electric field. This makes IRE a safer choice for preserving connective tissue, nerves, and vessels close to the tumor [14].

1.2 IRE Protocols

Many studies have investigated the optimal parameters for IRE to maximize non-thermal damage and avoid thermal damage [15, 16, 17, 18]. Two main factors that affect the electric field distribution during IRE treatment are considered in IRE protocols: pulse parameters and electrode configuration. Pulse

parameters include pulse strength, pulse shape, pulse duration, and the number of pulses. Other studies have also investigated the effect of pulse delay on treatment efficacy [19, 20]. For electrode configuration, most studies have investigated the electric field distribution in relation to the placement and number of electrodes [21, 22, 23]. In the case of a large tumor, more than two needles are required to completely ablate the tumor. Furthermore, the design of the electrode has been discussed to ensure that the electric field can cover the entire targeted tissue [24].

During IRE therapy, the voltage delivered typically ranges from 1400 to 2000 V, but it can go up to 3000 V depending on the distance between the electrodes. Square waves have been shown to be more effective for electroporation compared to sine waves or other waveforms. The application of square waves can take various forms, including unipolar, bipolar, and asymmetric pulses [25]. The pulse duration is normally around 50-100 μs with 80-100 pulses per treatment cycle. Although IRE has been studied for over a decade, a standard protocol is yet to be established, given that different target tissues where IRE is applied have different properties [26]. In clinical practice, most studies have reported using 90 pulses per treatment cycle, with a pulse duration of 70-90 μs and a voltage ratio of 1500-1700 V/cm [27, 28].

In terms of electrode placement, the number of electrodes used in IRE treatment varies from two to six electrodes. All electrodes should preferably be positioned in parallel, while the distance between the needle should be within 10-25 mm. If the electrode is angulated, there is a high risk of overcurrent in the area where the electrodes are close to each other. It can cause a rise in temperature and thermal damage to the tissue. On the other hand, if the electrodes are too far apart, there is a risk of incomplete ablation in some regions where the electric field does not cover. It is important to note that during needle placement, there should be a 2 mm distance from large vessels to avoid high temperatures in the surrounding area of the electrode, which can cause damage and risk of burn [29].

Electrode design is an important aspect to consider during IRE treatment. In general, four major types of electrodes are used in IRE, including plate, clamp, needle, and catheter [30].

The plate model uses two parallel plates inserted into the targeted tissue. It allows for the maintenance of a homogeneous distribution of the electric field generated. However, it is not commonly used in practice due to the difficulty of placement. It is considered invasive and is typically only implemented during open surgery treatment. The clamp model has similar characteristics to the plate model, with the cathode and anode located inside the clamp surface. This model can hold the target tissue and provide secure contact compared to the plate model. However, it is still considered an invasive type and is normally only used in open surgery on specific target tissue such as arteries or intestines.

The needle model is the most common type of electrode used in IRE treatment. With a needle-shaped electrode, it can be easily manipulated and becomes less invasive. However, the electric field is not homogeneously distributed and requires proper planning software to calculate the coverage area of the treatment. Additionally, multiple electrodes are required when the treatment area becomes larger. The catheter model is a type of electrode that is inserted into the targeted tissue via a catheter. It is considered the least invasive compared to other models, but it requires more skill to manipulate and navigate the electrode to the target location.

Proper treatment planning is necessary for the use of the needle-shaped electrode to determine the distribution of the electric field. Unlike thermal-based methods, the coverage area in IRE does not create a spherical shape and multiple needles need to be positioned near the tumor to cover the cancerous tissue with an electric field. Depending on the size and shape of the tumor, the number of inserted needles may increase from 2 to 6 needles. This is the primary technical complexity compared to other thermal ablation techniques.

Numerous studies have been conducted to develop computational models that optimize pulse parameters to find the right combination that covers the specific tumor region while avoiding unwanted thermal injury. This model is also useful for planning the effective configuration of the electrode placement. The use of computational models in IRE planning is found in various treatments, including kidney [31], liver [32], pancreas [33], and brain [34].

1.3 Robotic approach of IRE treatment

Although IRE has several advantages over other ablation techniques, it is not the preferred choice for most tumor treatments. It is only selected in cases where other methods are not applicable due to the anatomical position of the tumor, tumor type (pancreas), or when the results of other treatments are not showing improvement. The main challenge of IRE is the positioning of multiple electrodes in parallel. With only one pair of electrodes, IRE is only able to destroy tumors smaller than $< 1 \text{ cm}^3$ without repositioning [30]. To treat larger volumes, increasing the electric field coverage by raising the voltage or the pulse number and duration may cause thermal damage to other structures due to joule heating. The remaining options are to repeat the treatment by repositioning the needles, which may increase the treatment duration, or to add more needles, which increases the complexity and difficulty of the procedure. The placement of multiple needles needs to be planned carefully to maintain the generated electric field above the IRE threshold and cover the entire tissue region [35].

Apart from planning the treatment parameters and needle placement layout, inserting multiple needles is a challenging process in IRE. It is crucial to ensure that the electrodes are inserted parallel to each other and at a distance of 10-20 mm to prevent thermal damage or incomplete ablation of the tumor. In cases of larger tumors, multiple electrodes need to be precisely placed in the area surrounding or inside the tumor to cover the entire tumor volume. The depth of the needles also needs to be uniform. When the tumor is located in a sensitive structure that makes uniform needle depth difficult, there is a risk of overestimating the ablation area due to the difference in electrode spacing.

Accurate manual insertion requires an experienced physician to perform. In addition, the patient needs to be under total anesthesia and well-fixed to prevent any spontaneous movement due to respiratory motion. Most of the time, manual insertion requires multiple adjustment processes to get the needle into the correct position. This leads to an increase in the radiation dose received by the patient, longer anesthesia times, and an increased chance of surgical complications.

Considering the difficulty of placing the needle in IRE treatment, robotic applications are gaining popularity in assisting clinicians with needle placement. Several studies have shown that a robot can decrease intervention time, lower radiation exposure, and achieve equal or higher needle accuracy. This helps the patient recover faster and reduces the risk of infection, while also providing easier access to hard-to-reach places [36, 37].

Several robots have been reported in the application of IRE, such as Maxio Perfint [38, 36, 39], DaVinci Platform [40], robotic arm [41] and iSYS or Micromate [42]. Some robotic systems, such as Maxio, support the IRE treatment with a software system that can expedite the planning process. This includes identifying tumors, blood vessels, normal tissue, and organs, as well as restricted zones such as blood vessels or vital tissue. In cases where multiple needles are required, the placement of the needles is performed simultaneously, with the parallel insertion being maintained based on the position of the first probe.

Most of the robotic applications mentioned earlier were performed under CT guidance, which is used to verify the location of the needle. With robotic assistance, the number of times the needle needs to be repositioned or readjusted is significantly reduced, thereby reducing the radiation received by the patient [39]. However, the application of robots is still limited due to the high cost, which includes the main robot cost and the cost of disposable items needed for each treatment. Ultimately, the choice of the ablation procedure, whether manual or robot-assisted, depends on the financial capacity of the hospital and the preparation of the medical team.

There is a need for a low-cost robot that is highly versatile and can be used in various types of treatments. Additionally, combining the proposed robotics with other imaging modalities can be advantageous. For example, many studies have developed MRI-compatible robots [43, 44, 45] that can take advantage of the high tissue contrast from MRI images without the use of radiation during the procedure.

1.4 Aim and outline of the thesis

The previous section explained the technical complexities involved in IRE treatment. These include a complex process to obtain optimized IRE parameters and difficulties in placing multiple needles while meeting IRE requirements. We have identified two main research directions related to IRE:

1. The use of a computational model is important in determining the treatment plan for IRE. The main aspects include the configuration of pulse and electrode parameters and the relationship between these parameters, which affect the distribution of the electric field and the risk of thermal damage that may occur when the temperature rises.
2. The development of a robotic device that can assist with multiple needle insertions for IRE treatment. The main requirements for the device are to preserve the parallel positioning of needles and to maintain a specific distance between electrodes within a certain range.

The following research results are presented in the various chapters:

Chapter 2 discusses the relationship between pulse and electrode parameters that are typically used in the IRE procedure. The main objective is to develop a 2D computational model and validate it on animal tissue. Later, the optimal parameters are calculated to obtain the maximum ablation coverage while also keeping the temperature below the thermal damage threshold.

Chapter 3 presents a 3D computational model that was validated in vegetable tissue to predict the ablation volume achieved in IRE. The aim of this study is to observe the effect of non-parallel placements of electrodes on the electric field distribution. While it has been discussed that parallel placement is the preferable position for the electrode, it may not always be the better choice in situations where the tumor is located next to sensitive structures. We investigated the alignment of the electrodes by introducing tilting in the forward and sideward needle orientations, as well as when either one or both needles are tilted. To validate the computational model, we performed IRE treatment on the vegetable tissue with various needle configurations.

Chapter 4 introduces a deep learning network that automatically segments the liver and tumor from CT images. In the previous computational model, the liver and tumor were modeled with simplified shapes, such as boxes and spheres. To improve the accuracy of the computational model, the actual shape of the tissue can be used. Therefore, this study aims to provide a technique for obtaining a realistic shape of the liver and tumor. The deep learning network was tested on the liver tumor segmentation dataset, which consisted of 131 datasets for training and 70 datasets for testing [46]. Later, the model's performance was evaluated by comparing the segmentation result to manual segmentation.

Chapter 5 presents the design of an MRI-safe robot for multiple needle insertion. The robot's body and actuator are made from non-metallic, non-magnetic, and non-conductive materials using 3D printing, making it lightweight and safe to operate inside the MRI bore. The robot has four degrees of freedom and a large robot workspace, which enables it to handle the largest tumor that can be treated using IRE. Multiple needle placement is achieved by simultaneously inserting needles, and the parallel placement is calculated based on the previous needle position. The evaluation of the robot system is performed by conducting several tests, including a needle accuracy test in free air and inside the MRI bore. An MRI compatibility test is also performed by evaluating the image SNR in various robot positions.

Chapter 6 presents the second design of the robot which utilizes a grid system to perform parallel needle insertion. The robot comprises six subgrids that can rotate in two directions, enabling the needle to reach various locations under the robot's body. With this subgrid design, needle insertion can be performed simultaneously while maintaining parallelism during insertion. Two main evaluations were conducted to assess the robot's ability: the accuracy test and the alignment test to keep the needle parallel.

Chapter 7 presents a general discussion regarding the key findings in the developed computational models and robotic devices. In addition, suggestions for future research are included, regarding the further improvement of the robot design and other aspects that need to be tested and evaluated in order to bring the robot towards application in clinical practice.

2

Development of a Thermal Model for Optimizing IRE Protocols

Adapted from: Girindra Wardhana et al. “Development of a thermal model for irreversible electroporation: an approach to estimate and optimize the IRE protocols”. In: *International journal of computer assisted radiology and surgery* 16.8 (2021), pp. 1325–1334.

Abstract

Purpose Irreversible electroporation (IRE) is an emerging technique that has drawn attention in the field of cancer treatment. IRE uses non-thermal electric pulses to induce cell death. However, there have been concerns about the potential tissue heating associated with this technique. This study aims to improve the efficiency of IRE and establish better treatment protocols by investigating optimal IRE protocols that minimize thermal damage during the treatment.

Methods The study focuses on analyzing electrode and pulse parameters. Finite element models are developed to evaluate the ablation area and the temperature changes in the tissue. The model is validated experimentally in bovine liver tissue, while the parameters were optimized using the response surface method (RSM)

Results Analysis of variance reveals that the electrode distance and input voltage significantly influence the temperature rise in the IRE treatment of bovine liver ($P = 0.020$ and $P = 0.003$, respectively). Additionally, only the input voltage significantly affects the ablation area ($P < 0.001$). The optimal results determined by RSM showed that, for achieving a maximum ablation area of 250.82 mm^2 without causing thermal damage, the IRE protocol consisted of an active electrode length of 10 mm, a distance of 10 mm between the electrodes, and the delivery of 50 pulses with a pulse width of $41.21 \text{ }\mu\text{s}$ and an amplitude of 3000 V.

Conclusions This study demonstrates the feasibility of optimizing IRE protocols using the proposed approach. An optimal IRE protocol that maximizes the ablation area was successfully calculated while ensuring no risk of thermal damage to the tissue.

2.1 Introduction

Pancreatic adenocarcinoma is the most common type of pancreatic cancer and ranks as the fourth leading cause of cancer-related deaths in both men and women [48, 49]. This cancer often spreads to other organs, particularly the liver [50]. Over half of the pancreatic cancer patients already have liver metastases at the time of diagnosis [51]. Treatment options for liver metastases are limited, with surgical resection being the primary curative method [52]. However, not all patients are suitable candidates for this type of treatment [53]. Furthermore, due to late diagnosis, most patients present with advanced-stage tumors where resection is no longer feasible [52].

Irreversible Electroporation (IRE) is a minimally invasive surgical procedure that has gained interest in the field of cancer ablation over the last decade. The electroporation technique involves exposing cells to strong electric fields delivered by electrodes inserted into the surrounding soft tissue. If the applied electric field is sufficiently strong, electroporation can become irreversible. This process is characterized by the formation of nanopores in the plasma membrane, which leads to cell death [52, 54].

Theoretically, the process of tissue ablation through IRE can be assumed as non-thermal since it relies on electrical energy to disrupt the cell membrane [52]. However, if the alignment of the electrodes is not maintained during the treatment, there may be an increase in temperature, as described by Van Den Bos et al. [10]. Recent studies have also shown that this technique may result in tissue heating [55, 56]. During IRE, some of the electrical energy delivered to the cells is converted into thermal energy, causing an increase in temperature. If the temperature surpasses a certain threshold, there is a risk of immediate thermal damage to healthy tissue [57]. The rate of damage significantly increases around 50 °C - 60 °C [11], and the amount of thermal damage is typically measured using the Arrhenius equation [58].

Several parameters can influence the outcomes of an IRE treatment. These parameters establish the IRE treatment protocols and are primarily associated with the pulses delivered to the cells (pulse parameters) and the configuration of the inserted electrodes (electrode parameters). The electric field generated

in the tissue and the resulting temperature changed depending on the applied configuration. By adjusting these parameters, it is possible to reduce the thermal effect caused by heating without compromising the ablation process.

Optimizing the IRE protocols is crucial to prevent thermal damage to vital structures near the liver, such as the vasculature, gall bladder, or bile duct [59]. However, the optimal combination of parameters remains unknown, leaving room for improving the efficiency of the IRE method. Consequently, the question arises: *What can we do to optimize the outcomes of an IRE procedure?*

To the best of our knowledge, there are still no defined guidelines regarding the ideal IRE protocols for specific treatments, especially concerning the combination of pulse and electrode parameters. This chapter proposes an approach for calculating optimal IRE protocols by developing an IRE model with experimental validation. The final goal is to present IRE protocols that can maximize the ablation area while minimizing thermal damage during treatment.

2.2 Related Work

This section presents published studies that examine the relationship between IRE parameters, such as electric distribution and thermal development during IRE treatment. Additionally, the proposed approach in this study is described at the end of this section.

During the planning of IRE treatment, multiple parameters are taken into consideration to determine the ablation zone, including electrode and pulse parameters. Various studies have investigated the impact of electrode parameters on IRE treatment. Davalos et al. [8] demonstrated that the electrode diameter affects the maximum voltage that can be applied to the tissue before reaching a temperature of 50 °C. They also observed that electrode shape influences the electric field distribution, with spherical electrodes reaching 50 °C faster than cylindrical electrodes [60]. Yang et al. conducted a study on the influence of four electrode properties (diameter, length, distance between electrode, and electrode number) on the volume of ablated tissue and the maximum temperature generated in liver tissue. The result indicated that only the distance

between the electrodes and the number of electrodes significantly affected the maximum temperature, while only the electrode length significantly impacted the ablation volume [61].

In terms of pulse parameters, Garcia et al. [57] investigated the effect of pulse number on the probability of cell death due to IRE and thermal damage in a 2D liver model using a bipolar electrode. Simulation results showed that thermal damage begins to occur around the electrodes after 30 pulses, and significant tissue damage is observed after 90 pulses. Wandel et al. [16] characterized the effects of pulse number and pulse width in a porcine model, finding that higher pulse numbers and greater pulse widths can increase the ablation zones.

Despite numerous investigations on electrode and pulse parameters in IRE, most studies have considered them separately. However, it is essential to plan both parameters together to achieve the optimal configuration that maximizes the ablation area while minimizing thermal damage. The optimal combination of electrode and pulse parameters is currently unknown.

The present research contributes to the development of an experimentally validated model for adjusting IRE protocols related to electrode and pulse parameters, providing guidance to operators regarding the optimal configuration. An experimental apparatus was developed to validate finite element models for IRE simulation. A series of experiments were designed and conducted using ex vivo bovine liver tissue to validate the models. Temperature measurements were taken and compared to simulation results. If the experimentally measured temperature values align with the values calculated from the models, they can be considered a reliable representation of the real phenomena. Once validated, the models will be utilized to determine the optimal configuration of IRE parameters using Response Surface Methodology (RSM).

2.3 Methods

This section presents the developed models for simulating IRE and the experimental setup and procedure used to validate the models.

2.3.1 Experimental Setup

The experimental setup (Figure 2.1a) includes a transparent cylindrical container (40×150 mm) made of Polymethyl Methacrylate. Fresh bovine liver tissue was purchased from a local butcher store within 24-48 hours after the animal was slaughtered. The liver tissue was not frozen, and therefore, we expect that the conductivity would not be significantly affected. The tissue was used in the experiment after being cut into smaller samples. These samples were placed inside the container, which was then placed in a thermostatic bath to maintain a controlled temperature of 37°C , mimicking body temperature. The pulse generator system Gemini X2 (BTX, Holliston, MA) was connected to two stainless-steel cylindrical electrodes that were inserted in parallel into the bovine liver tissue sample. The pulse generator delivered a series of square pulses, while a high-voltage probe (BTX Enhancer 3000) measured the amplitude of these pulses. The output of the measurements was displayed on a digital oscilloscope RTB2004 (Rohde & Schwarz, Munich, Germany).

Fiber-optic temperature measurement probes, “T1 Fiber Optic Temperature Probe” (Neoptix, Québec, Canada), were inserted into the liver tissue to measure the temperature between the two electrodes. Another fiber-optic probe was inserted 3 mm away from the right electrode, at the same depth as the tip of the electrodes, to monitor the temperature outside the electrodes. Fiber-optic probes were chosen for temperature measurement due to their invulnerability to electromagnetic interference that may occur around the electrode. The actual experimental setup is presented in Figure 2.1b.

2.3.2 Design of the Experiment

Five IRE parameters were tested at different levels. Two cylindrical electrodes were inserted into biological tissue. The distance between electrodes, the applied voltage, the number of pulse repetitions, and the pulse width were evaluated at three levels: low, medium, and high. Additionally, the active length of the electrodes was tested at two different levels: low and high. The different parameter levels in this study are presented in Table 2.1 and Figure 2.1c. The frequency of pulse delivery was set at 1 Hz.

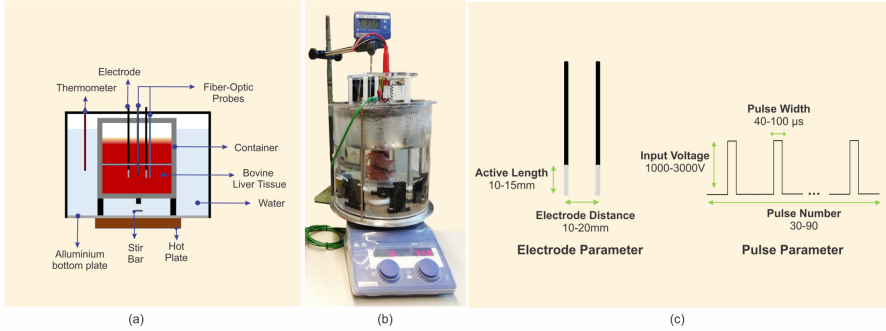


Figure 2.1: (a) The schematic representation of the experimental setup for model validation. Temperatures from three different locations were measured: (1) between the electrodes and (2) outside the electrodes using fiber-optic probes, and (3) water temperature using a thermometer. (b) The actual experimental setup. (c) Electrode and pulse parameters that were tested in the experiment.

2.3.3 Finite Element Models

Finite element models were created to analyze the impact of the IRE parameters on the electric field and temperature responses. The finite element models were computed using COMSOL Multiphysics v.5.4 (Burlington, MA, USA). The geometry consisted of a 2D longitudinal section perpendicular to the two electrodes inserted into bovine liver tissue. The Finite Element Method (FEM) was employed to solve the mathematical models. The mesh was automatically generated by COMSOL with custom sizes for each domain. For the liver and electrodes domains, the maximum element size was set to 3.3 mm and 1 mm respectively, while the minimum element size was set to 3.1 mm and 0.8 mm, respectively. The elements had a triangular shape. The number of elements for each electrode configuration is presented in Table 2.2.

The electric field (EF) distribution in the liver was determined using the Laplace equation:

$$\nabla^2 \cdot V = 0 \quad (2.1)$$

Table 2.1: Various IRE parameters with different configuration levels

Level	Active length (mm)	Distance between electrodes (mm)	Input voltage (V)	Pulse repetitions	Pulse width (μ s)
1	10	10	1000	30	40
2	15	15	2000	60	70
3	-	20	3000	90	100

Table 2.2: The number of elements for each electrode configuration

Distance between electrodes (mm)	Active length (mm)	Number of elements
10	10	16,974
10	15	17,160
15	10	18,481
15	15	18,579
20	10	19,440
20	15	19,600

To model heat transfer within the biological tissue, the Bioheat Transfer Equation was considered:

$$\rho c_p \frac{\partial T}{\partial t} + \rho c_p u \cdot \nabla T + \nabla \cdot q = Q_s + Q_{bio} \quad (2.2)$$

being ρ , c_p and T the density, heat capacity, and temperature of the tissue, respectively, and q the heat flux by conduction in the tissue. Q_s is the energy source term, sometimes mentioned as Specific Absorption Rate (SAR) in the literature [62]. Q_{bio} is the bioheat term that contains the perfusion source term

Q_{bl} and the metabolic heat generation term Q_{met} :

$$Q_{bio} = Q_{bl} + Q_{met} \quad (2.3)$$

$$Q_{bl} = \rho c_{p,b} \omega_b (T_b - T) \quad (2.4)$$

where ρ_b the blood density, $c_{p,b}$ the specific heat of blood, ω_b the blood perfusion rate, T_b the arterial blood temperature, and T the tissue temperature.

To fully define the model, several boundary conditions were established. The electrodes were electrically and thermally insulated, ensuring no electrical or thermal conductivity between the electrodes and the external environment. The initial temperature of the tissue was set to 37 °C. Table 2.3 provides an overview of the terms used to represent blood perfusion and metabolism, which are crucial for modeling heat transfer in biological tissue.

The electrical and thermophysical properties of the bovine liver tissue are summarized in Table 2.4. The relative permittivity $\epsilon_{r,bov}$ and thermal conductivity k_{bov} were adjusted to account for their temperature-dependent variations, while the electrical conductivity σ_{bov} was considered as a function of the electric field.

2.4 Results

This section presents the experiment results for model validation. Following the validation of the models, the process of optimization to determine the optimal configuration of IRE parameters for the bovine liver is described.

2.4.1 Validation of the Models

The finite element models were validated empirically by comparing the model results with the temperature measured in the bovine liver tissue during the IRE experiments. Three trials of experiments were performed for each combination, where active length and distance between electrodes were set to constant at 10 mm. The experimental results are presented in Figure 2.3.

Table 2.3: Properties of blood perfusion and metabolism for heat transfer model

Parameter	Symbol	Unit	Value	References
Blood density	ρ_b	Kg/m^3	1000	[62]
Blood temperature	T_b	$^{\circ}\text{C}$	37	-
Blood specific heat capacity	$c_{p,b}$	$\text{J}/(\text{Kg } ^{\circ}\text{C})$	3640	[62]
Blood perfusion rate	ω_b	1/s	$5e^{-4}$	[62]
Metabolic heat source	Q_{met}	W/m^3	0	[63]

Table 2.4: Electrical and thermophysical properties of bovine liver tissue

Parameter	Symbol	Unit	Value	References
Density	ρ_{bov}	Kg/m^3	1050	[64]
Heat capacity	$c_{p,\text{bov}}$	$\text{J}/(\text{Kg } ^{\circ}\text{C})$	3400	[65]
Relative permittivity	$\varepsilon_{r,\text{bov}}$	-	(See Figure 2.2a)	[64]
Thermal conductivity	k_{bov}	$\text{W}/(\text{m } ^{\circ}\text{C})$	(See Figure 2.2b)	[66]
Electrical conductivity	σ_{bov}	S/m	(See Figure 2.2c)	[67]

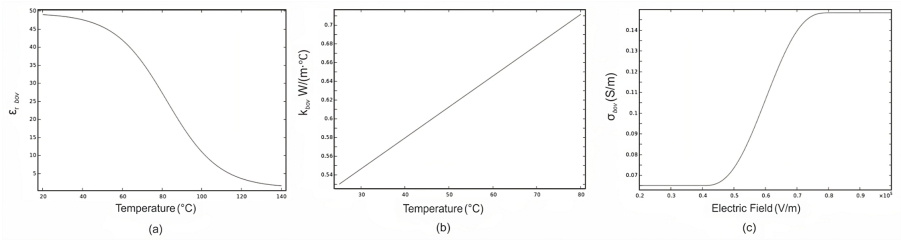


Figure 2.2: (a) Relative permittivity and (b) thermal conductivity in the function of temperature, and (c) electrical conductivity in the function of electric field for bovine liver tissue

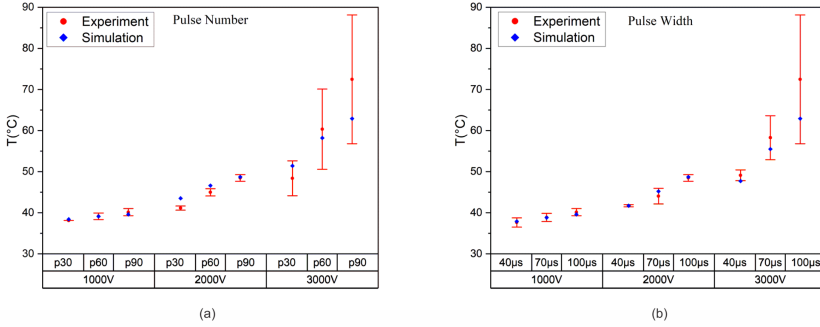


Figure 2.3: Maximum temperature in the IRE experiment and models simulation in bovine liver tissue with varying (a) pulse number and (b) pulse width

Figure 2.3a presents the temperature achieved by varying the pulse number and voltage in each experiment. The pulse width was kept constant at 100 μs , while the pulse number varied between 30, 60, and 90, and the input voltage varied between 1000 V, 2000 V, and 3000 V. The errors in the temperature measurement at the center of the electrode were relatively low, averaging around $3.9\% \pm 4.2\%$, except for the last experiment with 3000 V and 90 pulses, which had an error of up to 13.2%. In terms of thermal damage, the bovine liver tissue reached temperatures above 50 $^{\circ}\text{C}$ when the voltage was set to 3000 V and the pulse numbers were 60 and 90. Interestingly, the figure also revealed that as the pulse number and voltage increased, the maximum temperature in the bovine liver also increased.

The results from the experiment with varying pulse width are shown in Figure 2.3b. In this experiment, the pulse number was set to 90 pulses, while the pulse width and voltage were varied. The error percentage for temperature measurement in all the experiments was around $2.9\% \pm 4.2\%$, except for the last experiment with 3000 V and 100 μs combination.

Overall, the temperature profiles obtained from the FEM simulation and the ex vivo experiments were quite similar. It can be concluded that the models were successfully validated and can be used to calculate the response of the IRE parameters in the optimization study.

2.4.2 IRE Optimization for the Treatment on Liver Tissue

According to Table 2.1, there are 162 possible combinations of parameters for the experiments. To reduce the number of experiments while maintaining significant information, the Taguchi method, described by Berger et al. was used [68]. An L18($2^1 3^4$) Taguchi design was implemented using Minitab 18 (Minitab Inc., USA), resulting in 18 parameter combinations.

After validating the models, the IRE experiments were conducted using the 18 selected parameter combinations on simulation. The response of these IRE parameters was evaluated in terms of the maximum temperature and the coverage area of ablation (where $EF > 800$ V/cm), as presented in Table 2.5.

To analyze the results in Table 2.5, the RSM in Minitab was employed. This method allows for the determination of the relationship between the responses and the variables, which can be visualized through factorial plots, as shown in Figure 2.4. Additionally, the optimal solution for the IRE parameter configuration can be calculated, as illustrated in Figure 2.5. The goal is to achieve the maximum ablation area between the electrodes while ensuring that the tissue does not experience thermal damage (i.e., the tissue temperature remains below 50 °C).

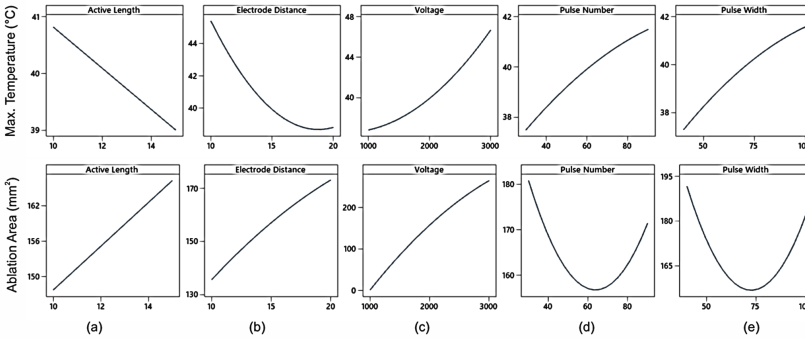


Figure 2.4: The response of the maximum temperature and the ablation coverage area ($EF > 800$ V/cm) to various IRE parameter configurations, including (a) active length, (b) electrode distance, (c) voltage, (d) pulse number, and (e) pulse width

Table 2.5: Ablation area and maximum temperature response on various IRE parameter configuration

Experiment number	Active length (mm)	Distance between electrodes (mm)	Input voltage (V)	Pulse number	Pulse width (μ s)	Ablation area (mm^2)	Maximum temperature ($^{\circ}\text{C}$)
1	10	10	1000	30	40	68.79	37.58
2	10	10	2000	60	70	135.56	43.67
3	10	10	3000	90	100	216.57	62.90
4	10	15	1000	30	70	9.46	37.00
5	10	15	2000	60	100	192.34	42.29
6	10	15	3000	90	40	297.33	43.34
7	10	20	1000	60	40	1.35	37.00
8	10	20	2000	90	70	208.79	39.82
9	10	20	3000	30	100	330.24	42.21
10	15	10	1000	90	100	95.03	39.66
11	15	10	2000	30	40	157.81	39.53
12	15	10	3000	60	70	237.69	52.61
13	15	15	1000	60	100	10.50	37.30
14	15	15	2000	90	40	216.62	39.88
15	15	25	3000	30	70	313.66	43.27
16	15	20	1000	90	70	4.74	37.35
17	15	20	2000	30	100	215.80	39.34
18	15	20	3000	60	40	375.46	40.61

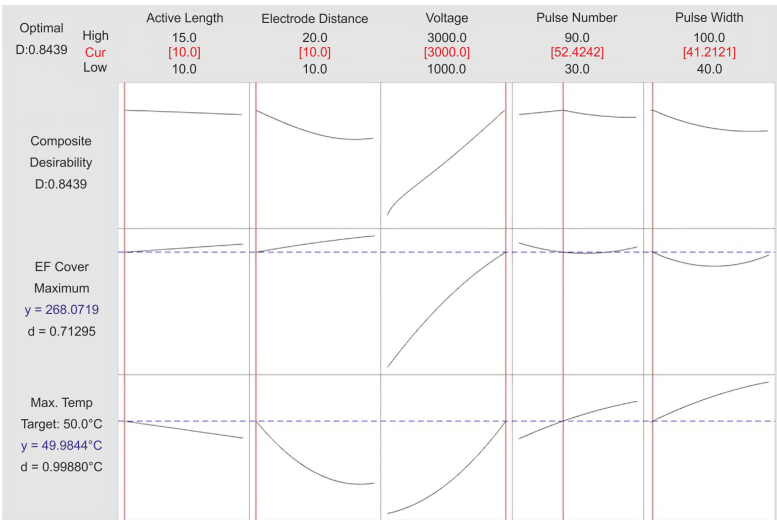


Figure 2.5: Optimization results obtained from RSM. The optimal parameters are highlighted in red brackets at the top row. The red lines in the graph indicate the optimal solutions. The blue dashed lines represent the target values of the objective functions, which in this case are the maximum electric field and a temperature of 50 °C (the threshold for thermal damage)

Based on the results shown in Figure 2.4a and Figure 2.4b, increasing the active length and the distance between the electrodes is the most effective approach to reduce the maximum temperature while increasing the ablation area during the treatment. Adjusting the input voltage can also lead to a larger ablation area, but it must be carefully chosen as it significantly increases the temperature, as demonstrated in Figure 2.4c. When considering the pulse number (Figure 2.4d) and pulse width (Figure 2.4e), using smaller values is preferable to keep the temperature low. However, increasing the pulse number and pulse width does not have a significant impact on the ablation area.

The analysis of variance reveals that the electrode distance and input voltage parameters have a significant effect on the temperature rise during IRE treatment of bovine liver ($P=0.020$ and $P=0.003$ respectively). On the other hand, only the input voltage parameter significantly affects the ablation area ($P<0.001$).

According to Figure 2.5 and the optimization study using RSM, the optimal configuration of IRE parameters for bovine liver is as follows: two electrodes with an active length of 10 mm and a separation of 10 mm, delivering 52.42 pulse repetitions with a width of 41.21 μs and amplitude of 3000 V. It should be noted that the number of pulse repetitions was rounded to 50 instead of the calculated value of 52.42 by RSM.

Table 2.6: Comparison of the optimization and simulation results with the optimal IRE parameter configuration for liver tissue

Response	RSM	Models	Error (%)
Area (mm^2)	268.07	250.82	6.43
Maximum temperature ($^{\circ}\text{C}$)	49.98	45.36	9.24

The optimal parameters obtained from RSM were utilized in the models to assess the reliability of the method. The ablation area and the maximum temperature at the center point between the electrodes were measured. The outcomes of each response were compared with the ones obtained with RSM by calculating the relative error. The findings are presented in Table 2.6.

The electric field calculated by RSM and the models showed a high level of agreement. However, RSM produced an overestimated value for the temperature. The simulation indicated a maximum temperature of 45.46 $^{\circ}\text{C}$, which is lower than the threshold for thermal damage (50 $^{\circ}\text{C}$). The error is not significant, as it is unlikely that thermal damage would occur in the tissue.

2.4.3 Electric Field and Temperature Distributions Using Optimal IRE Parameter Configuration

After verifying the reliability of the optimization process, simulations were conducted to calculate the electric field and temperature distributions in the liver tissue. The graphical representations of the simulation results for the electric field and temperature distribution are displayed in Figure 2.6.

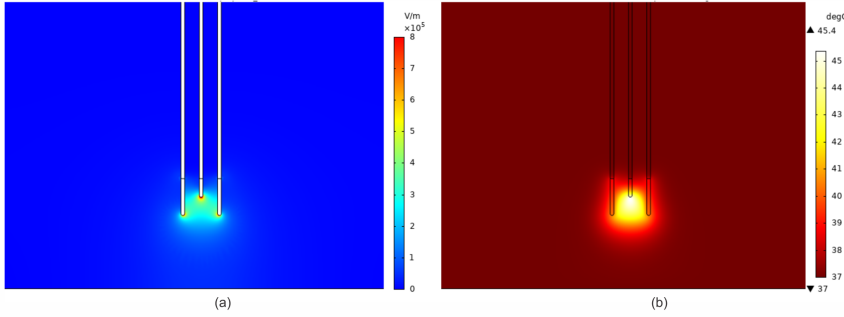


Figure 2.6: (a) Electric field distribution and (b) temperature distribution in liver tissue when applying the optimal IRE configuration

The electric field distribution appears to be relatively uniform between the electrodes. However, in Figure 2.6a, it can be observed that the electric intensity is higher near the tips of the electrodes. As charges tend to spread across the surface of a conductive material, this phenomenon can be explained due to higher concentrations of electric charges at the tips of the electrodes.

The temperature increase is more pronounced in the region between the electrodes, following a similar pattern to the electric field distribution as shown in Figure 2.6b. The temperature reaches its highest values near the vicinity of the electrodes and gradually decreases with increasing distance. The temperature rise outside the region between the electrodes is not as significant as within it. Based on these observations, it is unlikely that thermal damage would occur when the calculated optimal IRE parameter configuration is applied.

2.5 Discussion

This study presented a statistically based approach (Taguchi, RSM) to calculate the optimal configuration of IRE parameters, considering the risk of thermal damage that may occur in the tissue. Although IRE is generally considered a non-thermal treatment, our results showed that the temperature in bovine liver tissue increased within the range of 37-50 °C and can reach up to 72 °C with high voltage (3000V) parameters. This finding is consistent with

the results reported by Agnass et al. [69], suggesting that IRE can be considered as a mild-hyperthermic treatment rather than a non-thermal treatment.

Two-dimensional models were built instead of 3D models for the sake of computational speed and based on the assumption that the electric and temperature distributions are symmetric. The two-dimensional models simulate the configuration of two electrodes in a real IRE setup and provide a good approximation for planning IRE treatments [60]. Furthermore, the experimental setup was represented by a 2D plane, which corresponds to a cross-section perpendicular to the electrodes along the z-axis.

The models were validated based on experimental temperature measurements. Validation was successfully achieved, with a great part of the experiments showing percentage errors lower than the assumed threshold of 10%. However, some measurements presented relatively high errors. One possible source of error could be attributed to the incorrect placement of temperature probes. The bovine liver tissue presents a challenge due to its lack of transparency, making it difficult to visually confirm the accurate positioning of the temperature probes.

The potential error in temperature measurement resulting from improper probe placement can be illustrated using the temperature distribution depicted in Figure 2.7. In this figure, the y-coordinate of 0 mm corresponds to the point on the vertical line aligned with the tip of the electrodes. The y-coordinate values between 0 and 10 mm represent the active region of the electrodes. The measurement point at the center is situated at the y-coordinate of 5 mm. The figure demonstrates that the temperature distribution along the vertical line is not constant. Even a small error in the probe location can lead to different temperature measurement results. Therefore, it is recommended to have visual feedback, such as live ultrasound imaging, to ensure accurate probe insertion and proper positioning. This visual guidance can provide confirmation that the probes are inserted in the correct locations, reducing measurement errors caused by inaccurate probe placement.

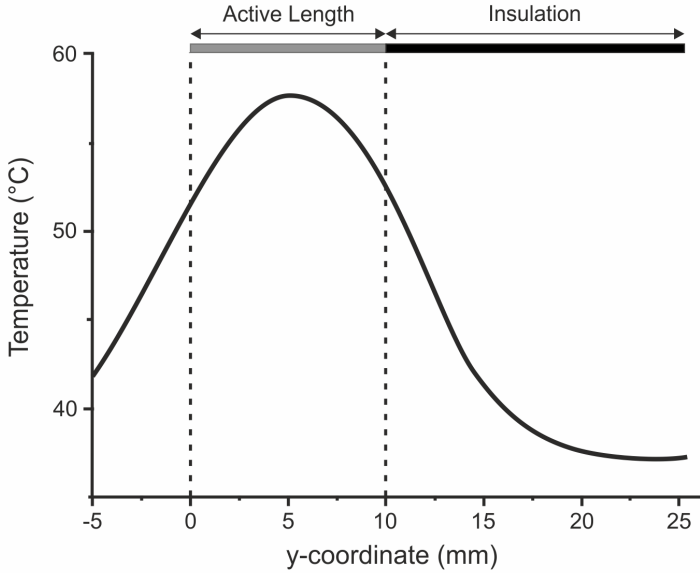


Figure 2.7: Temperature distribution at the center point between electrodes

2.6 Conclusion and Future Research

The approach presented in this study allows for the optimization of IRE parameters using validated models. By maximizing the electric field between the electrodes and limiting the maximum tissue temperature to 50 °C, an optimized combination of IRE parameters for the bovine liver was obtained. The application of this IRE configuration is expected to result in no thermal damage to bovine liver tissue, making it suitable for potential clinical use.

Five parameters were investigated in this research, including active length, distance between electrodes, input voltage, pulse number, and pulse width. Apart from these parameters, there are other parameters that could be further investigated. One example is the implementation of breaks between pulses. Evidence suggests that rest periods between pulse sequences can contribute to reducing the resultant temperature in the tissue [70, 71]. This parameter could be important to consider in the optimization of IRE with regard to its

thermal effects. Another parameter of interest is the waveform of the delivered pulses. It would be valuable to assess and compare the temperature outcomes of exponential pulses and square pulses [72].

Using another algorithm, such as Nondominated Sorting Genetic Algorithms II (NSGA-II), to calculate the optimal IRE protocol would provide additional valuable insights into the optimization process [73]. By considering both signal and electrode parameters in IRE treatment planning, the efficacy of the treatment could be improved. Therefore, it is recommended to consider both parameters during the optimization process in future research.

3

Investigating the Effect of Electrode Orientation on IRE

Adapted from: Girindra Wardhana et al. “Investigating the effect of electrode orientation on irreversible electroporation with experiment and simulation”. In: *International journal of computer assisted radiology and surgery* 17.8 (2022), pp. 1399–1407.

Abstract

Purpose In recent years, Irreversible Electroporation (IRE) has been developed to specifically destroy undesirable tissues as an alternative to surgical resection. The placement of multiple electrodes in a parallel configuration is necessary to achieve a uniform electric field distribution. However, the process of maintaining parallel electrode positions can be challenging, and the quantitative impact of electrode orientation accuracy has not been thoroughly investigated. This study aims to investigate the effect of electrode orientation, as well as various electrode and pulse parameters, on IRE outcomes.

Methods The study considered three electrode configurations: parallel, forward, and sideward orientation. A numerical model was developed to study the effect of electrode orientation on the electric field distribution. The model was validated experimentally on potato tubers as it has similar properties to biological tissue. In addition, a test was conducted to determine the conductivity and electroporation threshold of the potatoes.

Results The numerical model was successfully validated by comparing the electroporated volumes obtained from the experiment and simulation, resulting in a mean dice score of 0.727 ± 0.046 . The potato has an electrical conductivity of 0.044-0.454 S/m, with an electroporation threshold of 375 V/cm. Analysis of variance test showed that the difference in the electroporated regions between the parallel orientation and a 5° forward or sideward orientation was not significant.

Conclusion This study showed that the developed numerical models were validated and able to predict the outcome of IRE on potatoes. In addition, a tolerance of up to 5° in electrode orientation can be defined to achieve a similar response to the parallel orientation.

3.1 Introduction

Irreversible electroporation (IRE) is a novel non-thermal tumor ablation technique that has emerged as a promising ablation technique for solid tumors. IRE operates by exposing cells to electric pulses, which increases the permeabilization of the cell membrane. The impact of the electroporation pulse on the cell membrane depends on its intensity and duration, resulting in one of three outcomes: no effect, reversible membrane opening, or irreversible membrane opening leading to cell death via apoptosis [8]. The main advantages of this treatment method include reduced damage to the surrounding tissues and vascular complications, ease of application, and reduced risk of heat sink effect as commonly observed in other thermal-based ablation methods [75].

Despite the advantages of IRE, it is not considered the best choice for tumor treatment. The absence of a systematic approach to obtaining optimal treatment planning may cause incomplete tumor ablation and consequently increases the risk of tumor recurrence. The effectiveness of the IRE depends on the electric field distribution in the tissue. The electric field distribution is affected by various factors, including electrode parameters (electrode orientation, electrode active length, electrode spacing, etc.), pulse parameters (number of pulses, pulse width, pulse amplitude, etc.), and tissue properties, which influence the dose of the treatment.

One of the standard requirements of IRE for achieving a uniform electric field distribution and maximizing the ablation volume is the parallel placement of electrodes, along with equal electrode insertion depth [36]. However, maintaining this configuration can be challenging especially when dealing with tumors located deep within the body.

Several attempts have been made to study the effect of non-parallel electrode placement on the IRE outcomes. However, there has been no detailed investigation into the permissible extent of electrode orientation while ensuring treatment safety. As a result, the main aim of this study is to investigate the effect of electrode orientation on the distribution of the electric field. Furthermore, this study also investigates the relationship between electrode orientation and other IRE parameters, including the electrode active length, electrode spacing,

pulse number, and pulse length. To mimic the IRE experiment, 3D numerical models were designed and validated. The final goal is to determine the maximum deviation from parallelism for the electrodes while still yielding similar electroporation outcomes compared to the configuration with parallel electrodes. This information will assist clinicians in deciding whether to re-insert electrodes when they are not completely parallel.

3.2 Related Work

One of the main aspects of treatment planning in IRE is the specific treatment protocol administered to the patient. Several studies have investigated the influence of treatment protocols on the outcomes of IRE. This section provides a compilation of literature highlighting the challenges associated with treatment planning, particularly in relation to electrode placement.

The challenge of numerical modeling for clinical electroporation in liver tumor ablation was addressed in [76]. The study investigated the model sensitivity to parameters, including the influence of a small translation or inclination of a needle, and observed a significant impact on the distribution of the electric field. Translation of 3 mm produced a Hausdorff distance of 3.8 mm and the difference in volume was 209 mm³. An inclination angle of 5° produced a Hausdorff distance of 4.4 mm and the difference in volume was 247 mm³. The results show that a small error in the needle location can lead to large errors in the prediction of the treatment region.

A unicentric retrospective analysis where the influence of needle positioning on ablation success of IRE was studied by [77]. The analysis identified fifteen cases with residual tumors after IRE and compared them to thirty cases with successful ablations. The results revealed that in patients with residual tumors, there were significantly greater distances between the tumor center and ablation center, as well as between the tumor and needle. Additionally, the needle depth was found to be too short (2.1 mm versus 6.8 mm), and the mean needle divergence was significantly higher (7° versus 3.7°). As the study was retrospective in nature, the parameters of the needle could not be adjusted to further investigate incomplete tumor ablation.

The study by [78] analyzed the electric field distribution for non-parallel electrodes. The effect of electrode position was evaluated for inclinations at 5° and 30° in numerical models and experiments. The experiments were conducted using potatoes, while the numerical study was performed for linear and non-linear conductivity scenarios. The results indicated that changes in conductivity and electrode orientation influenced the electric field distribution. Notably, the maximum electric field was higher in cases involving nonlinear conductivity and non-parallel electrode configurations. However, it remains unknown whether there is a safety threshold for needle orientation or not.

Achieving non-parallel electrode placement can also be accomplished by varying the insertion depth. The effect of this parameter has been studied by employing a 3D numerical model aimed at optimizing electrode configuration parameters, such as electrode distance, insertion depth, and the number of electrodes [21]. The results showed that V-IRE (the voltage required to electroporate 95% of the tumor) increased as the electrode distance increased. Furthermore, V-IRE values were the lowest for two electrodes and highest for three electrodes. The study concluded that electrode distance had a more significant impact on the IRE outcome compared to insertion depth.

3.3 Methods

Three types of electrode placements were investigated in this study: parallel, sideward, and forward orientations (Figure 3.1). For forward and sideward orientations, the electrode was rotated around the center of its active length within a range of 5° - 15° . It is important to note that this study focused on configurations involving only two electrodes, where the orientation could occur on one electrode or on both electrodes simultaneously.

Finite element models (FEM) were developed to analyze the effect of electrode orientation on the outcomes of IRE. A set of experiments were conducted to validate the models. The first experiment involved measuring tissue conductivity. Then, electroporation was applied to the tissue with various electrode placements. The volumes of electroporated tissue were measured and compared to the results obtained from numerical simulations, with the

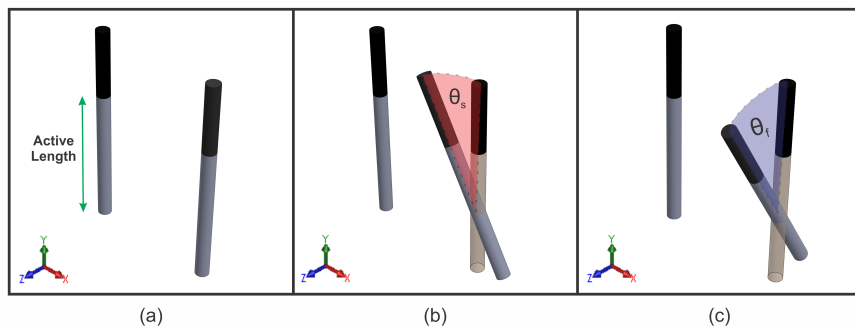


Figure 3.1: Electrode placement used in the experiments and finite element model, (a) parallel, (b) sideward, and (c) forward orientation.

Dice score used as an evaluation metric for model validation. Once the models were validated, the FEM was extended to investigate the relation between the electrode orientation and various electrode and pulse parameters in IRE. Finally, a two-way analysis of variance (ANOVA) test was performed to understand the interaction between the parameters.

In this study, IRE experiments were conducted using potato tissue as the test medium. Potatoes were chosen due to their distinct properties, which can aid in evaluating the IRE outcomes. In potatoes, it has been observed that the electroporated region becomes darker approximately 12 hours after electroporation [79]. This occurs through oxidation due to the release of polyphenol oxidase that causes membrane rupture. Furthermore, potato tissue exhibits a significant increase in conductivity after electroporation, mimicking the response seen in vivo.

3.3.1 Finite Element Models

Three-dimensional models were designed using COMSOL Multiphysics v5.5 (Comsol AB, Stockholm, Sweden). This software supports fully dynamic analysis and multi-physics modeling with defined boundary conditions. Previous studies [80, 81, 82] have used it as a finite element solver to compute the electric field distribution for simulating the IRE process.

In the 3D model, the geometry shape was simplified to reduce the number of mesh elements for faster computation. The potato tuber was represented as an ellipsoid, and the two electrodes were represented as cylinders with a diameter of 1 mm and inserted into the center of the potato. BTX Gemini X2 (Harvard Apparatus, USA) was used as a pulse generator in this study to produce a series of square wave pulses with a pulse frequency of 1 Hz. However, the generated pulses were different than the ideal square wave, as the pulse amplitude required some time to rise and fall. To mimic the real pulse from the pulse generator, the electric pulses in the simulation were modeled as square wave pulses with smoothing in the transition zone.

The values for potato conductivity and electric field threshold were derived from conductivity tests, while other potato properties were obtained from relevant literature. The electrode material was defined as structural steel, and its properties were predefined within the COMSOL software. A summary of the potato and electrode properties can be found in Table 3.1.

In COMSOL, the electrode orientation and various IRE parameters were configured by adjusting their values within the model. The distribution of the electric field within the potato was computed using Laplace's equation:

$$\nabla \cdot (\sigma(E) \nabla \varphi) = 0 \quad (3.1)$$

where σ is the electrical conductivity of the potato as a function of the electric field and φ is the applied electric potential. To complete the definition of the model, appropriate boundaries were established, including electrically insulating the potato tissue from the external environment.

3.3.2 Conductivity Test

The electrical conductivity of the potato tissue can be defined as a sigmoid function of the electric field intensity $\sigma(E)$ ([86]), as indicated by the following Equation 3.2.

$$\sigma(E) = \sigma_0 + \frac{(\sigma_1 - \sigma_0)}{2} (1 + \tanh(k_v(E - E_{th}))) \quad (3.2)$$

Table 3.1: Electrical properties of potato and electrode for numerical model

Parameter	Value	Reference
Potato		
Heat capacity (c_p)	3780 J/kg K	[83]
Tissue density (ρ)	1100 kg/m ³	[84]
Thermal conductivity (k)	0.562 W/mK	[83]
Metabolic heat generation (q^m)	2161 W/m ³	[85]
Electrodes		
Heat capacity c_p	840 J/kg K	
Thermal conductivity (k)	18 W/mK	
Electrical conductivity (σ)	1e8 S/m	
Relative permittivity (ϵ)	1	
Density (ρ)	6450 kg/m ³	

Where σ_0 and σ_1 are the conductivity of the non-electroporated and electroporated tissue, respectively. k_v is a fitting coefficient for the sigmoid function. The coefficient is an arbitrary value that modifies the smoothness of the transition between σ_0 and σ_1 . E_{th} is the electric field threshold for electroporation and E is the applied electric field intensity.

The electric field threshold is the minimum value of the electric field required to electroporate the entire potato cube. These parameter values, σ_0 , σ_1 , k_v , and E_{th} , were evaluated by finding the best fit of the pairs $(E, \sigma(E))$ using the non-linear least squares method with the Curve Fitting Toolbox in Matlab R2020b (The Mathworks, Inc., Natick, MA, USA).

Figure 3.2a shows the setup for the conductivity test. Potatoes were cut into small cubes of 10 mm \times 10 mm \times 10 mm and were placed in a well casing which was printed using a 3D printer. The dimensions of the casing were 11 mm \times 11 mm \times 11 mm (Figure 3.2b). Parallel plate stainless steel electrodes were placed on the sides of the potato cube inside the casing. The dimensions of the electrodes were 10 mm \times 20 mm \times 1 mm (thickness). The distance between the plate electrodes was 10 mm (Figure 3.2c).

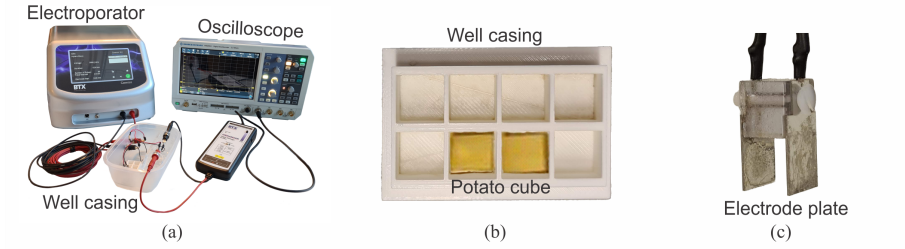


Figure 3.2: (a) Experiment setup for conductivity test (b) Well casing printed using the 3D printer for placing the potato cubes (c) Parallel plate stainless steel as electrodes

A series of 50 square wave electric pulses, ranging in voltage from 100 V to 800 V, was applied to the potato cubes via a pulse generator. To determine the resistance of the potato cube, a voltage divider circuit was employed. This involved connecting a 1 k Ω resistor across the electrodes. The potato resistance was derived from the voltage readings obtained using a high-voltage probe connected to a digital oscilloscope. Three trials of measurement were performed for each applied voltage. The resistance values were recorded, and the conductivity of the potato was calculated using the formula presented in Equation 3.3.

$$\sigma(E) = \frac{1}{R} \times \frac{L}{A} \quad (3.3)$$

Where R is the resistance of the potato tuber, L is the width of the potato, and A is the area section of the potato that was connected to the electrode.

To evaluate the effect of the IRE after the experiment, the potato cubes were stored at room temperature. The oxidation of the potatoes became apparent 24 hours after electroporation. The intensity of the discoloration in the potato cubes increased as the electric field strength increased. When the electric field value exceeded the electric field threshold, the potato cubes exhibited a darker appearance. The visualization of the potato oxidation can assist in confirming the threshold obtained from the curve fit process.

3.3.3 Validation Experiment

Potato tubers were treated with electroporation using different pulse parameters and electrode orientations. The resulting volume of electroporated tissue was used to validate the finite element model. The parameters tested in these experiments included pulse strength and pulse number in parallel configurations, as well as variations in the tilt of 5° and 10° in the sideward and forward directions. The electrode orientation was adjusted by tilting the electrode from the center of its active length. The electric field distribution is expected to be different for single and dual electrode tilts since the electroporation outcome is calculated based on the original position of the electrode.

A total of thirteen potatoes were used in this experiment, with the pulse parameters and electrode orientations for each potato listed in Table 3.2.

Table 3.2: Pulse and electrode parameter for validation experiment with pulse width 100 μ s

Parallel orientation	Sideward orientation (500 V, 50 pulses)	Forward orientation (500 V, 50 pulses)
(1) 500 V, 30 pulses	(6) Single electrode (5°)	(10) Single electrode (5°)
(2) 500 V, 50 pulses	(7) Single electrode (10°)	(11) Single electrode (10°)
(3) 500 V, 90 pulses	(8) Dual electrode (5°)	(12) Dual electrode (5°)
(4) 800 V, 50 pulses	(9) Dual electrode (10°)	(13) Dual electrode (10°)
(5) 1000 V, 50 pulses		

The electroporated volumes (darkened regions) of potatoes were measured by taking MRI images of the potatoes 24 hours after electroporation, using the MRI scanner located at the TechMed center at the University of Twente. T2-weighted FLAIR sequence (Table 3.3) was chosen for the MRI scan based on the study reported [79]. A picture of the experimental setup used for the IRE experiments is shown in Figure 3.3a. The active length of the electrodes was 18 mm and the distance between the electrodes was 10 mm as seen in Figure 3.3b.

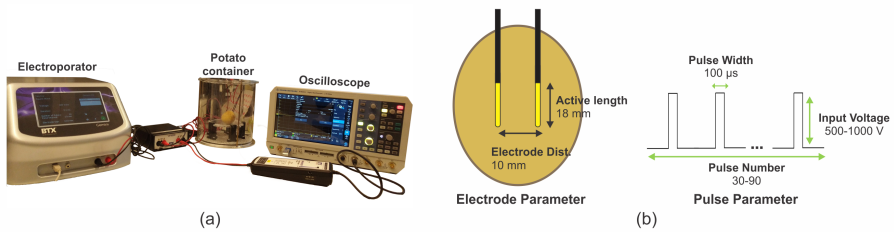


Figure 3.3: (a) Validation experiment setup used for the electroporation of the potato (b) Electrode and pulse parameter for the validation experiment.

The electroporation volumes obtained from the combination of pulse and electrode parameters listed in Table 3.2 were also determined through numerical simulation. These electroporated volumes, obtained from both experiment and simulation, were used for model validation by measuring the volume of electroporated tissue and calculating the Dice score. To ensure accurate comparison in Dice score calculation, it was important to align the position and orientation of the electroporated regions obtained from the experiment and simulation. For this purpose, the electrode position was taken as a reference point, facilitating the alignment process. The aligned results were then exported to MATLAB for calculating the Dice score.

Table 3.3: MRI scan parameters used for the acquisition of MRI images of electroporated potato tubers (T2-weighted FLAIR sequence).

Parameter	Value
MR acquisition type	3D
Slice thickness	1.1 mm
Inversion time (T1)	1800 ms
Echo time (TE)	168 ms
Repetition time (TR)	7000 ms
Acquisition matrix	200
Echo train length	153
Flip angle	120°

3.4 Results

This section describes the experimental results for validating the finite element model and the statistical results from the parametric study.

3.4.1 Potato Characterization

The potato conductivity was determined using Equation 3.3 and the unknown parameters (σ_0 , σ_1 , k_v and E_{th}) were derived by fitting the experimental data. Each conductivity value represents the average of three potato samples.

Figure 3.4a shows the oxidation of the potato cubes treated with various electric field intensities observed 24 hours after electroporation. The dark or the oxidized region represented the electroporated region in the potato and showed an increasing trend with the increase in the electric field intensity. From the curve fit in Figure 3.4b, the following parameters were obtained: $E_{th} = 375$ V/cm and $k_v = 0.0045$. The values of σ_0 and σ_1 were determined as 0.044 S/m and 0.454 S/m, respectively.

3.4.2 Model Validation

The mesh for the finite element model was built using the physics-controlled mesh option in COMSOL. The mesh resolution was set to normal with a tetrahedral shape element. A convergence test was performed to determine the appropriate element size for both the potato and electrode domains. In this test, a sequence of 50 square wave pulses with a voltage of 800 V, pulse width 100 μ s, and frequency of 1 Hz, were employed. By configuring the parameters in the mesh option, the mesh was refined until the change in ablation volume was within a 0.1% difference between two consecutive meshes.

From the result presented in Figure 3.5, the ablation volume change remained below 0.1% when the number of elements exceeded 6987 elements. Therefore, the number of elements in the mesh model was set to 6987 elements. The element sizes (average edge length of elements) for the potato and electrode domains were set to a maximum of 12.0 mm and 0.55 mm, and a minimum of 2.16 mm and 0.37 mm, respectively.

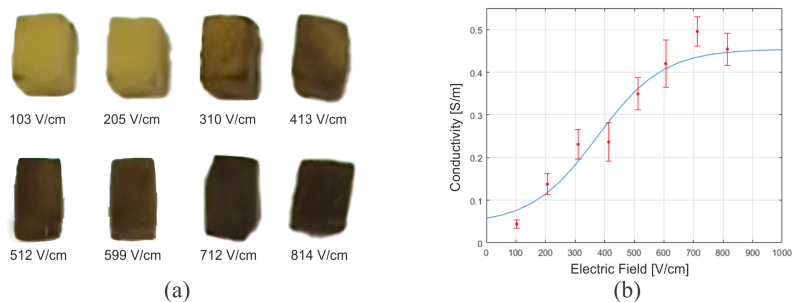


Figure 3.4: (a) Oxidation of potato cubes observed 24 hours after electroporation (b) Curve-fit obtained from the conductivity test. Each point is an average from $n=3$ potato cubes and the error bar represents the standard deviations.

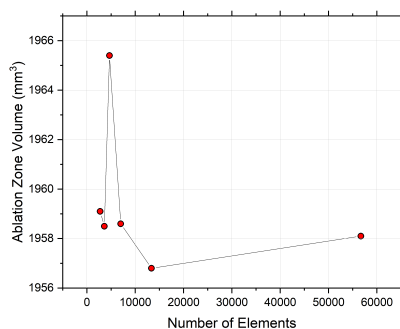


Figure 3.5: Ablation zone volume vs. the number of elements for convergence test

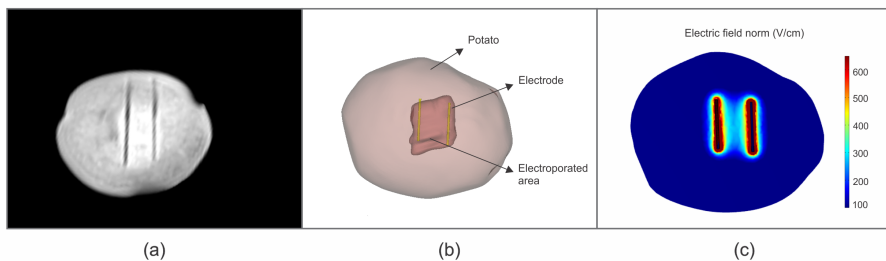


Figure 3.6: (a) MRI image of one electroporated potato tuber (b) 3D reconstruction in Slicer for potato, electrodes, and electroporated area from the MRI image (c) Electric field distribution (V/cm) on the potato from finite element model simulation

Figure 3.6a shows one of the MRI images capturing the potato after electroporation. The MRI images were loaded on 3D Slicer v4.11 to obtain the segmentation of the entire potato, electroporated volumes, and electrodes. In 3D Slicer, MRI images were manually segmented by selecting the pixel threshold for each respective region. The electrodes were represented by the dark line over the potato region, while the electroporated volumes had a brighter intensity surrounding the electrodes. The painting tool was further used to refine these segmented regions.

Figure 3.6b presents the 3D reconstruction of the segmentation for one of the potatoes. The reconstructed electrode and potato models were imported into COMSOL to calculate the electroporated volume using the simulation model. The conductivity values σ_0 and σ_1 , derived from the conductivity test, were used in the simulations. The electric field distributions corresponding to the pulse protocol used in the validation experiments were computed for each potato. Figure 3.6c shows the electric field distribution acquired in one of the slices from one of the potatoes.

The Dice score for all thirteen tested potatoes in this experiment is shown in Figure 3.7. According to the findings reported in [87], the error in the electroporated area calculation for potatoes with a ΔV of 500 V was approximately 25%, and this error increased with higher applied voltage. Therefore, it is reasonable to consider a Dice score of 0.7 as a threshold for a satisfactory match in model validation for this experiment.

By averaging the Dice scores of all thirteen potatoes, the model achieved a good result with a mean Dice score of 0.727 ± 0.046 . Therefore, we can conclude that the models have been successfully validated and can be utilized in the parametric study.

3.4.3 Parametric Study

The numerical model was further extended to investigate the electric field distribution for different electrode placements (parallel, sideward, and forward orientation) at various electrode and pulse parameter levels. Each test involved the application of two pulse strengths: 1000 V and 3000 V.

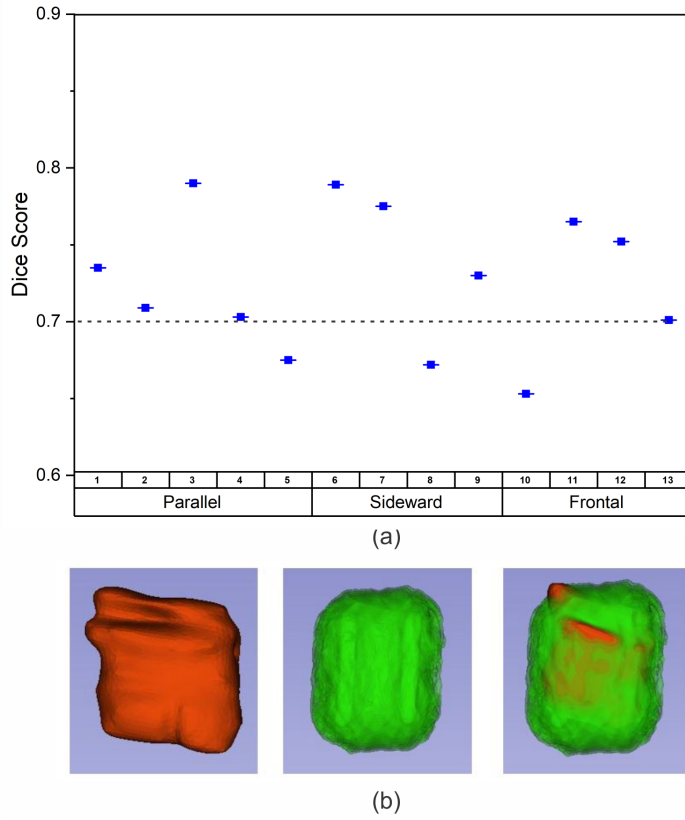


Figure 3.7: (a) The dice score obtained from thirteen potatoes in validation experiment (b) Reconstruction of electroporated volume from one of the potatoes with the result from MRI (red), simulation (green), and the overlapped between them.

The electrode parameters included the active length (AL) at levels of 10 mm, 20 mm, and 30 mm, and the electrode distance (ED) at levels of 10 mm, 15 mm, and 20 mm. In the AL test (Figure 3.8a), the electroporated volume increased to 57% for sideward orientation with a dual-electrode setup tilted at 15° and AL of 30 mm. In the ED test (Figure 3.8b), the maximum increase of 39% in electroporated volume was observed in a dual-electrode setup with 10° sideward orientation and ED of 10 mm.

For pulse parameters, the pulse number (PN) was tested at levels of 50, 70, and 90 (see Figure 3.8c), and the pulse width (PW) was tested at levels of 50 μ s, 70 μ s, and 100 μ s (see Figure 3.8d). The increase in electroporated volume obtained with the variation of PN was less than 1% for both orientations. A similar result was obtained when the PW was varied. Therefore, it can be concluded that the changes in PN and PW were not significant in changing the electroporated volume results.

To gain further insight into the obtained results, an analysis of variance (ANOVA) was performed using IBM SPSS Statistics for Windows, version 27 (IBM Corp., Armonk, N.Y., USA). The ANOVA results showed that the electrode distance ($p < 0.001$), active length ($p < 0.001$), and electrode orientation ($p < 0.001$) had a significant influence on the electroporated volume. The interaction between electrode distance and electrode orientation had a significant effect on the electroporated volume only in the single electrode sideward orientation setup ($p = 0.023$). Similarly, the interaction between active length and electrode orientation had a significant influence on the electroporated volume in all electrode orientations ($p < 0.001$).

It was also observed that there was no significant difference in the electroporated volume when comparing a parallel orientation to a single electrode with 5° orientation in sideward ($p = 0.134$), forward ($p = 0.276$) and dual electrode with 5° orientation in frontal orientation ($p = 0.997$) when varying the electrode distance. Similarly, when considering the active length and electrode orientation, there was no significant difference in the electroporated volume between parallel orientation and a 5° orientation in all electrode orientations.

3.5 Discussion

Based on the results of the parametric study, it is evident that the electrode distance, electrode active length, and electrode orientation have a significant impact on the increase of the electroporated volume. Among various electrode orientations, the sideward orientation resulted in the highest increase in the electroporated volume.

The statistical analysis revealed that orientations up to 5° in both sideward and forward directions can produce similar electroporated volumes compared to a parallel orientation. Orienting both electrodes shows a significant increase in the electroporated volume. This electrode arrangement may be considered for treating deep-seated tumors where a parallel electrode orientation is not feasible. However, aligning the electrodes toward each other must be avoided due to the high risk of overcurrent, which can potentially cause thermal damage to the tissue. For tumors where a parallel electrode orientation is possible, it can be considered safe to allow a tolerance level of up to 5° in electrode orientation.

Three-dimensional numerical models were designed to simulate two electrode placements on potato tissue. The accuracy of the numerical model was validated by comparing the electroporated regions obtained from the experiment with those generated by the simulation. From thirteen potatoes, a mean dice score of 0.727 ± 0.046 was successfully achieved. However, some samples presented lower Dice scores, ranging from 0.65 to 0.70.

One of the main factors contributing to the lower Dice scores is the challenge of accurately measuring the electroporated region in potatoes. In this study, the electroporated regions in potato images were manually segmented based on the discoloration observed in the MRI images. Due to the lack of clear boundaries, there is a possibility that the electroporated areas were not segmented precisely. Furthermore, shrinkage of the potato tissue was observed after the treatment, which could result in a reduction of the segmented region.

Another factor that can impact the accuracy of the model is the variability in the conductivity values and the electric field thresholds of potatoes.

The results obtained from the conductivity test in this study are similar to those reported in [88]. However, potato conductivity has been found to vary in different studies, as reported in [87] and [89]. Moreover, the electric field thresholds for potatoes mentioned in the literature range from 184 V/cm [89] to 478 V/cm [88]. This wide range of conductivity values and electric field thresholds poses a challenge in designing accurate numerical models for predicting the volume of electroporated tissue.

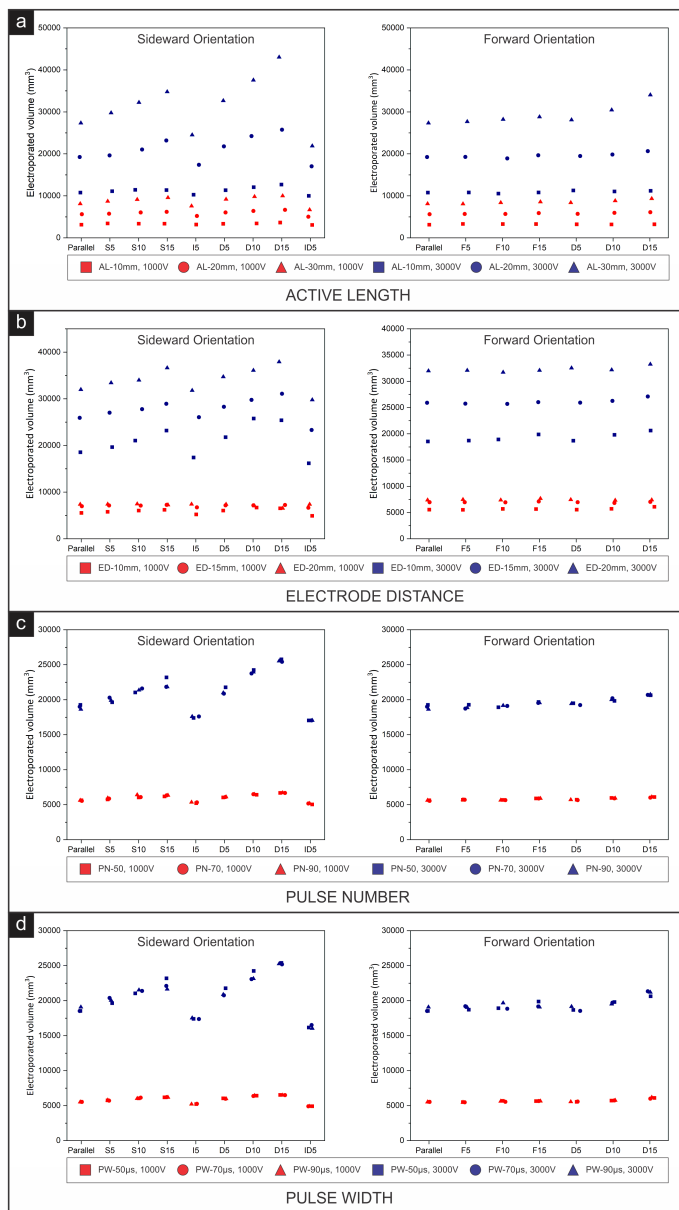


Figure 3.8: Electroporated volume with various IRE parameters: (a) Active length, (b) Electrode distance, (c) Pulse number, and (d) Pulse width.

3.6 Conclusions and Future Work

IRE is a relatively new non-thermal tumor ablation technique. Despite its advantages, it is not considered as an immediate choice of treatment. One of the reasons for this is the lack of a systematic approach to optimize treatment planning. The investigation of the electrode orientation's effect on IRE outcomes is a step toward improving treatment planning. Maintaining a parallel electrode configuration can be challenging, particularly when treating tumors located deep within the body.

Our study aimed to examine the effect of electrode orientation along with several IRE parameters on the IRE outcome using a 3D numerical model. The findings showed that parameters such as the active length of the electrodes, electrode distance, and electrode orientation significantly influenced the electric field distribution. Statistical analysis indicated that, for most orientations, there was no significant difference in the electroporated volumes between a parallel orientation and a 5° electrode orientation. Therefore, it can be concluded that introducing orientations to an electrode up to 5° can result in a similar outcome compared to an electrode in a parallel position.

To improve the accuracy of the current model, validation using hydrogels that better mimic soft tissue properties can be conducted. Hydrogel offers the advantage of transparency, making it easier to monitor and ensure precise electrode placement and orientation [80]. In addition, validation on different heterogeneous tissues with varying IRE configurations is necessary, as potato tubers are relatively homogeneous compared to human or animal tissue. The numerical models can also be further extended to implement more electrodes. Finally, few studies have investigated the optimal dose of IRE parameters for parallel electrode orientations. Optimizing IRE parameters for different electrode orientations can offer valuable insights to enhance the accuracy of treatment planning by effectively targeting and covering the entire tumor region.

4

Liver and Tumor Segmentation Using Deep Learning

Adapted from: Girindra Wardhana et al. “Toward reliable automatic liver and tumor segmentation using convolutional neural network based on 2.5D models”. In: *International Journal of Computer Assisted Radiology and Surgery* 16 (2021), pp. 41–51.

Abstract

Purpose We investigated the parameter configuration for automatic liver and tumor segmentation using a convolutional neural network based on the 2.5D model. The 2.5D model has shown promising results since it allows the network to have a deeper and wider network architecture while still accommodating the 3D information. However, there has been no detailed investigation of the parameter configurations for this specific network model.

Methods In our study, we focused on several parameters, including the number of stacked layers, image contrast, and the number of network layers, and implemented them in neural networks based on the 2.5D model. We trained and tested these networks using the dataset from the liver and tumor segmentation challenge. The network performance was further evaluated by comparing the network segmentation with manual segmentation from nine technical physicians and an experienced radiologist.

Results The results from the slice arrangement test demonstrate that networks with multiple stacked layers outperform single-layer networks. However, the Dice scores begin to decrease when the number of stacked layers exceeds three layers. This suggests that adding too many layers can lead to overfitting. In the contrast enhancement test, implementing contrast enhancement methods did not show statistically significant differences in network performance. Additionally, in the network layer test, adding more layers to the network architecture did not consistently result in higher Dice scores for the network.

Conclusions This chapter presents a comparison of network performance based on the 2.5D model using different parameter configurations. Our findings highlight the effect of each parameter, providing insights for the selection of optimal configurations to improve the network performance in automatic liver and tumor segmentation applications.

4.1 Introduction

Liver cancer is among the leading causes of cancer death globally (2015:810.000) with increasing diagnosed cases (2015:854.000) [91]. Prevention and treatment of liver disease are urgent since early action can significantly reduce the progression of the disease. Clinicians utilize medical imaging to provide an early diagnosis by providing a clear picture of the possible lesion inside the patient's body. Segmentation, the process of separating the lesion from surrounding organs or tissues, plays a vital role in extracting critical information such as size, shape, and precise location of the lesions. Image segmentation facilitates diagnostic analysis and aids clinicians in making informed decisions [92].

One of the segmentation strategies, manual segmentation, is still used regularly by radiologists. Even though this method can provide precise liver shape and volume, the method is time-consuming, laborious, and subjective, as it relies on the skills and expertise of the clinician performing the segmentation.

The need for efficient liver segmentation techniques has led to the development of more automated methods, for instance, contour optimization, semi-automated, and fully automated approaches [93]. Contour optimization and semi-automated methods provide clinicians with greater flexibility, as they only need to identify the initial reference point, leaving the remaining segmentation process to be completed by computer algorithms. However, these methods are still prone to subjectivity due to the need for user input. By incorporating more automated steps into the segmentation process, both time efficiency and segmentation precision can be improved [94]. With reduced reliance on manual interaction, automated approaches offer the potential for time savings and more consistent and accurate liver segmentation results.

Despite the advantages of automatic segmentation methods, there is still room for improvement in their performance [95]. Segmenting the liver from Computed Tomography (CT) images is a challenging task due to various contrast agents and acquisition protocols, resulting in a wide range of liver intensity. Additionally, the low contrast between the liver and adjacent organs makes it difficult to detect the liver boundaries accurately. Automatic methods that rely

on intensity information, such as threshold and region growing [96, 97], are prone to detect other organs as liver areas due to the lack of shape control. On the other hand, techniques that utilize descriptive shape information, such as level set-based methods [98, 99] and statistical shape models [100, 101, 102], face complexity in separating the liver from other organs due to the highly varied shapes and sizes of livers among individuals.

Tumor segmentation poses an even greater challenge compare to liver segmentation. While the liver has variations in size and shape, its location is predictable. However, liver tumors have not only various sizes and shapes, but also the location and numbers can vary considerably within a patient population. In addition, some tumors do not have clear boundaries, further limiting the performance of automatic segmentation methods that rely on intensity information for tumor identification.

In recent years, deep learning applications, especially convolutional neural networks (CNNs), have shown great success in addressing the segmentation problem. Unlike other methods, CNNs perform all processes automatically, including feature extraction, without the need for handcrafted features.

In a recent segmentation competition, participants were challenged to develop an automatic segmentation algorithm for the liver and tumors in contrast-enhanced abdominal CT scans. Most of the participants employed deep neural networks to segment the liver and tumors. Chlebus [103] presented a convolutional neural network based on the 2D U-Net architecture. Two models were proposed to segment the liver and tumors, and a random forest classifier was employed to reduce false positives among the tumor candidates. Bi [104] proposed cascaded ResNet to overcome the layer limitation in order to extract more discriminative features. Other studies have shown that incorporating 3D information can improve segmentation results. Li [105] proposed hybrid dense units that consist of 2D dense units to extract intraslice features and 3D dense units to exploit interslice context from a volumetric image.

Including 3D information is reasonable, considering CT images are typically volumetric medical images. However, implementing 3D convolutions encounters several issues, such as high computational cost and memory usage. An alternative approach to accommodate 3D information into the network is by

using a 2.5D model. Han [106] proposed a deep convolutional neural network architecture that combines the long-range connections of U-Net and the short-range residual connections of ResNet. Two models were developed: the first model was used to segment the liver region as an input, and the second model was used to detect and segment tumors. Both models worked in 2.5D, where five adjacent slices were used as input, producing the segmentation of the center slice. The main purpose was to maintain computational efficiency by using 2D slices while still providing 3D context information to the network.

The implementation of the 2.5D model has shown promising results as it allows for a deeper and wider network architecture while still incorporating the benefits of 3D information. In this study, our goal is to evaluate how different configurations of input parameters affect the accuracy of segmentation outcomes, with the aim of optimizing the performance of the neural network based on the 2.5D model. We will investigate three main parameters. The first parameter is the number of stacked layers in the input image, which is a defining characteristic of the neural network based on the 2.5D model. The second parameter is the effect of image contrast, which will be tested by applying various contrast enhancement techniques to the dataset. The third parameter is the number of layers in the network architecture.

4.2 Materials and Methods

4.2.1 Datasets

The dataset used in this study was obtained from the Liver and Tumor Segmentation (LiTS) challenge [107], which was organized in conjunction with Medical Image Computing and Computer Assisted Intervention (MICCAI) 2017 and IEEE International Symposium on Biomedical Imaging (ISBI) 2017. The dataset contains contrast-enhanced abdominal CT scans from various clinical sites, utilizing different scanners and scanning protocols. As a result, the dataset has a wide range of variations in resolution and image quality [108]. It consists of 131 training images and 70 test images. Clinical experts manually performed segmentations for each training image, which serve as the ground truth.

To investigate the effects of slice arrangement and contrast enhancement on input images, we used the training images for both training and evaluation. Specifically, the training images were separated into 111 images for training and 20 images for evaluation. On the other hand, the study exploring the effect of layer numbers in the network architecture will utilize the entire dataset, including both the training and test images. The test result will be validated through submission to the LiTS website.

4.2.2 Network Training

The network training process is divided into four steps, as illustrated in Figure 4.1. In the first step, several actions were performed on the dataset to standardize the input images. This involved calibrating the pixel values of the images and limiting the image intensity range. In the second step, the network architecture was defined. Additionally, the pre-processing tasks were carried out, such as the investigation on the number of image slices and image contrast. In the third step, training options were configured. Once the configuration was complete, the network training process started, enabling the network to learn and optimize its performance. Upon completion of the training process, the network became capable to segment the liver and tumors from CT scan images. Finally, in the fourth step, the post-processing stage was applied to refine the segmentation result, leading to the final outcome.

STEP 1: Image Normalization

The image intensity in the CT scan dataset is measured using the Hounsfield unit. Due to variations in machines and imaging protocols used during image acquisition in the dataset, intensity calibration is required. The calibration process involves applying a linear calibration function, which is expressed by Equation 4.1:

$$HU = a \cdot HU_o + b \quad (4.1)$$

where a represents the multiplication factor and b represents the addition factor. These factors can be obtained from the header information of the CT image. The initial pixel value from the image is denoted as HU_o , and the calibrated image intensity is denoted as HU .

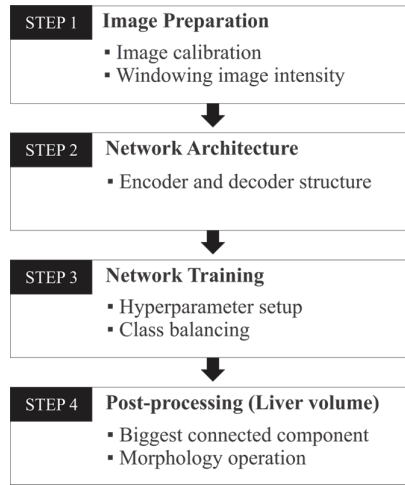


Figure 4.1: Network training workflow: image preparation, network architecture, network training option, and post-processing

To enhance the visual contrast and simplify the image analysis, the image intensity is windowed to a specific range. In this study, the image intensity is truncated to the range of $[-250, 250]$ to focus on the fat tissue and soft tissue areas. Subsequently, the intensity values are normalized to a grayscale unit range of $[0, 255]$. All processes in step 1 are illustrated in Figure 4.2.

STEP 2: Neural Network Architecture

The network architecture employed in this study was based on SegNet network structure [109], which consists of an encoder and decoder part. However, two main modifications were introduced to improve the network's performance. The first modification utilized the long-range connection from U-Net [110], which connects the output of the encoder to the decoder directly. The second modification was the implementation of the short/skip connections that are commonly found in the ResNet [111]. By incorporating these connections, the information from the input of the previous layer is preserved in the stacking layers. This approach helps reduce the risk of gradient vanishing in the deeper network and facilitates easier optimization during the training.

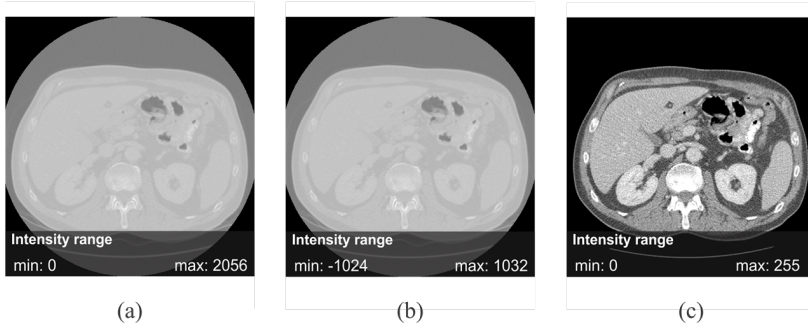


Figure 4.2: Normalization steps for images in the dataset: (a) Raw image with intensity (0,2056), (b) calibrated image with intensity (-1024, 1032), and (c) normalized image with intensity (0,255)

4

STEP 3: Training

Network models were developed using Deep Learning Toolbox in MATLAB 2018a (The MathWorks, Natick, USA). The training was performed on a single NVIDIA GeForce GTX 1070 GPU with 8GB memory. The initial learning rate was set to 0.001 and Stochastic Gradient Descent with momentum of 0.9 was used as the optimizer. During training, the learning rate was reduced by a factor of 0.1 every five epochs, and each model completed training after 20 epochs. To increase the amount of training data, data augmentation techniques such as reflection, rotation, scaling, and transition were randomly applied.

To address the issue of class imbalance and mitigate the effect of dominant classes on the segmentation result, balanced data across all class labels were preferred. Several methods have been discussed by López et al. [112] to overcome the issue of unbalanced data. In this study, two methods of class balancing were implemented during the training process.

The first method involved data resampling, where the training data was modified to produce a more balanced dataset. This approach was similar to the one applied by Chlebus et al. [103], where only image patches containing tumors and background were used, and Bi et al. [104], who considered slices containing both the liver and tumors for training their network. In this study, the

undersampling technique was applied to the training set, where slices from the CT image volume were filtered based on the segmentation labels. Slices containing background, liver, and tumor were selected for training the network, while slices containing only the liver without a tumor or just the background were discarded. The second method involved applying class weight to adjust the cost of class errors. The lower the presentation of the class, the higher the class weight it has. The class weight was calculated using Equation 4.2.

$$classWeight = \frac{N}{n} \quad (4.2)$$

where N represents the total pixel number in the dataset and n which represents the total pixel in a specific class.

STEP 4: Post-processing

The segmentation of CT images was performed in a slice-by-slice manner, where each individual slice from the CT image was segmented separately. The segmentation results from each slice were then combined to form a 3D segmentation volume.

In this study, post-processing steps were applied to reduce noise in the liver segmentation volume. In the beginning, a liver mask was created by selecting the largest 3D-connected component from the segmentation volume. This mask was applied as a filter to remove the false positive liver and tumor segmentation outside the liver area. Afterward, morphological operations, such as erosion and dilation, were employed to smooth the surface of the liver volume. These operations helped refine the boundaries and enhance the overall quality of the liver segmentation.

4.2.3 Study Design

Slice arrangement test

Two types of networks were trained: a single-layer network and a multiple-layer network. The difference between these networks lies in the variation of the slice number in the input image. The multiple-layer networks, which represent the networks using the 2.5D model, use a stacked input layer to provide

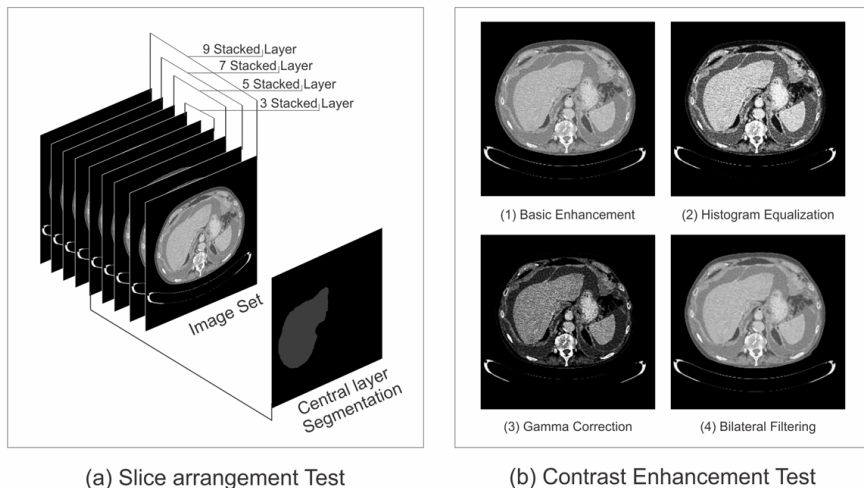


Figure 4.3: Experiment setup for parameter study on neural network based on 2.5D model. (a) Slice arrangement test with five networks using a different number of stacked layers, and (b) contrast enhancement test with four networks applying different contrast enhancement techniques, where (1) basic contrast enhancement, (2) histogram equalization filter, (3) gamma correction filter, and (4) bilateral filtering

3D information to the network. The stacked layer is constructed by combining the center layer with additional layers from the top and bottom. The segmentation map for this stacked layer corresponds to the center slice. The networks were trained with various configurations, including one slice, three slices, five slices, seven slices, and nine slices. More detailed information about these configurations can be found in Figure 4.3a.

Contrast enhancement test

In the image normalization step, we implemented a technique called basic contrast enhancement, which involves windowing and normalizing the CT image to increase its contrast within a specific intensity range. We can further enhance the CT image contrast using different methods such as histogram equalization, gamma correction, and bilateral filtering. The contrast difference in the final image from each method is illustrated in Figure 4.3b.

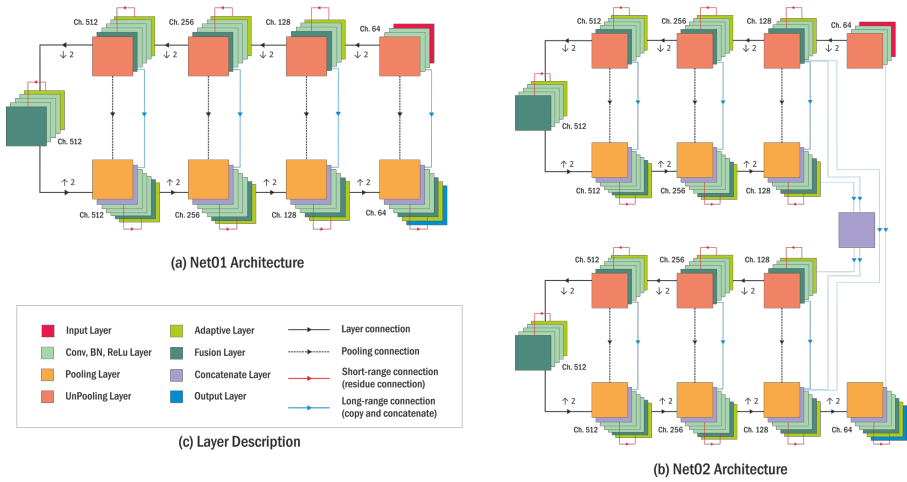


Figure 4.4: Overview of convolutional neural network model architecture that inspired by the encoder and decoder structure. (a) Net01 combines the SegNet model with long-range connections from U-Net and short-range connections in ResNet. (b) Net02 is an expanded version of Net01, where the dense connection of the encoder and decoder is applied in the structure to improve the number of layers in the network. (c) Description of layer type in Net01 and Net02. Convolution layers and adaptive layers use a kernel size of 3×3 and 1×1 , respectively. Meanwhile, Pooling and unpooling layers are used to half and double the pixel resolution.

Four networks were trained to evaluate the impact of contrast enhancement on network performance. One network utilized only basic contrast enhancement, while the other three networks utilized additional contrast enhancement methods in their input images alongside the basic contrast enhancement. The objective was to determine the most suitable method of contrast enhancement that can effectively improve network performance.

Network layer test

In this experiment, two network architectures were designed, as illustrated in Figure 4.4. The first architecture, referred to as Net01, was based on the SegNet structure. The Net01 structure was employed during the slice arrangement and contrast enhancement test. Meanwhile, the second structure, referred to as Net02, was an upgraded version of Net01, where the network architecture

was expanded from one to two encoder and decoder components. This expansion was inspired by the approach proposed by Fu et al. [113] to increase the number of layers in the encoder-decoder structure. Instead of simply adding more convolutional layers to the same encoder-decoder structure to increase the network parameters, it was found to be more effective and efficient to stack additional encoder and decoder components.

Segmentation comparison test

To gain further insights into the performance of the proposed networks, a segmentation comparison experiment was conducted involving ten subjects with a clinical background, including an experienced radiologist and nine technical physicians. In this experiment, the participants manually performed segmentations of the liver and tumors on 15 image slices, with each slice being obtained from 15 different patients in the evaluation dataset. At the same time, the segmentations of these image slices were obtained automatically using the proposed networks (Net01 and Net02).

4.3 Result and Discussion

4.3.1 Slice Arrangement Test

The Dice scores of liver and tumors were used to evaluate the performance of neural networks. Statistical analysis revealed significant differences in the mean Dice scores for liver ($F(1.752, 31.533) = 8.278, P = 0.002$) and tumor ($F(2.278, 41.009) = 9.322, P < 0.0005$) among the different stacked slice numbers. Based on the result presented in Table 4.1, the network using a single slice obtained a lower Dice score compared to the other networks that adopted multiple slices in their input image. The network with one slice achieved a Dice score of $87.7 \pm 5.4\%$ for the liver and $33.5 \pm 26.3\%$ for the tumor. In contrast, the network with three slices achieved the highest Dice score, with values of $90.5 \pm 4.7\%$ for the liver and $41.1 \pm 28.0\%$ for the tumor.

Increasing the number of stacked slices in the input image provides the neural network with more 3D context. However, adding more layers may decrease performance due to the risk of overfitting the training set. This complexity is

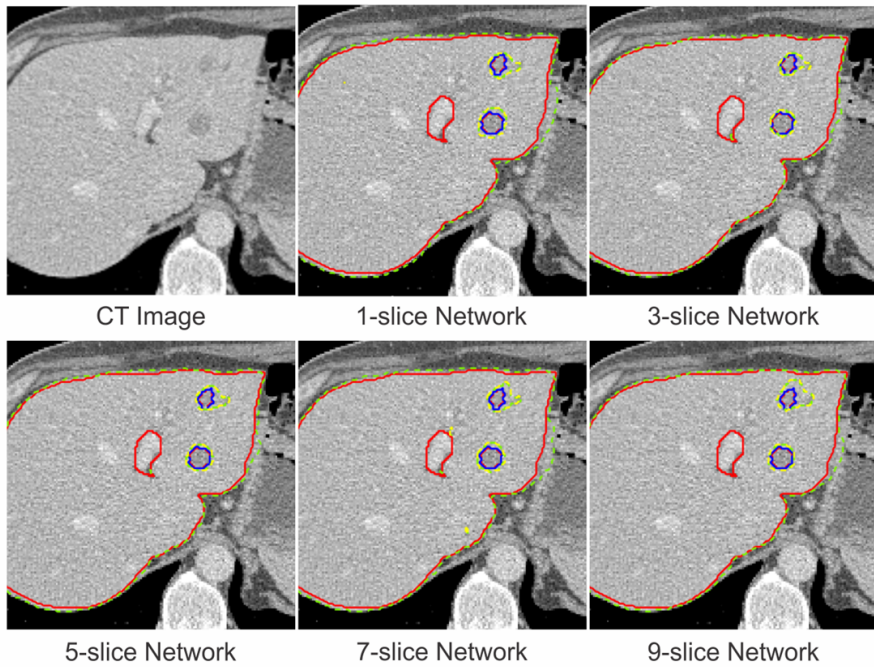


Figure 4.5: Selected segmentation result of liver and tumor from slice arrangement test. Liver and tumor boundaries are represented by the green and yellow dashed lines in the segmentation result and the red and blue solid lines in the ground truth.

particularly relevant for networks utilizing 2D convolution layers, where each slice is processed individually. It is important to maintain similar information across all stacked slices to ensure consistent performance.

Using Hausdorff distance as an additional evaluation metric, it is clear that multiple-layer networks have a better segmentation compared to single-layer networks, as indicated by smaller Hausdorff distance. For liver segmentation, there is no correlation between the number of stacked slices and the Hausdorff distance. This is because the liver volume consists of a number of slices, and the liver shape remains relatively consistent throughout the stacked layers.

In tumor segmentation, the Hausdorff distance increases as the number of network layers increases. With a small number of stacked layers, the tumor shape in the center slice closely resembles the tumor shapes in the top and bottom layers. However, as the number of slices increases, the tumor shapes in the top and bottom layers may differ significantly or not appear at all. This inconsistency distorts the tumor shape information in the network, thereby reducing the network's ability to accurately recognize tumors. This can be observed in Figure 4.5, where the input image has more than three layers, resulting in a higher number of false positive tumors detected in the segmentation result.

4.3.2 Contrast Enhancement Test

Four networks were trained using different contrast enhancement techniques with three stacked slices in the input image. The results in Table 4.2 indicate that employing histogram equalization to increase image contrast contributes to a lower Dice score compared to other techniques. Histogram equalization enhances contrast by equalizing the distribution of pixel intensities based on the image histogram. However, this method relies on the histogram data, which varies across different image datasets. As a result, each image is treated differently, leading to variations in intensity distribution for the same organ in different image datasets. This variability makes it challenging for a network to identify specific features representing the volume of an object in the image. Therefore, the network with the histogram equalization method has the worst segmentation result among other contrast enhancement techniques, with an average liver Dice score of $85.1 \pm 16.9\%$ tumor Dice score of $36.4 \pm 26.6\%$.

The network employing bilateral filtering achieves the highest mean Dice score, showing a slight improvement over the network with basic contrast enhancement. However, the implementation of bilateral filtering can be risky, particularly for tumor segmentation. This technique increases the image contrast by applying a Gaussian filter for reducing the noise in the image, but it may also remove small lesions from the image.

Table 4.1: The result of slice arrangement test on validation dataset (20 patients)

Metric	Slice-1	Slice-3	Slice-5	Slice-7	Slice-9	P value*
<i>Dice score</i>						
Liver	87.7 ± 5.4%	90.5 ± 4.7%	89.7 ± 5.1%	89.1 ± 5.2%	90.1 ± 4.7%	0.002
Tumor	33.5 ± 26.3%	41.1 ± 28.0%	39.9 ± 27.9%	33.4 ± 25.7%	38.4 ± 27.8%	< 0.0005
<i>Hausdorff distance</i>						
Liver	24.8 ± 13.8%	21.0 ± 14.0%	20.2 ± 12.8%	22.6 ± 14.3%	20.7 ± 13.8%	0.107
Tumor	56.3 ± 16.1%	51.6 ± 16.6%	51.8 ± 17.4%	52.8 ± 15.6%	55.3 ± 17.5%	0.130

Table 4.2: The result of contrast enhancement test on validation dataset (20 patients)

Dice score	Basic enhancement	Histogram equalization	Gamma correction	Bilateral filtering	P value*
Liver	87.7 ± 5.4%	90.5 ± 4.7%	89.7 ± 5.1%	89.1 ± 5.2%	0.002
Tumor	33.5 ± 26.3%	41.1 ± 28.0%	39.9 ± 27.9%	33.4 ± 25.7%	< 0.0005

* Repeated measures ANOVA test with a Greenhouse–Geisser correction, $\alpha = 0.05$

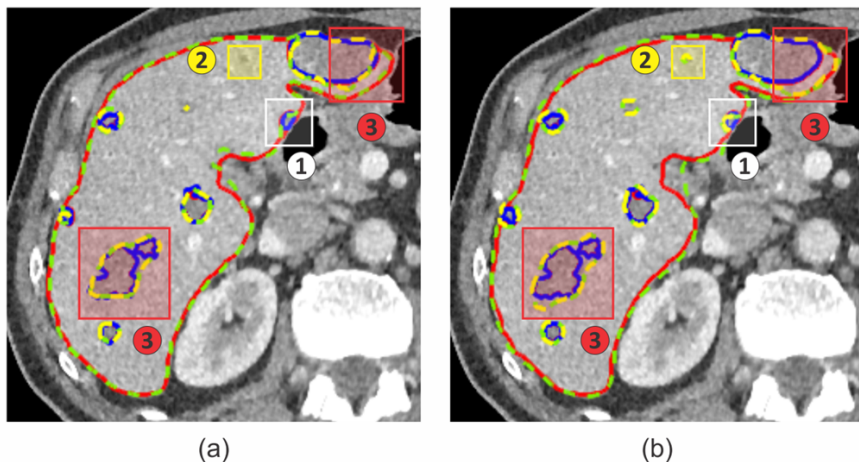


Figure 4.6: Segmentation comparison between ground truth and (a) Net01 segmentation and (b) Net02 segmentation. Three main differences are identified. (Case 1-White box) A tumor that missing from Net01 can be identified by Net02; (Case 2-Yellow Box) Some false positive tumors are identified by Net02; (Case 3-Red Box) Net02 tends to overestimate the tumor segmentation size. Liver and tumor boundaries are represented by the green and yellow dashed lines in the segmentation result and the red and blue solid lines in the ground truth.

Although variations in the mean Dice scores were observed in this test, the differences were not statistically significant ($P_{\text{liver}} = .117$ and $P_{\text{tumor}} = .094$). The test results do not provide a clear explanation of the effect of additional contrast enhancement on network performance. Therefore, we decided to proceed with only the basic contrast enhancement technique in the next phase.

4.3.3 Network Layer Test

Based on the result of the slice arrangement and contrast enhancement test, two networks, Net01 and Net02, were trained with a different number of layers. The performance of both networks was evaluated by segmenting the test dataset, which consisted of 70 patients from the LiTS dataset. The evaluation scores are presented in Table 4.3.

Table 4.3: Comparison of various liver and tumor segmentation methods in LiTS test dataset (70 patients)

Team	Lesion			Liver	
	Dice per case	Dice global	Recall at 50% overlap	Dice per case	Dice global
Net01 - Encoder and Decoder Net	56.2%	67.2%	0.348	91.4%	92.8%
Net02 - Densely Encoder and Decoder Net	50.1%	65.3%	0.465	91.1%	92.2%
Hans.meine[103]	67.6%	79.6%	0.397	96.0%	96.5%
H-DenseUnet[105]	72.2%	82.4%	0.393	96.1%	96.5%

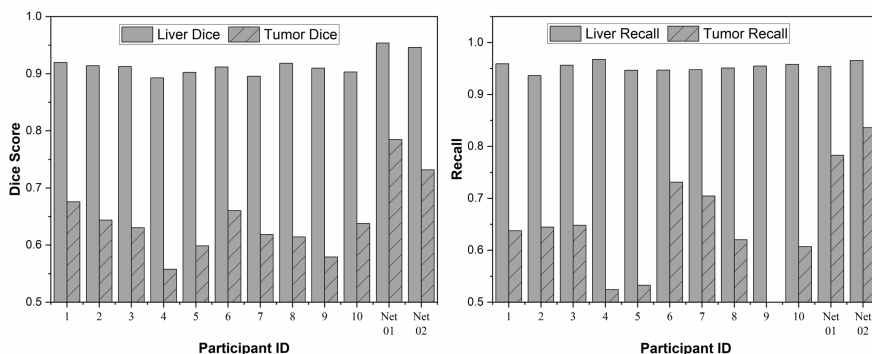


Figure 4.7: Average Dice and recall score of liver and tumor segmentation on 15 image slices. The segmentation were obtained from the manual method (ID1 to ID10) and the automatic method (Net01 and Net02)

This table shows that the liver Dice scores for Net01 and Net02 are quite similar. However, Net01 has higher tumor Dice scores compared to Net02. This can be explained by the segmentation results shown in Figure 4.6.

Net02, with its increased number of layers, has higher sensitivity to tumors compared to Net01. This is because the additional layers provide more features and improve tumor recognition in Net02. For instance, in case 1, a tumor that was missed by Net01 is successfully identified and segmented by Net02. However, higher sensitivity also means that some tumors are misidentified by the network, as observed in case 2. In addition, Net02 tends to exaggerate the tumor area, as shown in case 3. As a result, the false positive tumor rate increases, contributing to the lower Dice score of Net02 compared to Net01.

Although our network's segmentation scores are lower compared to other methods mentioned in Table 4.3, it is worth noting that those methods implement additional techniques to improve their performance. For instance, the hans_meine team [103] applies extensive post-processing, such as conditional random field and random forest classifier, to remove falsely detected tumors. On the other hand, H-DenseUNet [105] combines image features using both 2D DenseUNet and 3D DenseUNet to achieve better recognition of the liver and tumor areas.

4.3.4 Segmentation Comparison Test

The test for comparing the performance of manual and automatic segmentation was conducted using 15 image slices from 15 different patients. Two evaluation metrics, Dice score and recall, were used, and the results are shown in Figure 4.7.

For liver segmentation, the automatic segmentation labeled with Net01 and Net02 achieved average liver Dice scores of $95.3 \pm 1.8\%$ and $94.6 \pm 2.0\%$, respectively. It surpassed the result from manual segmentation, which had a maximum score of $91.9 \pm 3.5\%$. However, in terms of recall metric, the manual segmentation slightly outperformed the automatic segmentation, with a score of $96.7 \pm 2.9\%$ compared to $96.6 \pm 4.1\%$ for Net02. These results indicate that both methods are capable to identify the liver area properly.

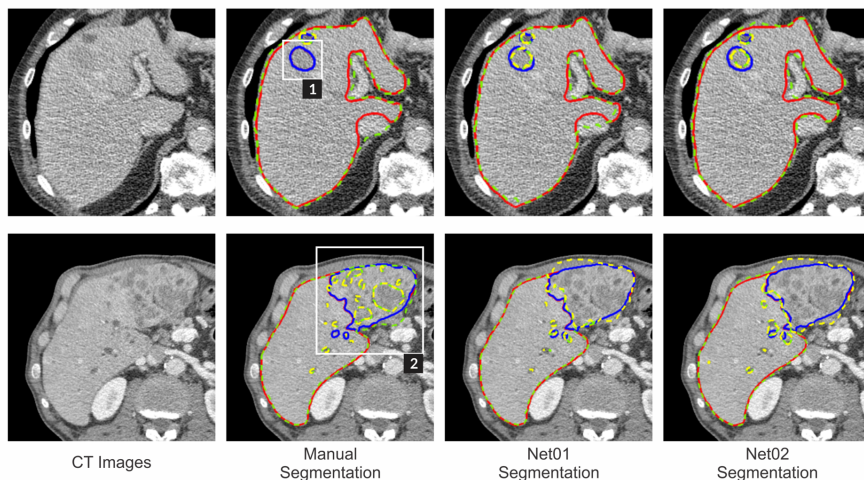


Figure 4.8: Selected segmentation results from the manual and automatic segmentation in comparison tests reveal two main differences. (Case 1-white box) A tumor was not identified by the segmenter. (Case 2-white box) A group of small tumors was identified separately instead of treated as a big tumor. Liver and tumor boundaries are represented by the green and yellow dashed lines in the segmentation result and the red and blue solid lines in the ground truth.

In tumor segmentation, the automatic method outperformed manual segmentation in both the Dice score ($78.4 \pm 16.7\%$ for Net01) and recall (recall $83.6 \pm 24.7\%$ for Net02). The highest scores achieved by manual segmentation were $67.6 \pm 24.4\%$ for the Dice score and $73.1 \pm 27.4\%$ for recall. The main differences between automatic and manual segmentation can be seen in Figure 4.8. Most participants struggled to detect tumors with similar intensity to the image background, as indicated by the white box in Figure 4.8 Case 1. In addition, participants tended to identify nearby tumors as separate entities, while the network grouped them together as a single tumor, similar to the ground truth segmentation (Figure 4.8 Case 2). Furthermore, when comparing the manual segmentation performed by our participants in this study to the ground truth manual segmentation (LiTS), the lower Dice score obtained could indicate different levels of clinical expertise.

4.4 Conclusion

This chapter presents a comparison of network performance in automatic liver and tumor segmentation using a 2.5D model with different parameter configurations. Our results demonstrate that networks utilizing multiple stacked slices achieve higher Dice scores compared to networks using a single slice. Furthermore, it was observed that the network with three slices achieved the highest score while adding more slices decreased the score. The application of contrast enhancement methods to the input image did not show statistically significant results in liver and tumor segmentation. Further studies with a larger sample size are needed to verify the effect of image contrast on network performance. When it comes to network layers, increasing the number of layers improved tumor sensitivity. However, without additional post-processing to filter out false positives, this increase also led to a reduction in the tumor Dice score.

Based on the findings of this study, a clear correlation between parameter configuration and network performance was observed. Therefore, it is recommended to explore different configurations of network parameters to further improve the segmentation result.

The development of an automatic method for liver and tumor segmentation offers benefits to clinicians by providing faster segmentation with high accuracy. However, further improvements are required. Implementing liver detection can help reduce the processing time by focusing only on slices containing the liver. Additionally, incorporating a combination of 2D and 3D convolutions in the network structure to provide 3D context information may contribute to improved segmentation outcomes [114]. Advanced post-processing techniques for tumor segmentation are also necessary to enhance accuracy. Additionally, the application of neural networks for image segmentation is not limited to CT images. With suitable modifications to the network and dataset, it can also be adapted for use with MR images, which are being increasingly utilized in medical practice due to their lower associated risks.

5

Design and Characterization of an MRI-Guided Robot for IRE

Adapted from: Girindra Wardhana et al. “Design and Characterization of a Multiple Needle Insertion MRI-guided Robot for Irreversible Electroporation (IRE) Treatment”. In: *2022 9th IEEE RAS/EMBS International Conference for Biomedical Robotics and Biomechatronics (BioRob)*. 2022, pp. 1–6.

Abstract

Irreversible electroporation (IRE) is a promising tumor treatment that uses an electric field to kill tumor cells. During treatments, 2-6 needles are inserted around the tumor, preferably placed in parallel and located at the same depth. This allows the electric field to be effectively distributed across the cell to destroy tumors. In this chapter, we present a body-mounted robot with four degrees of freedom ($140\text{ mm} \times 147\text{ mm} \times 113\text{ mm}$) designed to assist in multiple needle placements under Magnetic Resonance Imaging (MRI) guidance. The robot and the actuators can be classified as an MR-safe system, where the material composition consists of non-metallic, non-magnetic, and non-conductive materials to allow safe operation inside the MRI scanner. The accuracy of the robot was evaluated, and the maximum translation error was $0.72 \pm 0.26\text{ mm}$ on the horizontal axis and $1.60 \pm 0.75\text{ mm}$ on the vertical axis. The compatibility of the robot with MRI was evaluated and no artifacts or changes to the signal-to-noise ratio were observed in the MRI images. The proposed robot was able to cover the target tumor area and support the placement of multiple needles for IRE treatment.

5.1 Introduction

Various modalities have been developed as minimally invasive treatments for liver tumors. Cryoablation, microwave ablation, and radiofrequency ablation are commonly used alternatives to surgical resection for larger tumors [116]. However, these techniques have drawbacks, such as the potential damage to vital structures near the liver [117], and the possibility of incomplete ablation due to heat dissipation in larger vessels caused by local blood flow [118].

Irreversible electroporation (IRE) is a non-thermal ablation technique that has shown promising results in treating liver tumors. IRE applies sufficiently high electric fields to tumor cells, which induces a permanent opening to the cell membrane and leads to cell death. [119]. IRE has several advantages over other tumor treatments, including the preservation of vital structures from thermal injury and the avoidance of the heat sink effect [30].

Accurate positioning and placement of needles into tumors are essential in IRE to ensure complete tumor removal [120, 121]. Multiple needles are required and need to be placed in parallel and at equal depth for effective tumor ablation [122]. In small tumors ($< \varnothing 3$ cm), two needles are typically sufficient, while larger tumors ($> \varnothing 3$ cm) may require up to six needles [123].

There has been a growing interest in using robots together with magnetic resonance imaging (MRI) to accurately place needles [43]. An advantage of this technique is that the robot can be adjusted inside the MRI bore to achieve accurate needle placement. This may reduce the number of times the patient needs to be in and out of the MRI bore for needle adjustment which is expected to significantly reduce the procedure duration. In addition, specific MRI sequences can be used to measure the electric field radius during tumor treatment, which may help predict the tissue ablation coverage in IRE [124].

The MRI safety of the robot should be identified clearly before it can be used in the Magnetic Resonance (MR) environment. According to the ASTM F2503 standard, the safety of medical devices can be labeled into three categories: MR safe, MR conditional, and MR unsafe. Based on this classification, the robot material should be carefully selected in the design process in order to build an MR-safe robotic system.

How the robot is fixed and mounted should also be considered. The robot can be fixed to a table, floor, or scanner bed. This provides a rigid platform and allows the robot to be directly registered to the scanner workspace, which improves the accuracy of needle positioning. A commercial computed tomography (CT)-guided robotic system (Maxio, Perfint Healthcare, USA) offers a solution for needle insertion, increasing needle placement accuracy compared to the manual placement of IRE probes [37]. However, movements that may occur during insertion due to organ motion or tissue deformation may need to be corrected manually, increasing the procedure time.

Another option is to mount the robot to the patient's body, where the robot is fixed directly to the patient's skin or MRI coil. In this way, the robot moves together with the patient, which is less vulnerable to misregistration of the guidance image due to organ motion. Several patient-mounted robots have been developed for percutaneous intervention. A shoulder-mounted robot with four degrees of freedom (DOF) [125], had two identical stages that implemented a scissor mechanism to achieve a large workspace within a compact model. Hungr et al. developed a light puncture patient-mounted robot with a workspace of 135 mm × 120 mm [126]. This five-DOF robot inserted needles into thoracic and abdominopelvic regions under CT and MRI guidance. Li et al. developed a fully actuated six-DOF robot with needle alignment and a needle driver module that assisted injection into the lower back with a workspace of (∅80 mm) [127].

Although various patient-mounted robots with a large workspace have been developed, most of these systems do not support multiple needle insertion. Wu et al. developed a compact patient-mounted robot that supported the insertion of multiple needles [128], but only through a single entry point. Using this system for the case of multiple needle entry points would require an adjustment step for each insertion. He et al. developed small patient-mounted robots that could treat multiple tumors in different locations [43]. However, this system was not suitable for treating larger tumors where multiple needles have to be inserted close together. The minimum distance between the needles is limited by the robot dimension since the insertion of multiple needles was accomplished by using several robots.

In our study, a patient-mounted robot has been developed that can support multiple needle insertion for IRE treatment of tumors in the liver, pancreas, and abdomen area. The proposed system can position multiple needles using a single device with a large workspace ($\varnothing 119$ mm), and offers a solution to the multiple entry points and the electrode minimum distance problem seen in previous robot designs. The robot and actuators were made using MRI-compatible materials, enabling the robot to operate under the MRI scanner. We validated the performance of the proposed robot and the compatibility of the robot material with MRI.

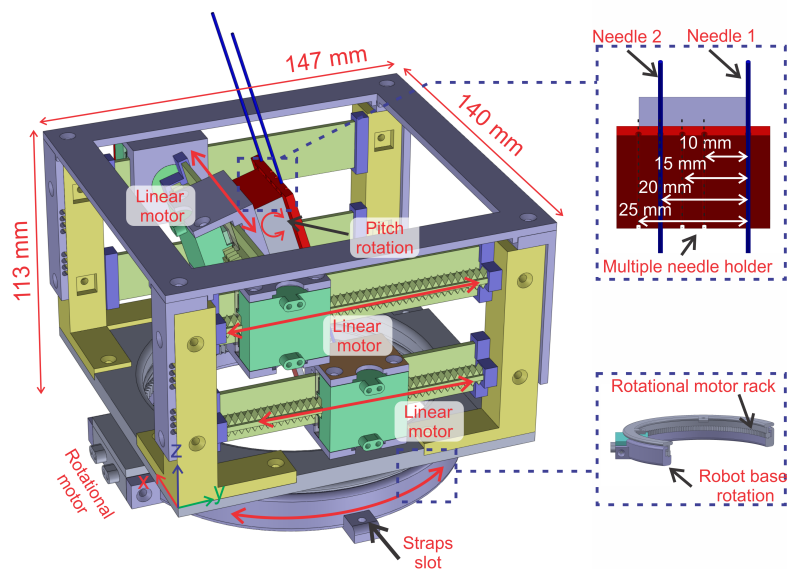
5.2 Methodology

5.2.1 Robot Design Requirements

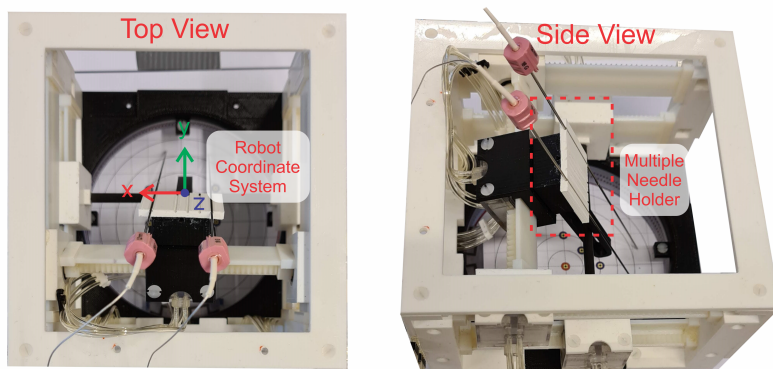
The main goal of the proposed robot is to help clinicians position electrodes under MRI guidance. To achieve this goal, the following points were considered when designing the robot:

1. Robot components made using nonmetallic, non-magnetic, and non-conductive materials
2. Actuators can operate safely inside the MRI
3. The robot is not too heavy, especially for the patient-mounted model
4. The robot fits within the dimensions of the MRI bore.
5. The robot has enough space to accommodate multiple needles

The robot was designed to operate within a Magnetom Aera 1.5T MRI scanner (Siemens AG, Munich, Germany) with an open-bore design and a 700 mm diameter. The robot was secured directly to the patient's body using belts that were connected to the table and the strap slots in the base of the robot. The robot was mounted on the abdominal area, so needed to be less than 350 mm high. A robot width of less than 200 mm was chosen based on the median abdominal diameter of men and women [129].



(a)



(b)

Figure 5.1: (a) CAD model of body-mounted robot prototype showing the multiple needle holder, robot degree of freedom and dimensions (given in mm). (b) Robot prototype detail in top and side view

Moir et al. [130] showed that IRE can treat a tumor size of 1-7 cm. To cover the minimum tumor size, the robot must be able to position the needle with an error of less than ± 5 mm. To achieve complete tumor ablation, a safety margin of 5-10 mm should be considered during IRE treatment [131]. Therefore, the robot workspace should cover the maximum tumor size as well as an additional safety margin ($> \varnothing 90$ mm). The electrodes should be placed parallel to each other, although small deviations may be required to place all electrodes in the desired position. IRE protocol allowed for a maximum angulation of 10° to ensure a homogeneous distribution of the electric field [132].

5.2.2 Overview of Robot Structure

The robot components were 3D printed with Makerpoint Ultimaker Tough PLA material (Makerpoint Holding, Wageningen, The Netherlands) and were fixed together using nylon screws and bolts. These materials were chosen because they are lightweight and MRI-compatible. After all components were assembled, the robot had a total weight of 240 g and dimensions of 140 mm \times 147 mm \times 113 mm. The DOFs and dimensions of the robot prototype are shown in Figure 5.1.

The robot was designed to guide the simultaneous insertion of two electrodes at a fixed distance of 10-25 mm. A multiple needle holder in the robot ensures parallel placement of the electrodes (Figure 5.1). The distance between the electrodes must be at least 10 mm and not exceed 20-25 mm for optimal treatment [133, 26]. If more than two electrodes are required, they can be inserted in sequence, following a planned path to avoid collision of the electrodes with the robot frame.

The robot had four pneumatic motors, each of which provides actuation to four separate joint states q_1 , q_2 , q_3 , and q_4 , as shown in Figure 5.2. Motor q_1 provides translation along the x axis (1st DOF). Motor q_2 and q_3 are mounted in parallel to provide translation along the y axis when moved together (2nd DOF) and rotation around the x axis when moved differentially (3rd DOF). Finally, motor q_4 provides rotation around the z axis (4th DOF).

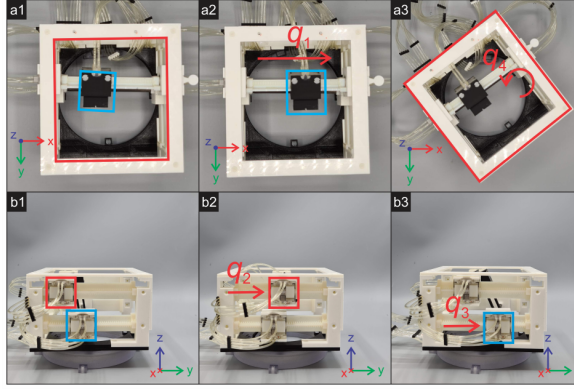


Figure 5.2: Joint motion of the robot, with (a1) robot top view showing (a2) translation motion in x axis by motor q_1 and (a3) rotation motion in z axis by motor q_4 ; (b1) Robot side view showing two translation motion in y axis for (b2) motor q_2 and (b3) motor q_3 , combined translation for pitch motion in the robot.

Joint movement in the robot was actuated using pneumatic stepper motors [134] that were produced at the University of Twente. The motor was 3D printed with Stratasys Objet Eden260 (Stratasys Ltd., Eden Prairie, MN, USA) using FullCure720 material. Two types of motors were used: a linear motor and a rotational stepper motor. The resolution of the motor depends on the size of the stepper teeth/rack. The smallest step size for the linear motor was 0.625 mm, and the minimum angle for the rotational motor was 0.5° . The motor position and joint motion of the robot prototype are shown in Figure 5.2.

5.2.3 Forward Kinematics

Two intermediary variables θ and d_{target} , (Figure 5.3), were used to derive the forward kinematics. θ represents the change in orientation around the x axis due to q_2 and q_3 , while d_{target} is the needle translation along the y axis at $z = 0$. Other variables, such as the horizontal distance between the center of the top motor and the needle position ($d_{\text{needle}} = 26$ mm), the vertical distance of q_2 and q_3 ($l_{\text{motor}} = 40$ mm), and the vertical distance between the target at $z = 0$ and q_3 ($l_{\text{target}} = 51.9$ mm), were derived from the robot prototype dimensions.

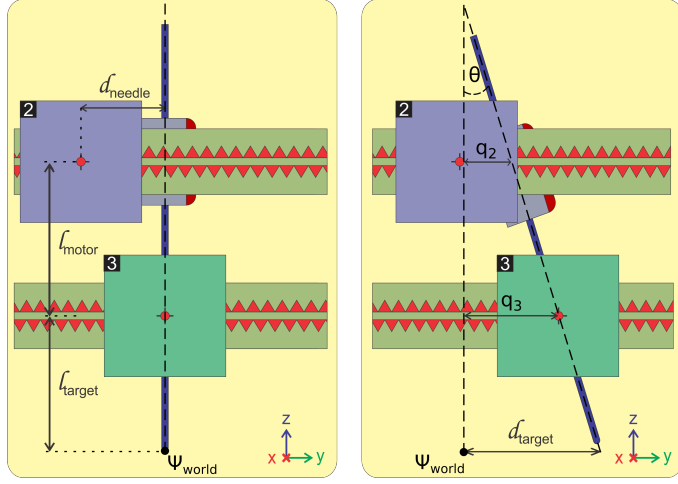


Figure 5.3: Diagram showing the robot geometry in the y - z plane. The initial reference configuration of the robot is shown in the left image, where the needle is located at the center of the workspace pointing straight downwards, using actuator configuration $\mathbf{q} = [q_1, q_2, q_3, q_4]^T = [0, 0, 0, 0]^T$. The needle orientation around the x axis is adjusted by the motion of motor q_2 and q_3 in the y axis as shown in the right image.

The orientation change θ can be written in terms of q_2 and q_3 by:

$$\theta = \text{atan2} \frac{q_3 - q_2}{l_{\text{motor}}}. \quad (5.1)$$

Furthermore, d_{target} can be calculated by extrapolating the line made by two points $(\bullet, q_2, l_{\text{motor}} + l_{\text{target}})$ and $(\bullet, q_3, l_{\text{target}})$ to the reference target plane at $z = 0$.

$$d_{\text{target}} = \frac{l_{\text{target}}}{l_{\text{motor}}} (q_3 - q_2) + q_3. \quad (5.2)$$

Finally, the mapping from the actuator space to the end effector space is given by the transformation matrix T_{ee} . It is obtained by compounding the transformation for each degree of freedom, including the insertion motion:

$$\mathbf{T}_{\text{ee}} = \mathbf{T}_{q_4} \mathbf{T}_{d_{\text{target}}} \mathbf{T}_{\theta} \mathbf{T}_{q_1} \mathbf{T}_{q_{\text{insert}}}, \quad (5.3)$$

$$T_{ee} = \begin{bmatrix} \mathbf{R}_{q_4} & \mathbf{0}_{3 \times 1} \\ \mathbf{0}_{1 \times 3} & 1 \end{bmatrix} \begin{bmatrix} \mathbf{I}_{3 \times 3} & \begin{bmatrix} 0 \\ d_{\text{target}} \\ 0 \end{bmatrix} \\ \mathbf{0}_{1 \times 3} & 1 \end{bmatrix} \begin{bmatrix} \mathbf{R}_\theta & \mathbf{0}_{3 \times 1} \\ \mathbf{0}_{1 \times 3} & 1 \end{bmatrix} \begin{bmatrix} \mathbf{I}_{3 \times 3} & \begin{bmatrix} q_1 \\ 0 \\ 0 \end{bmatrix} \\ \mathbf{0}_{1 \times 3} & 1 \end{bmatrix} \begin{bmatrix} \mathbf{I}_{3 \times 3} & \begin{bmatrix} 0 \\ 0 \\ q_{\text{insert}} \end{bmatrix} \\ \mathbf{0}_{1 \times 3} & 1 \end{bmatrix},$$

where \mathbf{I} is a 3×3 identity matrix, q_{insert} is the needle insertion degree of freedom (manually performed), and the rotation matrices are given by:

$$\mathbf{R}_{q_4} = \begin{bmatrix} \cos q_4 & -\sin q_4 & 0 \\ \sin q_4 & \cos q_4 & 0 \\ 0 & 0 & 1 \end{bmatrix}, \mathbf{R}_\theta = \begin{bmatrix} 1 & 0 & 0 \\ 0 & \cos \theta & -\sin \theta \\ 0 & \sin \theta & \cos \theta \end{bmatrix}.$$

5.2.4 Workspace Analysis

The robot workspace is limited by the motion of the pneumatic stepper motor and the collision of the needle with the robot frame at the target plane ($z = 0$). Using forward kinematics, the boundary of the workspace can be calculated by substituting q_1 , q_2 , q_3 and q_4 , which gives a cone-shaped boundary.

The cone-shaped robot workspace has a top diameter of 119.18 mm for electrode insertion on the skin and becomes larger depending on the depth of the electrode. The robot can also support a large insertion angle normal to the skin surface, with a maximum tilt of 32.3° . With proper placement on the patient's body, the robot workspace is large enough to cover the maximum tumor size, including the safety margin for IRE treatment ($> \varnothing 90$ mm), and the maximum angulation for the electrode ($> 10^\circ$) as discussed in subsection 5.2.1.

5.3 Experiments and Results

The robot was controlled using Robot Operating System (ROS) Melodic in Ubuntu 18.04 operating system. The needle trajectory was calculated using the ROS MoveIT package. By providing the position of the target, MoveIT calculated the inverse kinematics of the robot while preventing collision of the joint position. After obtaining the joint position, Arduino Mega 2560 was used to activate the pneumatic valve and actuate the pneumatic motor into the desired position. Open-loop control was used to move the pneumatic motor based on the motor step.

5.3.1 Needle Accuracy Test

The accuracy of the robot in free air was tested by inserting a needle into the target points as depicted in Figure 5.4. We opted to use only a single needle in this accuracy test, as the additional needles will move together due to the rigid connection to the needle holder. The positioning error of one needle should not differ compared to multiple needles, since the motion between the needles are relative to each other. The error is mainly introduced by the fabrication accuracy of the 3D-printed needle holder, which has sub-millimeter accuracy.

Table 5.1: Robot positioning accuracy (in mm)

Needle angle	0 degree		5 degrees		10 degrees	
	T_x	T_y	T_x	T_y	T_x	T_y
Mean error [mm]	0.21	0.70	0.62	0.81	0.72	1.10
Std. deviation [mm]	0.14	0.50	0.18	0.53	0.26	0.66

Needle angle	15 degrees		20 degrees		25 degrees	
	T_x	T_y	T_x	T_y	T_x	T_y
Mean error [mm]	0.32	1.18	0.32	1.42	0.37	1.60
Std. deviation [mm]	0.21	0.73	0.23	0.61	0.29	0.75

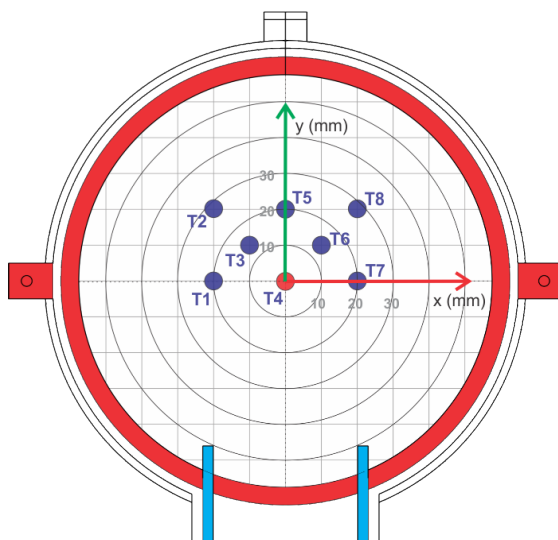


Figure 5.4: Overview of eight target positions (blue circles) that were located under the robot based on accuracy test

The robot was set to start at position T4 (the center of the robot coordinate) before moving to the other target points, from T1 to T8. The needle was inserted 15 times for each target and a variety of needle insertion orientations were also evaluated. In the first experiment, the needle was inserted parallel to the z axis. In the next experiment, the needle angle was increased incrementally by 5° until a maximum angle of 25° in the x direction.

The accuracy values of the robot are presented in Table 5.1. In a parallel position, the robot accuracies were 0.21 ± 0.14 mm for the x axis and 0.70 ± 0.50 mm for the y axis. We also found that the error increased in the direction of needle orientation. For instance, the position error in the y axis increased as the needle angle increased. This can be explained by the number of motors that were used to achieve the target position. On the axis where the orientation is given, two stepper motors were needed to control the needle tip, while on the other axis, only one motor was needed.

The accuracy in the z direction was not reported because the needle was inserted manually. This was intended to mimic the clinical procedure. Robot actuation is used to guide the needle to the desired position, and the clinician should be the one who has full responsibility and control over the insertion process due to regulation and safety concerns.

5.3.2 MRI Accuracy Test

We tested the ability of the robot to target several tumors in a triple modality 3D abdominal phantom (Model 057A; CIRS Inc., Norfolk, VA, USA) under MRI guidance. The robot was placed on top of the phantom, which left enough space inside the MRI bore. Fish oil capsules were used as fiducial markers on the phantom (four capsules) and robot (three capsules). The T2 sequence was used to obtain MRI images. The initial scan was performed with an image dimension of $768 \times 768 \times 192$ pixels and image spacing of $0.49 \text{ mm} \times 0.49 \text{ mm} \times 1 \text{ mm}$. From this scan, several important objects were segmented from the phantom, including phantom shell, liver, tumors, and fish oil markers, using 3D Slicer software [135].

In Slicer, these objects were manually segmented using pixel intensity information as guidance for object region and boundaries. Segmentation quality was improved using the painting tool to refine the object selection. These segmentations were exported to STL files and used for robot registration. Fiducial registration wizards from the SlicerIGT module [136] were used to register the segmentation files from MRI images to the robot coordinates.

Four tumors were selected as targets from the phantom. The accuracy of needle insertion in the axial and coronal planes was assessed. Robot inverse kinematics was used to calculate the required joint positions, using the center of the tumor as the target point. The needles were manually inserted, and the MRI images of the phantom were taken to evaluate the result.

Insertion results are shown in Figure 5.5. The distance between the needle tip and the tumor center was measured using 3D Slicer. In the coronal plane, the insertion error was $2.53 \pm 2.56 \text{ mm}$. In the axial plane, the accuracy was lower with an error of $8.73 \pm 1.95 \text{ mm}$.

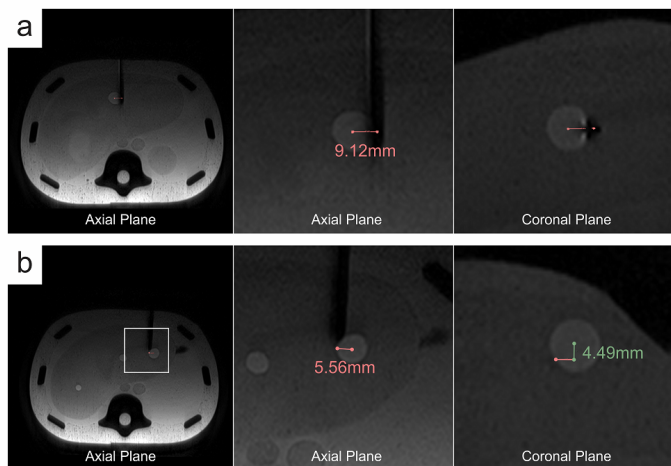


Figure 5.5: MR images of the abdominal phantom during MRI accuracy test

The observed error in registering the robot and MRI images may have contributed to the higher error observed in this experiment compared to the previous accuracy test result. Our finding, which indicates that deeper tumors have a higher error compared to tumors located closer to the skin surface, suggests that needle orientation error increases as the target depth increases. Needle deviation may also occur due to tissue compression deformation, which can also contribute to the error.

5.3.3 Image Quality Testing

The image quality test evaluated the effect of the robot on the quality of the MRI images. In this test, the robot was operated inside a Magnetom Aera 1.5T MRI scanner. A standard Siemens 1900 ml phantom plastic bottle (model# 8624186; 3.75 g $\text{NiSO}_4 \times 6\text{H}_2\text{O}$ + 5g NaCl) next to the robot was used to check the homogeneity of the MRI images. Scans were performed in three ways: (1) with a phantom only as a control image, (2) with a phantom and robot in the OFF state, and (3) with a phantom and robot in the ON state.

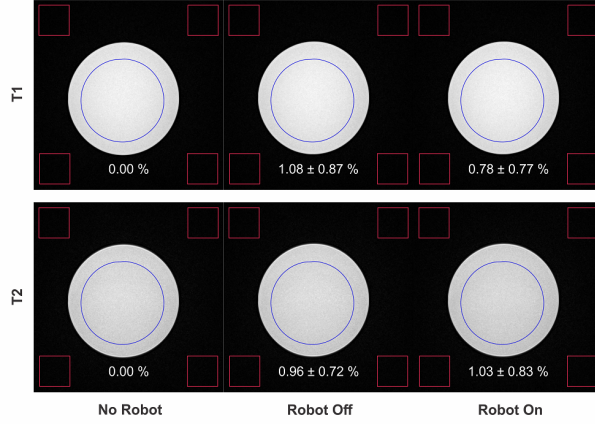


Figure 5.6: MR images of the phantom plastic bottle in three operating conditions with T1 and T2 image sequences. The ROI for signal and noise is represented by blue circles and red squares respectively.

Two image sequences, T1 and T2, were used during the test. The images for both sequences had a field of view of $320 \times 320 \times 20$ with a voxel size of $0.625 \text{ mm} \times 0.625 \text{ mm}$ and a slice thickness of 3.5 mm . The image quality was evaluated by measuring the signal-to-noise ratio (SNR) of the phantom MR images using the NEMA standard [137]:

$$SNR = \frac{\overline{S}_{\text{signal}}}{\sigma_{\text{noise}}} \quad (5.4)$$

where $\overline{S}_{\text{signal}}$ is the mean pixel value in the region of interest (ROI) of the signal and σ_{noise} is the standard deviation of all pixels in the ROI of the noise.

Figure 5.6 shows the ROI for both signal and noise, including the normalized SNR results. A maximum of 10% SNR loss is acceptable when demonstrating the MRI compatibility of the robot [138]. The maximum SNR decrease due to the robot presence was 1.08% for the T1 sequence and 1.03% for the T2 sequence. No significant differences were observed in the SNR between the ON and OFF states of the robot, and no artifacts were observed in the MRI images. Thus, our robot prototype can be safely used in an MRI scanner bore.

5.4 Conclusion

We have presented the design, fabrication, and validation of the four-DOF robotic system that supports multiple needle insertion using MRI guidance.

The robot and actuator were fabricated using non-metallic, non-magnetic, and non-conductive materials (PLA and FullCure720) so that the robot could be operated safely inside the MRI scanner. The robotic system can be classified as MR safe robot based on the material composition. Robot performance was evaluated with a needle accuracy test in free air and needle insertion to target tumors on a phantom inside the MRI scanner. Additionally, an image quality test was performed to assess the effect of the robot's presence on the quality of MRI images.

The main limitation of this system is the absence of sensor feedback to determine the real-time position of the motor. Although the accuracy of the stepper motor in this robot prototype is quite high, untracked motor errors can accumulate over time, which can affect robot performance. In the future, we plan to embed sensors into the robot to track the position of the motor in real-time. We also plan to reduce the rack size on the motor to fine-tune the position and the orientation of the needle [139]. Finally, an interface needs to be developed to help clinicians insert needles using the robotic system.

6

Robotic Grid System for Parallel Needle Insertion in IRE

Abstract

Accurate placement of needles in Irreversible Electroporation (IRE) treatment is crucial in ensuring the success of the tumor ablation. Depending on the size and shape of the tumor, 2-6 needles are inserted in the region surrounding the tumor. Optimally, these needles are placed in parallel to obtain a homogeneous distribution of the electric field and to prevent thermal damage to the other vital tissue. In this chapter, a robot with two degrees of freedom is presented to assist in the insertion of multiple needles. The robot utilizes a grid system that enables multiple needles to be inserted simultaneously while maintaining the parallelism between the needles. The robot design allows for the adjustment of the grid angulation to accommodate targeting the lesion in various positions. The robot has a dimension of $\varnothing 134$ mm and a height of 46 mm, with a total weight of 295 grams. The performance of the robot was evaluated by testing its accuracy and the robot's ability to maintain parallelism. On the skin surface, the robot shows a maximum deviation on the needle orientation of less than 1° . This robot showed promising results and making it suitable for IRE procedures, where multiple parallel needle insertions are required.

6.1 Introduction

Irreversible Electroporation (IRE) is an emerging soft tissue tumor treatment technique. Unlike other heat-based ablation techniques, IRE applies short high-voltage electric pulses to destroy the tumor cell [8]. Multiple needles are inserted around the tumor and an electric field is applied between each pair of needles. The number of needles typically varies from 2-6 depending on the size and shape of the tumor.

Precise needle positioning is a crucial factor in determining the efficacy of tumor ablation procedures. In IRE, needles should be placed parallel to each other to obtain homogeneous electric field distribution [122, 140]. Converge placement of the needle will increase the risk of over-current which will lead to temperature rise and may cause thermal damage to surrounding tissue. Meanwhile, diverging needle position will cause insufficient coverage of the electric field which increases the risk of incomplete ablation.

In current medical practice, needle placement procedures are typically performed manually by clinicians. However, the utilization of robotic devices to aid in these procedures has been gaining popularity, as they have the potential to not only enhance accuracy but also reduce the duration of the procedure. The integration of robotic devices with image guidance has been explored in several studies, such as in the case of cryoablation [141], shoulder arthrography procedures [142], and low back pain injections [127].

With regards to IRE, various solutions have been proposed, ranging from simple devices such as needle spacers to maintain the distance and orientation between needles, to more advanced approaches like navigation systems and robotic devices. Commercially available systems such as Stereotactic Computed Tomography (CT)-guidance (CAS-ONE, CAScination AG, Switzerland) [9] and CT-Guided Robotic system (Maxio, Perfint Healthcare, USA) [37] have also been reported to provide accurate needle placement. These studies showed that robotic assistance results in a shorter procedure time, fewer punctures, and lower radiation dose compared to the manual placement of IRE probes.

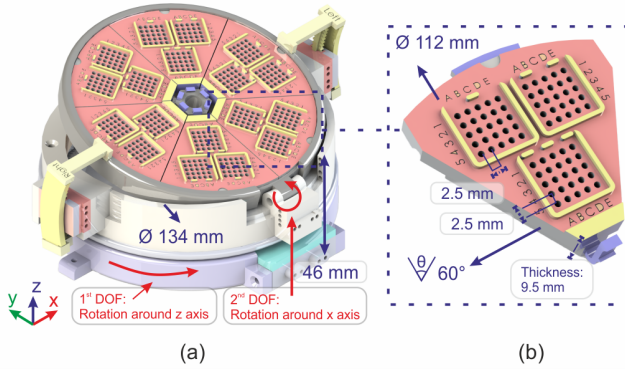


Figure 6.1: (a) Robotic grid system CAD model showing the degrees of freedom and the robot dimensions. (b) The subgrid element has 3 main groups of 5×5 array of holes with a diameter of 1.5 mm.

Despite the recent advancement in needle placement technology, there is limited literature available on devices that support multiple needle insertions. For instance, small patient-mounted robots developed by He et al. [43] were used to perform multiple needle insertions for tumor treatment. They used several robots to insert multiple needles in various locations. This approach is not applicable for IRE due to the limitation of the distance between the needle pair, which range needs to be 10-25 mm. For the application of commercial systems in IRE, they performed needle placement by inserting needles one by one. This approach requires proper adjustment to each needle, especially to maintain parallelism, in addition to accurate placement of the needle tip.

To address this gap, we propose a novel robotic grid system for multiple parallel needle insertion in IRE treatments. The proposed system has two degrees of freedom (DOF) implemented in the grid system to support the angulation of the needle path to accommodate insertion in complex multi-angle situations. This system represents an improvement over the previous robot that our research group has developed [115]. Two types of tests were performed to evaluate the accuracy of the system and the capability of the robot in maintaining parallelism for multiple needle insertion.

6.2 Methodology

6.2.1 Mechanical Design and Fabrication

The robot design was inspired by the precision grid used in breast biopsy. Figure 6.1 shows the design of the robot grid system. The precision grid provides a visual guide for the needle's path, helping to ensure that the needle is placed in the correct location. Localized needle entry help to obtain a reproducible and consistent placement with the needle. In addition, the precision grid can be easily incorporated into the standard medical procedure and does not require specialized training. Furthermore, the main advantage of utilizing a precision grid in IRE is the ability to simultaneously insert multiple needles with the same orientation, eliminating the need for individual needle adjustment and reducing procedure time. These factors were the reason for selecting this concept to be implemented in our robot design.

In conventional precision grids, the needle must follow the pre-determined path outlined by the grid. It limits the maneuverability of the needle, especially when deviation occurred which reduces the accuracy of the needle placement. Moriera et al. [143] introduce an angulated needle-guide template for answering this problem, where the needle orientation can be adjusted by angulated grid template system instead of adjusted manually by the clinician. Although that approach can reduce the deviation of the needle, it supports only a single needle insertion since the application is for prostate biopsy. We adopt the idea and improved the robot design in order to manage the multiple needle insertions required in the IRE procedure.

In our robot design, we incorporated pneumatic stepper motors to enable orienting the needle grid. These motors are using double-acting cylinder mechanism, as presented in the work of Groenhuis et al.[134]. Each motor is controlled by four pneumatic tubes made of polyurethane. The robot system has two degrees of freedom (DOF), which consist of rotation around the z-axis (1st DOF) and x-axis (2nd DOF) as shown in Figure 6.1a. The resolution of the motors is affected by the size of the stepper teeth or rack. In this design, the resolution for both stepper motors is 0.5° , with a motor range of up to 360° for rotation in the z-axis and 20° for rotation in the x-axis.

The robot incorporates a grid system that comprises six subgrids that are assembled together on the main robot frame. The subgrids have a diameter of 112 mm and a thickness of 9.5 mm. They are attached to the robot frame using a snap-fit mechanism, which allows for the easy removal of unused subgrids to increase the available space in the robot's workspace. It also allows for the subgrid to be sterilized independently without the need to include the whole system. Additionally, this design facilitates individual modification to the size of the grid hole. Each subgrid is composed of three main groups of 5×5 arrays of equally spaced holes with a distance of 2.5 mm. The current grid system has a hole diameter of 1.5 mm, to accommodate the common size of electrode diameter used in IRE (18G). A naming convention is used to identify the location of each hole within the subgrid, making it easy to locate and select the desired hole. For instance, a hole with an ID of '5-iii-B4' means the hole is located at subgrid 5, group iii, column B, and row 4.

The robot body, including the grid system and frame, was fabricated using a 3D printer with Makerpoint Ultimaker Tough PLA material (Makerpoint Holding, Wageningen, The Netherlands). The pneumatic motors and the racks were printed using Stratasys Objet Eden 260 with FullCure720 material (Stratasys Ltd, Eden Prairie, MN, USA). The components were assembled using nylon screws and bolts, resulting in a robot with a dimension of 134 mm in diameter and 46 mm in height, with a total weight of 295 grams. This lightweight and plastic-based design allows for the safe operation of the robotic grid system inside an MRI bore and enables direct mounting of the system on the patient's body.

6.2.2 Kinematic Analysis

A transformation matrix can be derived to calculate the position of the needle tip with respect to the robot's coordinate system. Two variables, q_z and q_x represent the orientation of the robot frame in the z and x-axis, respectively. Other variables, such as h_{axis} and h_y are obtained from the physical dimensions of the robot body and are equal to 37.8 mm and 61.5 mm, respectively. h_{axis} is the height of the x-axis rotation from the robot body, and h_y is the shifting distance of the x-rotation from the center of the robot. By combining

the transformation for each degree of freedom with the location of the selected grid hole and the length of the insertion, the following transformation matrix for the end effector can be obtained.

$$T_{ee} = T_{q_z} T_{h_{axis}} T_{q_x} T_{q_{insert}}, \quad (6.1)$$

$$T_{ee} = \begin{bmatrix} \mathbf{R}_{q_z} & \mathbf{0}_{3 \times 1} \\ \mathbf{0}_{1 \times 3} & 1 \end{bmatrix} \begin{bmatrix} \mathbf{I}_{3 \times 3} & \begin{bmatrix} 0 \\ 0 \\ h_{axis} \end{bmatrix} \\ \mathbf{0}_{1 \times 3} & 1 \end{bmatrix} \begin{bmatrix} \mathbf{R}_{q_x} & \begin{bmatrix} 0 \\ h_y \\ 0 \end{bmatrix} - \mathbf{R}_{q_x} \begin{bmatrix} 0 \\ h_y \\ 0 \end{bmatrix} \\ \mathbf{0}_{1 \times 3} & 1 \end{bmatrix} \begin{bmatrix} \mathbf{I}_{3 \times 3} & \begin{bmatrix} x_{grid} \\ y_{grid} \\ q_{insert} \end{bmatrix} \\ \mathbf{0}_{1 \times 3} & 1 \end{bmatrix},$$

where \mathbf{I} is a 3×3 identity matrix, x_{grid} and y_{grid} are the coordinate of the grid hole, and q_{insert} is the length of needle insertion.

Rotation matrices are given by:

$$\mathbf{R}_{q_z} = \begin{bmatrix} \cos q_z & -\sin q_z & 0 \\ \sin q_z & \cos q_z & 0 \\ 0 & 0 & 1 \end{bmatrix}, \mathbf{R}_{q_x} = \begin{bmatrix} 1 & 0 & 0 \\ 0 & \cos q_x & -\sin q_x \\ 0 & \sin q_x & \cos q_x \end{bmatrix}.$$

6.2.3 Reachability analysis

The arrangement of the grid hole imposes limitations on the reachable regions under the robot body. However, this reachable region can be modified by adjusting the position of the grid system. By utilizing the derived transformation matrix for the end effector, it is possible to estimate this region in relation to the orientation of the grid.

The reachable region is determined through the mapping of distances between the needle tip and the surrounding area. This mapping method allows for the classification of specific locations as reachable or not reachable.

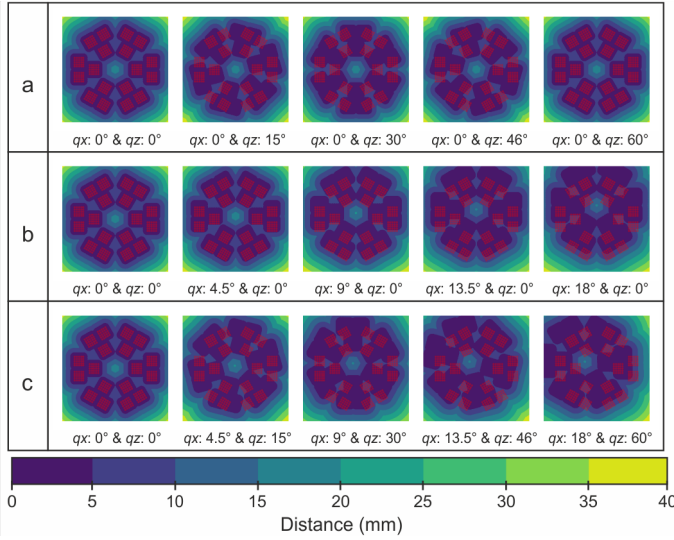


Figure 6.2: Reachable region of the robot grid in various robot orientations, including (a) rotating only in the z-axis, (b) rotating only in the x-axis, and (c) combination of rotation in the z and x-axis. A group of red dots represents the position of the subgrids when there is no orientation given to the robot.

In this study, three schemes were used to observe the reachable region with a particular emphasis on the area located beneath the robot frame ($z=0$). These schemes included rotating the robot grid:

1. only in the z-axis, from 0° to 60° with a 15° increment
2. only in the x-axis, from 0° to 18° with a 4.5° increment
3. combination of the z and x-axes using the values from (1) and (2)

The reachable region from the robot grid varies with different grid orientations, as shown in Figure 6.2. In Figure 6.2a, the reachable region remains consistent every 60°, when rotation is applied only in the z-direction. The reachable region from $q_z = 60^\circ$ yielding the same results as $q_z = 0^\circ$, due to the grid design's symmetry. In Figure 6.2b, applying rotation only in the

x-axis shifts the reachable region away from the x-axis, with the distance increasing with higher rotation. For difficult positions, such as areas located farther from the center of the grid, combining rotations in both the z and x-axes can provide an effective solution, as demonstrated in Figure 6.2c.

From this result, it is worth mentioning that the rotation in the x-axis has an important role in reaching the region that is located further away from the robot center. Also, the result is mainly correlated with the depth of the target. The results of the second and third schemes will be significantly different when the target is located in a deeper location. Furthermore, it is important to know that reaching a position in the corner by adjusting the orientation of the grid in x and z, will give a unique pose to the needle position and orientation. If the target required a specific path to be followed, it will be easier to readjust the robot system and redo the planning.

6.3 Experiments

Two tests were performed to evaluate the robot grid: the system accuracy test and the needle alignment test. The former analyzed the capability of the robot to precisely target designated points with varying robot configurations and target depths. The latter examined the ability of the robot to maintain needle parallelism, a vital aspect for the successful completion of IRE treatment.

6.3.1 Experimental Setup

Figure 6.3 shows the experimental setup for robot grid evaluation. The robot grid is operated through the Robot Operating System (ROS) Melodic. Users input the desired angle target along the z-axis and x-axis for the robot grid, and the required number of steps is calculated based on the motor resolution. No feedback is implemented in the system, thus the relative angle from the previous grid position is employed to monitor the current orientation of the grid system. To ensure proper operation, the robot position must be calibrated initially by positioning it at the home position, a configuration in which no rotation occurs around the x and z axes.

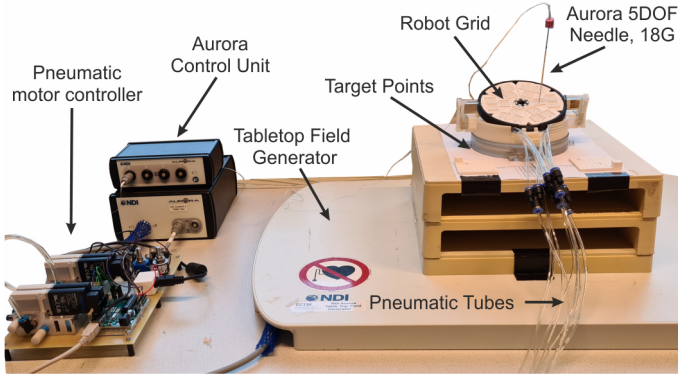


Figure 6.3: Experiment setup for evaluating the robot grid system, including robotic system, Aurora electromagnetic tracker system, and control board for pneumatic motors.

During the experiment, the pneumatic motor was actuated with an air pressure of 3 bar. The activation of the pneumatic valve was controlled by an Arduino Mega 2560, which was connected to ROS. The position and orientation of the needle tip were tracked using the Aurora 5-DOF needle. The robot body was located on the Tabletop Field Generator, which is an electromagnetic tracking system as part of Northern Digital's Aurora (NDI, Waterloo, Canada).

6.3.2 System Accuracy Test

The accuracy of needle placement was evaluated using a series of experiments in which the target points were located at varying depths under the robot. The insertion was performed in free space to evaluate the robot's accuracy without being affected by other factors, such as the interaction between needle and tissue. The origin of the robot coordinate system was set at the center of the robot grid (Figure 6.4a). The reported error is the average Euclidean distance in the x and y-axis between the target position and the needle tip position. Since the needle insertion was manually performed during the experiment, reported in-plane targeting errors do not account for errors in the z-axis.

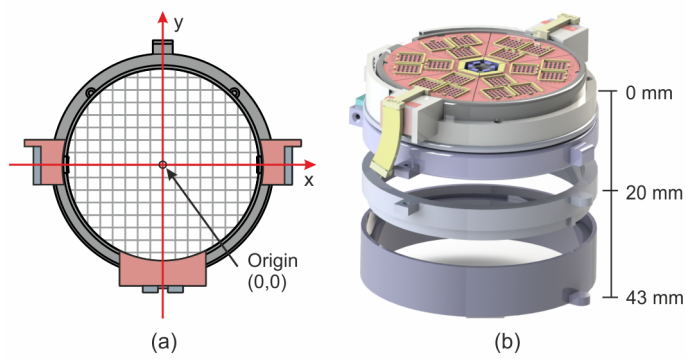


Figure 6.4: Experiment setup for accuracy test where (a) the origin of the robot coordinate system, and (b) different frame heights to introduce specific depth to the target location.

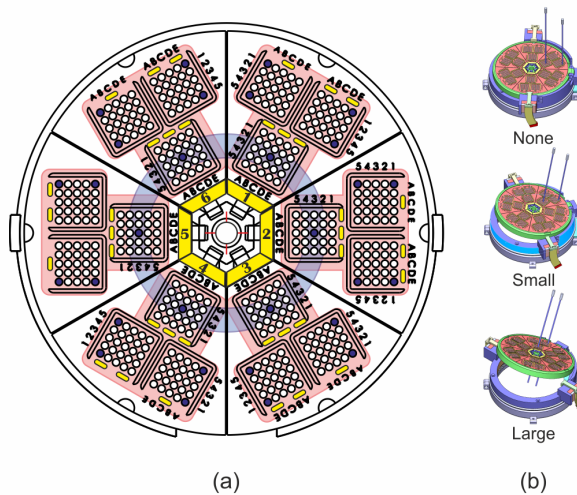


Figure 6.5: (a) Target holes for parallelism check, with red-colored region representing the holes used for the same subgrid test and blue-colored region for holes used in all grid tests. (b) Three variations of the robot orientation are introduced to investigate its effect on the needle orientation

The insertion locations were spread over the grid system. Needles were inserted through hole 'x-iii-C5', where x indicates the subgrid number (1-6). Various combinations of orientation in the z and x-axes were applied, where the insertion angle in the z-axis varying from 0-60° with 1.5° increment and the insertion angle in the x-axis from 0-18° with 0.5° increment. For each orientation and subgrid position in the grid system, the needle insertion was repeated five times. After targeting each point, the robot returned to the home position.

In addition to the previous test, two different frame heights, 20 and 43 mm, were introduced (Figure 6.4b). These frames were added to introduce depth to the target location. At each height, the initial step for the test was to perform registration of the EM sensor with respect to the robot coordinate system. Then, the insertion with various grid orientations was repeated following the previous procedure.

6.3.3 Needle Alignment Test

The orientation of the needles was evaluated when they were inserted using the robot grid in various grid hole locations. Two types of tests were performed as depicted in Figure 6.5a. The first test assessed the orientation of the needle when inserted through multiple holes within a single subgrid. The selected holes included 'x-i-A1', 'x-i-A5', x-ii-E1, x-ii-E5, and x-iii-C5, with x indicating the subgrid number. The second test compared needle orientations among different subgrids inserted through the hole 'x-iii-C5'. This test ensures that the robot is able to maintain consistent orientation regardless of the hole selected during insertion.

In addition to the grid location, the impacts of grid rotation on needle alignment were also investigated. Three different positions were evaluated during the recording of needle orientation. These positions included no rotation, small rotation, and large rotation applied in the x and z axis as shown in Figure 6.5b. The orientation of the needles was recorded upon reaching the target position, with ten repetitions for each hole in each grid orientation.

6.4 Results

6.4.1 System Accuracy Test

For every combination of orientation, a comprehensive evaluation of the robot's accuracy was conducted by performing 30 insertions, which consist of 5 repetitions for each target hole located in the 6 subgrids. To minimize the impact of the target hole distribution on the robot's accuracy, the result from all subgrids were taken into account during the accuracy assessment. The final outcome from the accuracy test is presented in Figure 6.6.

When the target plane was located directly under the robot body ($H=0$ mm), the minimum error of 1.24 ± 0.13 mm was achieved when the orientation of the robot grid was 0° for both the x and z-axes. Meanwhile, the maximum error was recorded at 2.09 ± 0.66 mm when the robot grid was oriented at 60° for the z-axes and 18° for the x-axes. This outcome highlights the correlation between the angulation of the robot grid and the accuracy of the needle placement, with a higher angulation resulting in a greater error in the accuracy test.

A similar pattern of error was also noted when an additional frame was added to the test. For both frames of $H=20$ mm and $H=43$ mm, the minimum and maximum errors were recorded at 1.79 ± 0.38 mm and 2.47 ± 0.82 mm, and 2.31 ± 0.21 mm and 3.55 ± 1.34 mm, respectively. It was evident that an increase in target depth resulted in a corresponding increase in robot error.

6.4.2 Needle Alignment Test

In the first type of test, a total of 50 insertions were performed for each subgrid and each grid orientation. The orientations of the needle were recorded and the average results were calculated for each subgrid. The results of the first test are presented in Table 6.1. The deviation of the needle orientation is generally below 1° , for both R_x and R_z components, across all subgrids and grid rotations. However, an exception was observed in subgrid 6 when a large rotation was applied, where the highest deviation of $1.10^\circ \pm 0.54^\circ$ was recorded.

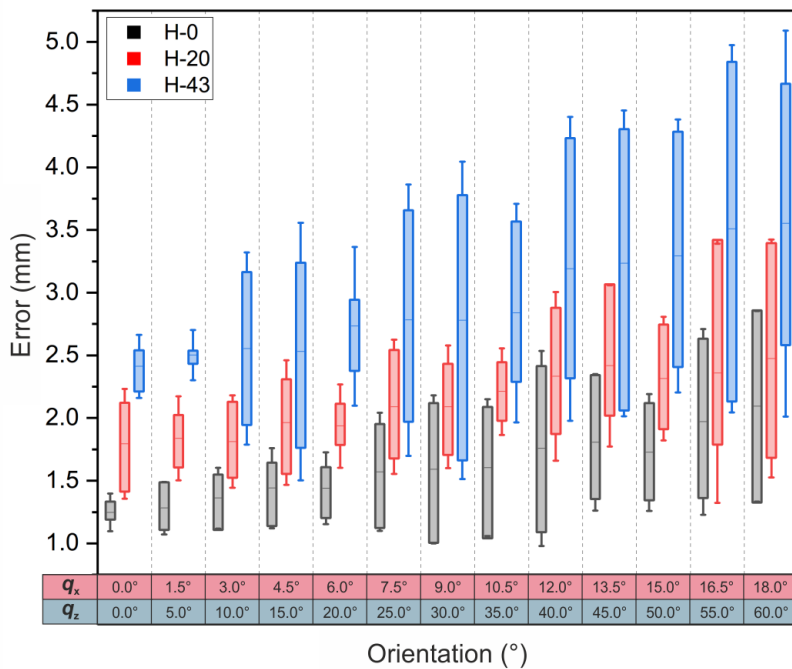


Figure 6.6: Needle targeting error versus the needle insertion angle and insertion depth. Insertion angle is introduced by applying rotation to the robot in the z and x-axis. Rotation in the z-axis is increased from 0° to 60° in increments of 5°, and rotation in the x-axis is increased from 0° to 18° in increments of 1.5°.

In the second type of test, a total of 60 insertions were performed across all subgrids for each grid orientation. The deviation of the needle orientation was slightly higher in comparison to the first test. Analysis of needle orientation results across all subgrids showed a maximum deviation of $1.52^\circ \pm 0.34^\circ$, with all results higher than 1° for all grid orientation, as presented in Table 6.2.

Table 6.1: Deviation of the needle orientation in degree ($^{\circ}$) for individual subgrid test

Orientation	Ind. Grid 1		Ind. Grid 2	
	R_x	R_z	R_x	R_z
None	0.75 ± 0.33	0.59 ± 0.25	0.53 ± 0.24	0.54 ± 0.25
Small	0.55 ± 0.24	0.59 ± 0.26	0.55 ± 0.30	0.60 ± 0.22
Large	0.86 ± 0.11	0.84 ± 0.35	0.66 ± 0.35	0.76 ± 0.34

Orientation	Ind. Grid 3		Ind. Grid 4	
	R_x	R_z	R_x	R_z
None	0.61 ± 0.24	0.80 ± 0.26	0.53 ± 0.13	0.72 ± 0.31
Small	0.65 ± 0.19	0.58 ± 0.20	0.46 ± 0.23	0.57 ± 0.27
Large	0.72 ± 0.32	0.61 ± 0.26	0.43 ± 0.19	0.52 ± 0.37

Orientation	Ind. Grid 5		Ind. Grid 6	
	R_x	R_z	R_x	R_z
None	0.57 ± 0.29	0.65 ± 0.30	0.46 ± 0.18	0.58 ± 0.24
Small	0.57 ± 0.25	0.48 ± 0.21	0.57 ± 0.28	0.55 ± 0.39
Large	0.41 ± 0.28	0.75 ± 0.32	0.66 ± 0.26	1.10 ± 0.54

Table 6.2: Deviation of the needle orientation in degree ($^{\circ}$) for all subgrid test

Orientation	All Grid	
	R_x	R_z
None	1.21 ± 0.32	1.39 ± 0.30
Small	1.52 ± 0.34	1.20 ± 0.22
Large	1.25 ± 0.26	1.37 ± 0.20

6.5 Discussion

The study presented the performance of the robot grid system for parallel needle insertion with support to angulate the needle insertion path to accommodate targeting the lesion in various positions. Two sets of tests were conducted to assess the accuracy of the system and its ability to maintain needle orientation. The results of the system accuracy test indicated that an increase in orientation leads to a corresponding increase in deviation from the target position. Moreover, a deeper target location results in a higher error in needle placement. The result of the needle alignment test demonstrated that the proposed robotic grid system is capable of maintaining parallelism of the needle insertion with minimal deviation, even when performed on different subgrids. As previously reported in our study [74], deviation of needle orientation exceeding 5° can significantly impact the outcome of IRE procedures. In this case, the robot can manage multiple needle insertion with deviation generally below 2° , which is within an acceptable range for IRE procedure.

In an ideal case, performing needle insertion in the free space using the robot grid would give precise needle placement. However, the potential sources of error in the experimental procedure may come from a variety of factors. It is including but is not limited to inaccuracies in the manufacturing of the robotic components, registration errors between the robotic coordinates and the electromagnetic tracker, and potential bending of the needle after repetitive tests. Based on our observation during the experiment, it was revealed that another factor contributing to the error is coming from the design of the grid hole used in the robot system. To demonstrate this phenomenon, an illustration of the needle positions within the grid hole is shown in Figure 6.7.

Ideally, a needle will follow a straight trajectory when inserted through a hole (Figure 6.7a). However, due to limitations encountered during the manufacturing of the grid components, a certain degree of space may be present within the hole grid, which may cause the needle to deviate from its intended trajectory, as demonstrated in Figure 6.7b. In such a scenario, the maximum deviation of the needle can be quantified by calculating the values of x_1 , x_2 , x_3 , and x_4 .

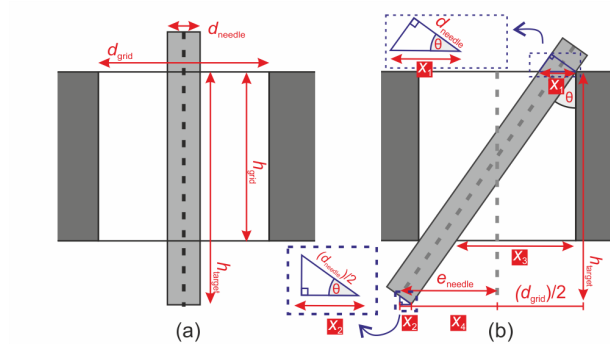


Figure 6.7: Illustration of needle position inside the hole grid, where (a) needle with a straight trajectory and (b) needle deviation due to the space present in the hole grid.

Assuming θ is small enough, where $\cos \theta \approx 1$, and knowing the dimension of d_{needle} and d_{grid} as the diameter of the needle and the grid, the value of x_1 , x_2 and x_3 are:

$$x_1 \approx d_{\text{needle}} \quad (6.2)$$

$$x_2 \approx \frac{d_{\text{needle}}}{2} \quad (6.3)$$

$$x_3 = d_{\text{grid}} - x_1 \quad (6.4)$$

Furthermore, with h_{grid} as the thickness of the grid and h_{target} as the depth of the target, x_4 can be calculated using the extrapolation made by the needle:

$$x_4 = \frac{h_{\text{target}}}{h_{\text{grid}}} (d_{\text{grid}} - d_{\text{needle}}) - \frac{d_{\text{grid}}}{2} \quad (6.5)$$

Finally, needle deviation (e_{needle}) can be calculated by substituting the value of x_2 and x_4 :

$$\begin{aligned} e_{\text{needle}} &= x_2 + x_4 \\ &= \left(\frac{h_{\text{target}}}{h_{\text{grid}}} - \frac{1}{2} \right) (d_{\text{grid}} - d_{\text{needle}}) \end{aligned} \quad (6.6)$$

In the design of our robot, the grid dimensions, d_{grid} and h_{grid} , are equal to 1.5 mm and 9.5 mm, respectively. An offset of 43.3 mm, which represents the distance from the top surface of the grid to the reference point on the robot's base, must be taken into account when determining the target depth, h_{target} . Meanwhile, for the needle dimension, the Aurora 5-DOF needle has a diameter of 1.05 mm. By utilizing these values, we can predict the maximum deviation that may occur to the needle when targeting specific positions at different depths. In our accuracy testing, where targets were located at depths of 0 mm, 20 mm, and 43 mm under the robot's base, the maximum deviations for the needle's position which are predicted using Equation 6.6, are equal to 1.83 mm, 2.77 mm, and 3.86 mm. These results are in accordance with the results obtained from the accuracy testing, which demonstrated that the errors for these specific depths were within the predicted ranges.

The impact of needle deviation caused by clearance in the grid hole is clearly visible in the result of the needle alignment test. When no rotation is applied to the robot, the deviation across all subgrids is relatively similar. However, when a large orientation is applied, the insertion depth varies between subgrids located near the axis of rotation in the x-axis and those located further away. As a result, subgrids 1 and 6, which are located at the farthest distance from the axis of rotation, have a longer distance to reach the target position, leading to higher deviation in the needle's orientation compared to other subgrids.

The results of the experiments have indicated a clear need for improvement in the design of the grid system, particularly regarding the clearance of the grid holes. Further studies should concentrate on exploring fabrication techniques that can produce a tighter grid for the robot system, which has been demonstrated to improve accuracy, as reported by McGill et al.[144]. It is also crucial to minimize the distance between the device and the skin surface to decrease deviation error. This is supported by the Equation 6.6 that shows that h_{target} contributes to needle deviation.

Another crucial aspect that needs attention is the absence of testing for targeting points within phantom or soft tissue. Conducting these tests with the robot is essential to determine the impact of the interaction between the needle and tissue on the accuracy of the robot. Based on these tests, a tailored

model can be established to predict needle deviation and minimize its effect, as demonstrated by Abolhassani et al.[145]. This will help to achieve more precise results for needle placement.

Given that the robot was fabricated using non-metallic, non-magnetic, and non-conductive materials, it is necessary to assess its compatibility within the MRI environment. This can be done by evaluating the robot's performance under MRI guidance and determining the effect of the robot's presence on MR image quality. Additionally, incorporating MR-visible markers into the robot's design is crucial for facilitating the alignment of the device's coordinate system with the MRI's coordinate system, thereby improving the accuracy of the registration process.

Finally, research into the positioning of the grid holes should be conducted. The configuration of the grid affects the areas that can be targeted using this robot system, particularly in the case of IRE treatment where a specific distance is required for effective ablation. This study can be combined with path planning software that provides automatic suggestions regarding the number of needles, position of needles, and insertion angle, taking into account both the patient's anatomy and the location of the tumor.

6.6 Conclusion

In this study, we presented the design and validation of a robotic grid system, capable of preserving needle parallelism during multiple needle insertions. The robot has 2 DOFs that allow for the adjustment of the grid angulation in the x and z axes through the use of pneumatic stepper motors. We performed a series of tests, including the system accuracy and needle alignment test, to evaluate the performance of the robot. The results showed that the robotic grid system has limited needle deviation and can be used to place multiple needles in parallel. This robot is suitable for IRE procedures and can be used for wider application of needle insertion procedures, such as microwave and radiofrequency ablation.

7

General Discussion and Conclusion

Irreversible electroporation (IRE) is a non-thermal ablation technique that utilizes an electric field to induce apoptosis in tumor cells. The electric field distribution within the targeted tissue is a crucial determinant of treatment success. To achieve irreversible electroporation, the intensity of the electric field must exceed a threshold that depends on tissue properties. Moreover, complete ablation requires complete coverage of the tumor area by the electric field, which relies on the appropriate configuration of treatment parameters.

This thesis aims to improve and enhance the efficacy of IRE treatment by investigating the effects of various treatment parameters. Computational models, including 2D and 3D models, have been developed to examine the influence of IRE parameters on the ablation area. Model validation has been conducted on animal and vegetable tissue, respectively, with detailed discussions presented in Chapters 2 and 3. To achieve a more accurate prediction of the ablation area, patient-specific models are required, for example by the incorporation of the tumor's actual shape. One approach to obtaining tumor shapes involves implementing a segmentation algorithm based on a deep learning network, which offers superior accuracy and faster processing times compared to manual segmentation, as elaborated in Chapter 4.

Needle placement significantly impacts the electric field distribution. To ensure electric field homogeneity and prevent thermal damage to adjacent tissues, several criteria must be met, including the parallel positioning of electrodes, consistent depth placement, and maintaining a specific distance between electrodes within a defined range. To accomplish these requirements, MRI-safe robotic devices have been developed to aid clinicians in inserting multiple electrodes during IRE treatment. Robot components were fabricated using 3D printing with plastic material, which is non-metallic, non-magnetic, and non-conductive. Various design approaches and assessments of the robot's performance are discussed in Chapters 5 and 6.

The following chapter discusses the design and evaluation of the computational model and robotic devices, highlighting the primary contributions, limitations, and future recommendations within this research field. Additionally, the steps toward clinical practice are explored, specifically focusing on the integration of robot-assisted intervention in IRE procedures.

7.1 Computational Model

7.1.1 Summary of the key results

Chapter 2 discussed the development of a 2D computational model, which was validated based on thermal monitoring on bovine liver tissue, to investigate the effects and relationships between parameters involved in IRE. The study examines several parameters, including pulse properties (pulse strength, pulse number, and pulse duration) and electrode configuration (electrode distance and active length), in terms of their impact on ablation coverage and the optimal parameter settings to maintain the temperature below the thermal damage threshold during treatment. Analysis of variance revealed that not all parameters had an equal effect on the ablation area and the temperature rise. The ablation area was significantly influenced by pulse strength ($P < 0.001$), while electrode distance ($P = 0.020$) and pulse strength ($P = 0.003$) significantly affected temperature rise. This experiment facilitated the calculation of the optimal IRE protocol to achieve maximum coverage area while preventing thermal damage to tissue.

Chapter 3 investigates the effect of needle orientation on electric field distribution by designing a 3D computational model, validated using potato tissue. Several variations in electrode position and orientation were tested, ranging from parallel placement to angulated placement in sideward and forward orientations, involving single and both electrodes. The needle was oriented around the center of the active length part, ranging from 0° to 15° with 5° increments. Measurements of potato conductivity and electroporation threshold yielded a result of 0.044-0.454 S/m and 375 V/cm, respectively. Model validations were conducted by comparing the electroporated area results between the simulation and experiment, achieving a mean Dice score of 0.727 ± 0.046 . Using the validated model, all needle orientations were tested to determine which orientation produced similar results compared to the parallel position. The ANOVA test revealed that as long as the orientation remained below 5° , the difference between the ablated areas in parallel and the electrodes in both sideward and forward-oriented positions was not significantly different.

Chapter 4 introduces a method for automatic segmentation of liver and tumor from CT images using a neural network based on a 2.5D model. This approach addresses the limitations of 2D models, which provide limited information for volume segmentation, while 3D models demand more memory and higher system requirements. Various factors were examined in this study, including the number of stacked layers in the input image, image contrast, and the number of network layers in building the network architecture. Results indicate that utilizing multiple stacked layers improves network performance compared to single-layer models. However, segmentation accuracy declines when the total number of stacked layers surpasses a certain number of layers. Contrast enhancement enhances object visualization, but does not significantly impact network performance. In general, adding layers to a network structure improves its ability to detect tumors but also increases the percentage of false-positive results, leading to a decrease in the overall Dice score.

7.1.2 Limitations and future challenges

The efficacy of IRE treatment depends on the electric field intensity applied to the tumor tissue. If the electric field intensity is lower than the tissue-specific electroporation threshold, irreversible electroporation will not occur. Conversely, if the intensity is much higher, tumor cells will undergo coagulation due to thermal damage rather than apoptosis. Ensuring complete coverage of the entire tumor region by the electric field is another crucial factor. The electric field distribution is influenced by the pulse parameter and electrode configuration employed during the treatment. Accounting for these three critical factors, tissue properties, pulse parameters, and electrode configuration in the computational model helps facilitate precise treatment planning.

Designing computational models for IRE presents the challenge of accurately modeling biological tissue. Numerous studies have calculated various tissue properties, including those of the brain [146], kidney [18], liver [147], pancreas [147], and prostate [148]. These studies have employed different models to describe the effect of electroporation on tissue electrical conductivity, such as static models [149, 150] or dynamic models that depend on the applied electric field $\sigma(E)$ [151, 152], tissue temperature $\sigma(T)$ [153], or a combination of

both $\sigma(E, T)$ [154, 71, 58]. Dynamic behavior is commonly implemented in electrical conductivity modeling, as it better correlates numerical model outcomes with experimental data, reducing errors in the electroporated area from 30% to 3% [87]. Furthermore, incorporating dynamic changes helps decrease variability in determining the electric field threshold for IRE, as demonstrated in canine kidneys [18] and prostate cancer [148] studies. Since IRE is theoretically considered as a non-thermal ablation technique, we decided to model the tissue electrical conductivity as a function of an electric field, as demonstrated in Chapters 1 and 2. However, some studies reported temperature increases during IRE treatment [155, 156, 10], so incorporating temperature effects on electrical conductivity may lead to a more accurate model.

Model validation is essential for ensuring that simulation results accurately represent actual ablation outcomes under similar protocols. In this thesis, chapter 2 validates the numerical model on ex vivo animal tissue by monitoring temperature changes during treatment. Animal tissue is often used in studies due to its heterogeneous nature and similar electrical characteristics to human tissue during electroporation [55, 157]. However, performing a broad range of parametric analyses on animal tissue is challenging due to the need for rapid tissue preparation and ablation before organ cells die and the ablation area becomes difficult to observe [158]. Potatoes are another common choice for validation, as their rapid changes in electrical conductivity are similar to animal tissue [87]. They allow for a larger number of experiments on living cells and a wider range of parameters to be tested [159]. Electroporated areas in potatoes are easily visualized as dark areas representing cell membrane rupture, simplifying the evaluation of IRE protocols, as seen in Chapter 3. However, the main limitation is that potatoes' electrical properties differ significantly from human tissue, and their lower IRE threshold means that results from potatoes cannot be used for clinical treatment planning.

Accurate electrode placement is crucial for obtaining electric field distributions that align with simulation calculations. In our experiments using either potato or animal tissue, accurate electrode placement is challenging due to the flimsiness and instability of commonly used 19G IRE electrodes during insertion [160, 161]. Even with specialized tools like needle holders or spacer devices, major differences were still observed after insertion due to needle

bending or tissue deformation. To address these issues, recent studies have turned to model validation based on retrospective studies. These studies focus on determining electric field thresholds for specific tissues based on IRE ablation results [162] or evaluating the effect of electrode configuration on treatment success [77]. This method validates the model results on human tissue models and can be extended to other settings for treatment planning, provided the tissue types are similar. Regarding accurate electrode placement, some studies propose the use of bipolar probes [24, 16] to reduce the number of probes and simplify treatment processes, thereby saving time and increasing accuracy.

Computational models enable researchers and clinicians to gain a deeper understanding of the complex biological processes that occur during IRE. These models allow for a detailed examination of tissue responses to various IRE parameters through simulation. To reduce computational costs while designing these models, simplified shapes like spheres, ellipsoids, and cylinders are commonly used as organ representations, even though sacrificing accuracy [18, 163]. In clinical practice, this approach is also found in designing pre-operative models for treatment planning, where tumor shapes are often approximated as ellipsoids. As a result, the ablated area sometimes turns out smaller than the predicted area, despite adherence to the treatment protocol and manufacturer-recommended parameters [164]. Therefore, adding a safety margin for ablation, as commonly seen in other thermal ablation techniques, is essential. Safety margins help ensure the removal of tumor sprouting surrounding the tumor, preventing tumor recurrence [27] and reducing uncertainties during treatment, such as changes in tissue electrical properties or IRE electroporation thresholds [163]. Although there is no consensus on the optimal safety margin for IRE ablation [165], it typically ranges from 5-10 mm.

To improve model accuracy, actual organ shapes can be incorporated into the computational model, enabling precise electrode positioning. However, using real-shape models may lead to higher computational costs and longer planning times. In addition, segmenting tumor tissue is time-consuming and prone to inter-observer variability. One solution is to use deep learning for automatic tumor segmentation, as proposed in Chapter 4. This approach can improve computational model accuracy and ensure complete tumor ablation.

Deep learning approaches have become popular due to their simplicity, fast processing, and high accuracy. However, their performance relies heavily on large labeled datasets, with larger training sets generally yielding improved results. Obtaining sufficient labeled data remains challenging. Data augmentation can help generate new labeled data for training, but not all techniques are suitable or helpful for medical applications [166]. Some methods that can assist in training networks with limited datasets include semi-supervised learning [167], transfer learning [168], and synthetic data generation [169]. Additionally, as MRI gains popularity as imaging guidance for tumor treatment, there is a need to develop networks that can segment MR images.

A significant challenge in working with MR images is the variability in image intensity for structures at the same location due to differing MR sequences. For example, various networks for liver segmentation have been developed, such as diffusion-weighted [170], T1-weighted [171], and T2-weighted [172]. Most existing networks have been trained using CT images, which means a potential solution for MR data is to implement an image-to-image translation method that is able to translate images from MR to CT, as demonstrated in previous studies [173, 174].

Moreover, during treatment planning for electrode positioning, information from nearby vital structures is required, including major bile ducts, blood vessels, and nerves. To develop accurate treatment planning based on patient-specific models [175], further investigation into developing a general network that can segment these structures is necessary.

7.2 Robotic device

7.2.1 Summary of the key result

Chapter 5 discusses the design and evaluation of an MRI-safe, patient-mounted robot for assisting multiple needle insertion in IRE treatment. The robot has four degrees of freedom actuated by pneumatic motors, which can be used to position and orient the electrode toward the target tumor. Multiple electrodes are inserted sequentially, with parallelism

between the electrodes maintained by considering the orientation of previous electrodes. The robot's accuracy in free air was 0.72 ± 0.26 mm on the horizontal axis and 1.60 ± 0.75 mm on the vertical axis. Further evaluation assessed the robot's compatibility with an MRI scanner, resulting in no artifact and no change in the signal-to-noise ratio of the image scans.

Chapter 6 presents an updated design of the robot from the previous chapter. This study employs a grid system to maintain distance and parallelism between electrodes. The robot is designed with two degrees of freedom, focusing on adjusting grid angulation and accommodating lesion targeting in various positions. The reduced number of actuators simplifies robot control and installation by requiring fewer pneumatic tubes. The robot's accuracy and ability to maintain electrode parallelism were tested in evaluations. The robot's accuracy depends on the relative position of the target to the nearest grid hole, as well as the depth of the target point and the insertion angle. As for parallelism, the robot demonstrated a maximum deviation of less than 1° , making it suitable for IRE procedures that require limited deviation when placing multiple needles.

7.2.2 Limitations and future challenges

With the advantages that IRE offers compared to other thermal ablation methods, it remains a less preferable option for tumor treatment due to its technical complexity. Multiple electrodes need to be inserted during treatment, depending on the tumor size. Electrode placement accuracy plays a crucial role in ensuring complete coverage of the ablation area. Using a robot during electrode placement improves accuracy and reduces procedure time.

One factor affecting the accuracy of our proposed robot is the quality of its components. Currently, robot components are fabricated using 3D printing, making production faster and more suitable for prototyping when designs are prone to change. However, the final product should be produced using a better process that offers higher resolution. For example, the limitations of the current printer affect the dimensions of the electrode hole from the robot grid,

significantly impacting the robot's accuracy. We believe that with more accurate machines and better material quality, the robot components will be more precise, and robot performance will be improved.

Another improvement for the robot is the implementation of sensor feedback to accurately inform the current state of the robot's position. Currently, the robot uses the information of relative step position to indicate its position. However, this is prone to error, especially considering the long distance between the control room and the MRI room which introduces a decrease in the pressure and eventually produces slips to the motor movement. Although various position sensors are available, the requirement for MRI-compatible sensors limits the types that can be used. The use of MR-safe sensors as position [176] or force sensor [177] can be explored to provide feedback and status during robot movement.

Robot accuracy may also be affected by tissue or organ deformation during the insertion process, causing the actual electrode path to deviate from the planned path. Additionally, patient movement may introduce errors caused by organ motion, especially during respiration or muscle contractions during electroporation. The current solution for addressing errors from tissue deformation is by carefully comparing planning images with images taken after needle insertion. If deviations occur, the electrode will be adjusted, and the comparison process repeated. We suggest using MRI to simplify this process, as it allows for real-time monitoring of electrode insertion while keeping both patients and clinicians safe from radiation. Moreover, tissue deformation can be modeled and integrated into the planning process [178, 179], so the final plan can be adapted, and placement can be more accurate. As for patient motion, current practice involves placing patients under total anesthesia and securing them well during electrode insertion. Another approach is using mechanical ventilation with total muscle relaxation to minimize respiratory movement or spontaneous patient movement. Implementing a patient-mounted robot in the robot design can be an alternative to compensate for patient-induced movement. Specific patient respiration models can be created to help determine the safest moment to begin electrode insertion.

In terms of robot design, each design presented in this thesis has unique advantages. The first robot design allows for controllable electrode orientation and position, as long as the target is within the robot's workspace. Equipped with a needle holder, this robot is best suited for treatments requiring only two electrodes. However, when more electrodes are needed, insertion may take longer and be less accurate due to individual electrode adjustments. The second robot design incorporates a grid system for electrode insertion, enabling multiple electrodes to be inserted while maintaining parallelism and distance between them. However, errors may occur if the needle position is not located in a grid hole, leading to over or underestimation of ablation. For future designs, it is crucial to consider treatment patterns, particularly when more than two electrodes are required. The current model utilizes replaceable grids, making it a flexible option for adapting to different treatment patterns or grid sizes that match electrode diameters. Consequently, the robot can be used not only for specific needle sizes and treatments but also for other applications, enhancing the robot's versatility.

Future robot designs should address the registration and mounting mechanisms to enhance efficiency and safety. In the current design, markers for registration are manually placed on the robot body. Integrating marker positions and shapes into the robot's main design would enable the development of an algorithm to automatically recognize these markers, speeding up the registration process. Regarding robot mounting, the current strap belt approach could be improved. By incorporating a softer material for the bottom part of the robot, it can better adapt to the patient's body contours. Additionally, using a suction mechanism to fix the robot in place could provide a more stable and secure attachment [180], minimizing movement during the procedure and maintaining registration and accuracy.

Lastly, an emergency stop mechanism must be integrated into the robot navigation system to allow for immediate intervention in case of changes in plans or unexpected failures. This mechanism could entail an immediate halt to robot movement or a return to the starting/home position. This critical function is essential to safeguard both the user and the patient from potential harm.

7.3 Future recommendation toward clinical practice

Before introducing the robot into clinical practice, several tests must be conducted, including *ex vivo*, *in vivo*, and patient trials. A clinical workflow should be designed, encompassing the installation, utilization, and cleaning of the robot components. Installation in the MRI room requires special consideration, particularly regarding the robot's pneumatic power source. Some hospitals may have pressurized gas available in the room, while others might need an external pump, taking into account the output required for the robot's operation. Additionally, the length of the pneumatic tube connecting the MRI room to the control room should be considered, as pressure drops may occur. For cleaning, some components can be sterilized, while others may be designated as disposable items.

Although most studies recommend parallel needle placement during treatment to ensure homogeneous electric field distribution and prevent thermal damage, non-parallel placement might be more suitable for certain situations, such as irregular tumor shapes or tumors near vital organs. Developing a computation model that considers non-parallel placement, realistic tumor shapes, and multiple needle placement would provide clinicians with a more versatile tool for effective tumor treatment while minimizing damage to healthy tissue.

Lastly, the robot control system should offer a user-friendly interface, enabling users with less experience to operate it effectively. Treatment planning should also be integrated with the software used for robot navigation. The treatment planning software should include features such as organ segmentation during planning, simulation of ablation area prediction based on IRE parameters, and determination of optimal needle placement considering tumor shape, nearby organs, and robot limitations. By integrating this system with the robot, electrodes can be guided along the planned path, and placement accuracy can be monitored using the same software.

7.4 Conclusion

In this thesis, we presented and validated 2D and 3D computational models to investigate the optimal IRE protocol. The optimization process focuses on examining the effects of pulse parameters and electrode configurations on the ablation area and thermal damage to the target tissue. To improve the model's accuracy, we suggested incorporating the actual tissue shape into the tissue models in the simulation. Therefore, we proposed an automatic segmentation method using deep learning for segmenting liver and tumors from CT images. This tool can assist clinicians in developing more patient-specific models, thereby improving treatment planning outcomes.

IRE has various advantages over other ablation methods. However, the complexity of positioning multiple electrodes during IRE treatment makes it a less popular choice for most tumor treatments. Maintaining parallel insertion between electrodes is essential for achieving complete ablation and preventing thermal damage to surrounding tissue. We developed robotic systems to assist clinicians in placing multiple electrodes into the target tissue. The robots were fabricated using plastic material and actuated with a pneumatic system, allowing them to be used within an MRI scanner. This enables visualization of the tumor location, monitoring of electrode placement, and safer treatment for both patients and clinicians from radiation. The two designs of the robotic system have distinct mechanisms for guiding the parallel insertion of multiple electrodes. The results demonstrated that both robots had limited deviation, but remained within the acceptable range for IRE procedures.

We hope that the tools proposed in this thesis, including computational models and robotic systems, will contribute to the improvement of treatment efficacy using irreversible electroporation.

Bibliography

- [1] Jon F Edd and Rafael V Davalos. “Mathematical modeling of irreversible electroporation for treatment planning”. In: *Technology in cancer research & treatment* 6.4 (2007), pp. 275–286.
- [2] Mark J Jaroszeski, Richard Gilbert, and Richard Heller. “Electrochemotherapy: an emerging drug delivery method for the treatment of cancer”. In: *Advanced drug delivery reviews* 26.2-3 (1997), pp. 185–197.
- [3] Richard Heller, Richard Gilbert, and Mark J Jaroszeski. “Clinical applications of electrochemotherapy”. In: *Advanced drug delivery reviews* 35.1 (1999), pp. 119–129.
- [4] George W Bates, James A Saunders, and Arthur E Sowers. “Electrofusion: principles and applications”. In: *Cell fusion* (1987), pp. 367–395.
- [5] F Andre and LM Mir. “DNA electrotransfer: its principles and an updated review of its therapeutic applications”. In: *Gene therapy* 11.1 (2004), S33–S42.
- [6] Samo Mahnič-Kalamiza, Eugene Vorobiev, and Damijan Miklavčič. “Electroporation in food processing and biorefinery”. In: *The Journal of membrane biology* 247 (2014), pp. 1279–1304.
- [7] Nikolai Lebovka and Eugene Vorobiev. “Food and biomaterials processing assisted by electroporation”. In: *Advanced electroporation techniques in biology and medicine*. CRC Press, 2010, pp. 483–510.
- [8] Rafael V Davalos, LM Mir, and B Rubinsky. “Tissue ablation with irreversible electroporation”. In: *Annals of biomedical engineering* 33 (2005), pp. 223–231.
- [9] David Stillström et al. “Initial experience with irreversible electroporation of liver tumours”. In: *European journal of radiology open* 6 (2019), pp. 62–67.

- [10] Willemien Van Den Bos et al. “Thermal energy during irreversible electroporation and the influence of different ablation parameters”. In: *Journal of Vascular and Interventional Radiology* 27.3 (2016), pp. 433–443.
- [11] Kenneth R Diller. “Modeling of bioheat transfer processes at high and low temperatures”. In: *Advances in heat transfer*. Vol. 22. Elsevier, 1992, pp. 157–357.
- [12] Muneeb Ahmed et al. “Principles of and advances in percutaneous ablation”. In: *Radiology* 258.2 (2011), pp. 351–369.
- [13] Katrina F Chu and Damian E Dupuy. “Thermal ablation of tumours: biological mechanisms and advances in therapy”. In: *Nature Reviews Cancer* 14.3 (2014), pp. 199–208.
- [14] Martin L Yarmush et al. “Electroporation-based technologies for medicine: principles, applications, and challenges”. In: *Annual review of biomedical engineering* 16 (2014), pp. 295–320.
- [15] Paulo A Garcia et al. “A parametric study delineating irreversible electroporation from thermal damage based on a minimally invasive intracranial procedure”. In: *Biomedical engineering online* 10 (2011), pp. 1–22.
- [16] Ayelet Wandel et al. “Optimizing irreversible electroporation ablation with a bipolar electrode”. In: *Journal of Vascular and Interventional Radiology* 27.9 (2016), pp. 1441–1450.
- [17] Yaniv Zager et al. “Optimization of irreversible electroporation protocols for in-vivo myocardial decellularization”. In: *PLoS One* 11.11 (2016), e0165475.
- [18] Robert E Neal et al. “In vivo characterization and numerical simulation of prostate properties for non-thermal irreversible electroporation ablation”. In: *The Prostate* 74.5 (2014), pp. 458–468.
- [19] Angelika Vižintin et al. “Effect of interphase and interpulse delay in high-frequency irreversible electroporation pulses on cell survival, membrane permeabilization and electrode material release”. In: *Bio-electrochemistry* 134 (2020), p. 107523.

-
- [20] Kenneth N Aycok et al. “A theoretical argument for extended inter-pulse delays in therapeutic high-frequency irreversible electroporation treatments”. In: *IEEE Transactions on Biomedical Engineering* 68.6 (2021), pp. 1999–2010.
- [21] Oyinlolu Adeyanju, Haitham Al-Angari, and Alan Sahakian. “The optimization of needle electrode number and placement for irreversible electroporation of hepatocellular carcinoma”. In: *Radiology and oncology* 46.2 (2012), pp. 126–135.
- [22] Alessia Ongaro et al. “Effect of electrode distance in grid electrode: Numerical models and in vitro tests”. In: *Technology in Cancer Research & Treatment* 17 (2018), p. 1533033818764498.
- [23] Helena Cindrič et al. “Optimization of Transpedicular Electrode Insertion for Electroporation-Based Treatments of Vertebral Tumors”. In: *Cancers* 14.21 (2022), p. 5412.
- [24] Robert E Neal et al. “Treatment of breast cancer through the application of irreversible electroporation using a novel minimally invasive single needle electrode”. In: *Breast cancer research and treatment* 123 (2010), pp. 295–301.
- [25] Vitalij Novickij et al. “Does the shape of the electric pulse matter in electroporation?” In: *Frontiers in oncology* 12 (2022), pp. 1–12.
- [26] Alette H Ruarus et al. “Irreversible electroporation for hepatic tumors: protocol standardization using the modified Delphi technique”. In: *Journal of Vascular and Interventional Radiology* 31.11 (2020), pp. 1765–1771.
- [27] Bor Kos et al. “Careful treatment planning enables safe ablation of liver tumors adjacent to major blood vessels by percutaneous irreversible electroporation (IRE)”. In: *Radiology and oncology* 49.3 (2015), pp. 234–241.
- [28] Matthew Bower et al. “Irreversible electroporation of the pancreas: definitive local therapy without systemic effects”. In: *Journal of surgical oncology* 104.1 (2011), pp. 22–28.

- [29] J-P Tasu et al. “Irreversible electroporation for locally advanced pancreatic cancer”. In: *Diagnostic and interventional Imaging* 97.12 (2016), pp. 1297–1304.
- [30] Chunlan Jiang, Rafael V Davalos, and John C Bischof. “A review of basic to clinical studies of irreversible electroporation therapy”. In: *IEEE Transactions on biomedical Engineering* 62.1 (2014), pp. 4–20.
- [31] Robert E Neal et al. “Simulation of in vivo irreversible electroporation renal ablations”. In: *6th European Conference of the International Federation for Medical and Biological Engineering: MBEC 2014, 7-11 September 2014, Dubrovnik, Croatia*. Springer. 2015, pp. 813–816.
- [32] Zheng Fang et al. “Irreversible electroporation enhanced by radiofrequency ablation: an in vitro and computational study in a 3D liver tumor model”. In: *Annals of Biomedical Engineering* 49.9 (2021), pp. 2126–2138.
- [33] Eduardo L Latouche, Rafael V Davalos, and Robert CG Martin. “Modeling of irreversible electroporation treatments for the optimization of pancreatic cancer therapies”. In: *6th European Conference of the International Federation for Medical and Biological Engineering: MBEC 2014, 7-11 September 2014, Dubrovnik, Croatia*. Springer. 2015, pp. 801–804.
- [34] Paulo A Garcia et al. “Nonthermal irreversible electroporation as a focal ablation treatment for brain cancer”. In: *Tumors of the Central Nervous System, Volume 12: Molecular Mechanisms, Children’s Cancer, Treatments, and Radiosurgery* (2014), pp. 171–182.
- [35] Timur Kuzhagaliyev et al. “Augmented reality needle ablation guidance tool for irreversible electroporation in the pancreas”. In: *Medical imaging 2018: Image-guided procedures, robotic interventions, and modeling*. Vol. 10576. SPIE. 2018, pp. 260–265.
- [36] Lukas P Beyer et al. “Evaluation of a robotic system for irreversible electroporation (IRE) of malignant liver tumors: initial results”. In: *International journal of computer assisted radiology and surgery* 12 (2017), pp. 803–809.

-
- [37] Xiao F He et al. “Preliminary clinical application of the robot-assisted CT-guided irreversible electroporation ablation for the treatment of pancreatic head carcinoma”. In: *The International Journal of Medical Robotics and Computer Assisted Surgery* 16.4 (2020), e2099.
- [38] Kenneth R Thomson, Helen Kavnoudias, and Robert E Neal II. “Introduction to irreversible electroporation—principles and techniques”. In: *Techniques in vascular and interventional radiology* 18.3 (2015), pp. 128–134.
- [39] Arman Smakic et al. “Performance of a robotic assistance device in computed tomography-guided percutaneous diagnostic and therapeutic procedures”. In: *Cardiovascular and interventional radiology* 41 (2018), pp. 639–644.
- [40] Alexandar Blazeovski et al. “Salvage robot-assisted radical prostatectomy following focal ablation with irreversible electroporation: feasibility, oncological and functional outcomes”. In: *BMC urology* 22.1 (2022), pp. 1–8.
- [41] Iwan Paolucci et al. “Stereotactic image-guidance for ablation of malignant liver tumors”. In: *Liver Pathology*. IntechOpen, 2019.
- [42] Andreas Melzer et al. “Innomotion for percutaneous image-guided interventions”. In: *IEEE Engineering in Medicine and Biology Magazine* 27.3 (2008), pp. 66–73.
- [43] Zhuoliang He et al. “Design of a percutaneous MRI-guided needle robot with soft fluid-driven actuator”. In: *IEEE Robotics and Automation Letters* 5.2 (2020), pp. 2100–2107.
- [44] Dan Stoianovici et al. “Multi-imager compatible, MR safe, remote center of motion needle-guide robot”. In: *IEEE Transactions on Biomedical Engineering* 65.1 (2017), pp. 165–177.
- [45] Nobuhiko Hata et al. “Needle guiding robot for MR-guided microwave thermotherapy of liver tumor using motorized remote-center-of-motion constraint”. In: *Proceedings of the 2005 IEEE International Conference on Robotics and Automation*. IEEE, 2005, pp. 1652–1656.

- [46] Patrick Bilic et al. “The liver tumor segmentation benchmark (lits)”. In: *Medical Image Analysis* 84 (2023), p. 102680.
- [47] Girindra Wardhana et al. “Development of a thermal model for irreversible electroporation: an approach to estimate and optimize the IRE protocols”. In: *International journal of computer assisted radiology and surgery* 16.8 (2021), pp. 1325–1334.
- [48] Sonia Orcutt, Bela Kis, and Mokenge Malafa. “Case report: irreversible electroporation for locally advanced pancreatic cancer”. In: *International journal of surgery case reports* 40 (2017), pp. 54–57.
- [49] Salvatore Paiella et al. “Safety and feasibility of Irreversible Electroporation (IRE) in patients with locally advanced pancreatic cancer: results of a prospective study”. In: *Digestive surgery* 32.2 (2015), pp. 90–97.
- [50] David P Ryan, Theodore S Hong, and Nabeel Bardeesy. “Pancreatic adenocarcinoma”. In: *New England Journal of Medicine* 371.11 (2014), pp. 1039–1049.
- [51] Robert H Hawes et al. “A multispecialty approach to the diagnosis and management of pancreatic cancer”. In: *The American journal of gastroenterology* 95.1 (2000), pp. 17–31.
- [52] Karin Nielsen et al. “Irreversible electroporation of liver tumors”. In: *Irreversible Electroporation in Clinical Practice* (2018), pp. 139–166.
- [53] Katsunori Imai et al. “Liver metastases from pancreatic ductal adenocarcinoma: is there a place for surgery in the modern era?” In: *Journal of Pancreatology* 3.02 (2020), pp. 81–85.
- [54] Tadej Kotnik et al. “Cell membrane electroporation-Part 1: The phenomenon”. In: *IEEE Electrical Insulation Magazine* 28.5 (2012), pp. 14–23.
- [55] EM Dunki-Jacobs, P Philips, and RCG Martin Ii. “Evaluation of thermal injury to liver, pancreas and kidney during irreversible electroporation in an in vivo experimental model”. In: *Journal of British Surgery* 101.9 (2014), pp. 1113–1121.

-
- [56] Martin JC van Gemert et al. “Irreversible electroporation: just another form of thermal therapy?” In: *The Prostate* 75.3 (2015), pp. 332–335.
 - [57] Paulo A Garcia, Rafael V Davalos, and Damijan Miklavcic. “A numerical investigation of the electric and thermal cell kill distributions in electroporation-based therapies in tissue”. In: *PloS one* 9.8 (2014), e103083.
 - [58] Timothy J O’Brien et al. “Effects of internal electrode cooling on irreversible electroporation using a perfused organ model”. In: *International Journal of Hyperthermia* 35.1 (2018), pp. 44–55.
 - [59] Yingtian Wei, Yueyong Xiao, and Zhongmin Wang. “The interventional therapeutics of irreversible electroporation for pancreatic cancer”. In: *Integrative Pancreatic Intervention Therapy*. Elsevier, 2021, pp. 355–362.
 - [60] Rafael V Davalos and Boris Rubinsky. “Temperature considerations during irreversible electroporation”. In: *International journal of heat and mass transfer* 51.23-24 (2008), pp. 5617–5622.
 - [61] Yongji Yang et al. “Optimization of electrode configuration and pulse strength in irreversible electroporation for large ablation volumes without thermal damage”. In: *Journal of Engineering and Science in Medical Diagnostics and Therapy* 1.2 (2018).
 - [62] Chunlan Jiang, Qi Shao, and John Bischof. “Pulse timing during irreversible electroporation achieves enhanced destruction in a hindlimb model of cancer”. In: *Annals of biomedical engineering* 43 (2015), pp. 887–895.
 - [63] Xiaoming He and John C Bischof. “Quantification of temperature and injury response in thermal therapy and cryosurgery”. In: *Critical Reviews™ in Biomedical Engineering* 31.5&6 (2003).
 - [64] Zhen Ji and Christopher L Brace. “Expanded modeling of temperature-dependent dielectric properties for microwave thermal ablation”. In: *Physics in Medicine & Biology* 56.16 (2011), p. 5249.
 - [65] Francis A Duck. *Physical properties of tissues: a comprehensive reference book*. Academic press, 2013.

- [66] Anandaroop Bhattacharya and RL Mahajan. “Temperature dependence of thermal conductivity of biological tissues”. In: *Physiological measurement* 24.3 (2003), p. 769.
- [67] Janez Langus et al. “Dynamic finite-element model for efficient modelling of electric currents in electroporated tissue”. In: *Scientific reports* 6.1 (2016), p. 26409.
- [68] Paul D Berger et al. “Introduction to Taguchi methods”. In: *Experimental Design: With Application in Management, Engineering, and the Sciences*. (2018), pp. 449–480.
- [69] Pierre Agnass et al. “Mathematical modeling of the thermal effects of irreversible electroporation for in vitro, in vivo, and clinical use: a systematic review”. In: *International journal of hyperthermia* 37.1 (2020), pp. 486–505.
- [70] Martijn R Meijerink, Hester J Scheffer, and Govindarajan Narayanan. *Irreversible electroporation in clinical practice*. Springer, 2018.
- [71] Timothy J O’Brien et al. “Cycled pulsing to mitigate thermal damage for multi-electrode irreversible electroporation therapy”. In: *International Journal of Hyperthermia* 36.1 (2019), pp. 952–962.
- [72] M Lee Lucas et al. “In vivo electroporation using an exponentially enhanced pulse: a new waveform”. In: *DNA and Cell Biology* 20.3 (2001), pp. 183–188.
- [73] Lujia Ding et al. “Treatment planning optimization in irreversible electroporation for complete ablation of variously sized cervical tumors: a numerical study”. In: *Journal of Biomechanical Engineering* 143.1 (2021).
- [74] Girindra Wardhana et al. “Investigating the effect of electrode orientation on irreversible electroporation with experiment and simulation”. In: *International journal of computer assisted radiology and surgery* 17.8 (2022), pp. 1399–1407.
- [75] Kenneth N Aycock and Rafael V Davalos. “Irreversible electroporation: background, theory, and review of recent developments in clinical oncology”. In: *Bioelectricity* 1.4 (2019), pp. 214–234.

-
- [76] Olivier Gallinato et al. “Numerical workflow of irreversible electroporation for deep-seated tumor”. In: *Physics in Medicine & Biology* 64.5 (2019), p. 055016.
- [77] René Michael Mathy et al. “Impact of needle positioning on ablation success of irreversible electroporation: A unicentric retrospective analysis”. In: *Scientific Reports* 10.1 (2020), pp. 1–10.
- [78] Luca G Campana et al. “Non-parallelism of needles in electroporation: 3D computational model and experimental analysis”. In: *COMPEL-The international journal for computation and mathematics in electrical and electronic engineering* 38.1 (2019), pp. 348–361.
- [79] Mohammad Hjouj and Boris Rubinsky. “Magnetic resonance imaging characteristics of nonthermal irreversible electroporation in vegetable tissue”. In: *The Journal of membrane biology* 236 (2010), pp. 137–146.
- [80] Christopher B Arena et al. “A three-dimensional in vitro tumor platform for modeling therapeutic irreversible electroporation”. In: *Biophysical journal* 103.9 (2012), pp. 2033–2042.
- [81] Cecilia Suárez et al. “The role of additional pulses in electroporation protocols”. In: *PloS one* 9.12 (2014), e113413.
- [82] Amir Khorasani. “A numerical study on the effect of conductivity change in cell kill distribution in irreversible electroporation”. In: *Polish Journal of Medical Physics and Engineering* 26.2 (2020), pp. 69–76.
- [83] S Zhu et al. “Evaluation of thermal properties of food materials at high pressures using a dual-needle line-heat-source method”. In: *Journal of food science* 72.2 (2007), E49–E56.
- [84] N Wang and JG Brennan. “Changes in structure, density and porosity of potato during dehydration”. In: *Journal of Food Engineering* 24.1 (1995), pp. 61–76.

- [85] RS Criddle et al. “Effects of temperature and oxygen depletion on metabolic rates of tomato and carrot cell cultures and cuttings measured by calorimetry”. In: *Plant, Cell & Environment* 11.8 (1988), pp. 695–701.
- [86] Alessia Bernardis et al. “Electric field computation and measurements in the electroporation of inhomogeneous samples”. In: *Open Physics* 15.1 (2017), pp. 790–796.
- [87] A Ivorra, LM Mir, and B Rubinsky. “Electric field redistribution due to conductivity changes during tissue electroporation: experiments with a simple vegetal model”. In: *World Congress on Medical Physics and Biomedical Engineering, September 7-12, 2009, Munich, Germany: Vol. 25/13 Special Topics and Workshops*. Springer. 2010, pp. 59–62.
- [88] Ileana Menegazzo et al. “Time Domain Nuclear Magnetic Resonance (TD-NMR) to evaluate the effect of potato cell membrane electroporation”. In: *Innovative Food Science & Emerging Technologies* 65 (2020), p. 102456.
- [89] Q Castellví, J Banús, and A Ivorra. “3D assessment of irreversible electroporation treatments in vegetal models”. In: *1st World Congress on Electroporation and Pulsed Electric Fields in Biology, Medicine and Food & Environmental Technologies: Portorož, Slovenia, September 6–10, 2015*. Springer. 2016, pp. 294–297.
- [90] Girindra Wardhana et al. “Toward reliable automatic liver and tumor segmentation using convolutional neural network based on 2.5D models”. In: *International Journal of Computer Assisted Radiology and Surgery* 16 (2021), pp. 41–51.
- [91] Global Burden of Disease Liver Cancer Collaboration. “The Burden of Primary Liver Cancer and Underlying Etiologies From 1990 to 2015 at the Global, Regional, and National Level: Results From the Global Burden of Disease Study 2015”. In: *JAMA Oncology* 3.12 (Dec. 2017), pp. 1683–1691. DOI: 10.1001/jamaoncol.2017.3055.

-
- [92] Xiaolei Huang and Gavriil Tsechpenakis. “Medical image segmentation”. In: *Information discovery on electronic health records*. Chapman and Hall/CRC, 2009, pp. 269–308.
- [93] Akshat Gotra et al. “Liver segmentation: indications, techniques and future directions”. In: *Insights into Imaging* 8.4 (Aug. 2017), pp. 377–392. DOI: 10.1007/s13244-017-0558-1.
- [94] Laura Fernández-de-Manuel et al. “3D liver segmentation in preoperative CT images using a levelsets active surface method”. In: *2009 annual international conference of the IEEE engineering in medicine and biology society*. IEEE, 2009, pp. 3625–3628.
- [95] Jana Lipková et al. “Automated unsupervised segmentation of liver lesions in ct scans via cahn-hilliard phase separation”. In: *arXiv preprint arXiv:1704.02348* (2017).
- [96] Laszlo Rusko et al. “Fully automatic liver segmentation for contrast-enhanced CT images”. In: *MICCAI Wshp. 3D Segmentation in the Clinic: A Grand Challenge* 2.7 (2007), pp. 412–417.
- [97] Ruchaneewan Susomboon, Daniela Stan Raicu, and Jacob Furst. “A hybrid approach for liver segmentation”. In: *Proceedings of MICCAI workshop on 3D segmentation in the clinic: a grand challenge*. Citeseer, 2007, pp. 151–160.
- [98] Daisuke Furukawa, Akinobu Shimizu, and Hidefumi Kobatake. “Automatic liver segmentation method based on maximum a posterior probability estimation and level set method”. In: *3D Segmentation in The Clinic: A Grand Challenge* 117 (2007).
- [99] Ying Chi et al. “A discussion on the evaluation of a new automatic liver volume segmentation method for specified CT image datasets”. In: *Proceedings of MICCAI workshop on 3D segmentation in the clinic: a grand challenge*. Citeseer, 2007, pp. 167–175.
- [100] Dagmar Kainmüller, Thomas Lange, and Hans Lamecker. “Shape constrained automatic segmentation of the liver based on a heuristic intensity model”. In: *Proc. MICCAI Workshop 3D Segmentation in the Clinic: A Grand Challenge*. Vol. 109. Citeseer, 2007, p. 116.

- [101] Dieter Seghers et al. “Landmark based liver segmentation using local shape and local intensity models”. In: *Proc. Workshop of the 10th Int. Conf. on MICCAI, Workshop on 3D Segmentation in the Clinic: A Grand Challenge*. 2007, pp. 135–142.
- [102] Tobias Heimann, Hans-Peter Meinzer, and Ivo Wolf. “A statistical deformable model for the segmentation of liver CT volumes”. In: *3D Segmentation in the clinic: A grand challenge* (2007), pp. 161–166.
- [103] Grzegorz Chlebus et al. “Automatic liver tumor segmentation in CT with fully convolutional neural networks and object-based postprocessing”. In: *Scientific reports* 8.1 (2018), p. 15497.
- [104] Lei Bi et al. “Automatic liver lesion detection using cascaded deep residual networks”. In: *arXiv preprint arXiv:1704.02703* (2017).
- [105] Xiaomeng Li et al. “H-DenseUNet: hybrid densely connected UNet for liver and tumor segmentation from CT volumes”. In: *IEEE transactions on medical imaging* 37.12 (2018), pp. 2663–2674.
- [106] Xiao Han. “Automatic liver lesion segmentation using a deep convolutional neural network method”. In: *arXiv preprint arXiv:1704.07239* (2017).
- [107] P Christ et al. “LiTS-liver tumor segmentation challenge”. In: *ISBI and MICCAI* (2017).
- [108] Patrick Bilic et al. “The Liver Tumor Segmentation Benchmark (LiTS)”. In: *Medical Image Analysis* 84 (2023), p. 102680. DOI: <https://doi.org/10.1016/j.media.2022.102680>.
- [109] Vijay Badrinarayanan, Alex Kendall, and Roberto Cipolla. “Segnet: A deep convolutional encoder-decoder architecture for image segmentation”. In: *IEEE transactions on pattern analysis and machine intelligence* 39.12 (2017), pp. 2481–2495.
- [110] Olaf Ronneberger, Philipp Fischer, and Thomas Brox. “U-Net: Convolutional Networks for Biomedical Image Segmentation”. In: *Medical Image Computing and Computer-Assisted Intervention – MICCAI 2015*. Ed. by Nassir Navab et al. Cham: Springer International Publishing, 2015, pp. 234–241.

-
- [111] Kaiming He et al. “Deep residual learning for image recognition”. In: *Proceedings of the IEEE conference on computer vision and pattern recognition*. 2016, pp. 770–778.
- [112] Victoria López et al. “An insight into classification with imbalanced data: Empirical results and current trends on using data intrinsic characteristics”. In: *Information sciences* 250 (2013), pp. 113–141.
- [113] Jun Fu et al. “Densely connected deconvolutional network for semantic segmentation”. In: *2017 IEEE international conference on image processing (ICIP)*. IEEE. 2017, pp. 3085–3089.
- [114] Stanislav Nikolov et al. “Deep learning to achieve clinically applicable segmentation of head and neck anatomy for radiotherapy”. In: *arXiv preprint arXiv:1809.04430* (2018).
- [115] Girindra Wardhana et al. “Design and Characterization of a Multiple Needle Insertion MRI-guided Robot for Irreversible Electroporation (IRE) Treatment”. In: *2022 9th IEEE RAS/EMBS International Conference for Biomedical Robotics and Biomechatronics (BioRob)*. 2022, pp. 1–6.
- [116] L.G.P.H. Vroomen et al. “Irreversible electroporation and thermal ablation of tumors in the liver, lung, kidney and bone: What are the differences?” In: *Diagnostic and Interventional Imaging* 98.9 (2017), pp. 609–617. DOI: <https://doi.org/10.1016/j.diii.2017.07.007>.
- [117] Yingtian Wei, Yueyong Xiao, and Zhongmin Wang. “Chapter 14 - The interventional therapeutics of irreversible electroporation for pancreatic cancer”. In: *Integrative Pancreatic Intervention Therapy*. Ed. by Maoquan Li et al. Elsevier, 2021, pp. 355–362. DOI: <https://doi.org/10.1016/B978-0-12-819402-7.00014-0>.
- [118] David SK Lu et al. “Effect of vessel size on creation of hepatic radiofrequency lesions in pigs: assessment of the “heat sink” effect”. In: *American Journal of Roentgenology* 178.1 (2002), pp. 47–51.

- [119] Edward W Lee et al. “Advanced hepatic ablation technique for creating complete cell death: irreversible electroporation”. In: *Radiology* 255.2 (2010), pp. 426–433.
- [120] Edward W Lee, Susan Thai, and Stephen T Kee. “Irreversible electroporation: a novel image-guided cancer therapy”. In: *Gut and liver* 4.Suppl 1 (2010), S99.
- [121] Russell C Langan et al. “Recurrence patterns following irreversible electroporation for hepatic malignancies”. In: *Journal of surgical oncology* 115.6 (2017), pp. 704–710.
- [122] Mikhail Silk et al. “The state of irreversible electroporation in interventional oncology”. In: *Seminars in interventional radiology*. Vol. 31. 02. Thieme Medical Publishers. 2014, pp. 111–117.
- [123] Govindarajan Narayanan. “Irreversible electroporation”. In: *Seminars in interventional radiology*. Vol. 32. 04. Thieme Medical Publishers. 2015, pp. 349–355.
- [124] Matej Kranjc et al. “Predicting irreversible electroporation-induced tissue damage by means of magnetic resonance electrical impedance tomography”. In: *Scientific reports* 7.1 (2017), pp. 1–10.
- [125] Niravkumar A Patel et al. “Body-mounted robot for image-guided percutaneous interventions: mechanical design and preliminary accuracy evaluation”. In: *2018 IEEE/RSJ International Conference on Intelligent Robots and Systems (IROS)*. IEEE. 2018, pp. 1443–1448.
- [126] Nikolai Hungr et al. “Design and validation of a CT-and MRI-guided robot for percutaneous needle procedures”. In: *IEEE transactions on robotics* 32.4 (2016), pp. 973–987.
- [127] Gang Li et al. “Fully actuated body-mounted robotic system for MRI-guided lower back pain injections: Initial phantom and cadaver studies”. In: *IEEE Robotics and Automation Letters* 5.4 (2020), pp. 5245–5251.

-
- [128] Faye Y Wu et al. “An MRI coil-mounted multi-probe robotic positioner for cryoablation”. In: *International Design Engineering Technical Conferences and Computers and Information in Engineering Conference*. Vol. 55935. American Society of Mechanical Engineers. 2013, V06AT07A012.
- [129] HS Kahn et al. “The population distribution of the sagittal abdominal diameter (SAD) and SAD/height ratio among Finnish adults”. In: *Clinical obesity* 4.6 (2014), pp. 333–341.
- [130] John Moir et al. “Systematic review of irreversible electroporation in the treatment of advanced pancreatic cancer”. In: *European Journal of Surgical Oncology (EJSO)* 40.12 (2014), pp. 1598–1604.
- [131] Martina Distelmaier et al. “Midterm Safety and Efficacy of Irreversible Electroporation of Malignant Liver Tumors Located Close to Major Portal or Hepatic Veins”. In: *Radiology* 285.3 (2017), pp. 1023–1031. DOI: 10.1148/radiol.2017161561.
- [132] Florentine EF Timmer et al. “Irreversible electroporation for locally advanced pancreatic cancer”. In: *Techniques in vascular and interventional radiology* 23.2 (2020), p. 100675.
- [133] Alexander DJ Baur et al. “MRI-TRUS fusion for electrode positioning during irreversible electroporation for treatment of prostate cancer”. In: *Diagnostic and Interventional Radiology* 23.4 (2017), p. 321.
- [134] Vincent Groenhuis and Stefano Stramigioli. “Rapid prototyping high-performance MR safe pneumatic stepper motors”. In: *IEEE/ASME transactions on mechatronics* 23.4 (2018), pp. 1843–1853.
- [135] Andriy Fedorov et al. “3D Slicer as an image computing platform for the Quantitative Imaging Network”. In: *Magnetic resonance imaging* 30.9 (2012), pp. 1323–1341.
- [136] Tamas Ungi, Andras Lasso, and Gabor Fichtinger. “Open-source platforms for navigated image-guided interventions”. In: *Medical Image Analysis* 33 (2016), pp. 181–186.

- [137] National Electrical Manufactures Association and others. “NEMA standards publication MS 1–2008 (R2014): Determination of Signal-to-Noise Ratio (SNR) in Diagnostic Magnetic Resonance Imaging”. In: *NEMA* (2014).
- [138] Kiyoyuki Chinzei, Karol Miller, et al. “Towards MRI guided surgical manipulator”. In: *Medical science monitor* 7.1 (2001), pp. 153–163.
- [139] Vincent Groenhuis, Françoise J Siepel, and Stefano Stramigioli. “Miniaturization of MR Safe Pneumatic Rotational Stepper Motors”. In: *2019 IEEE/RSJ International Conference on Intelligent Robots and Systems (IROS)*. IEEE. 2019, pp. 7150–7156.
- [140] Hanbal Arif et al. “Concept for parallel placement of flexible needles for Irreversible Electroporation”. In: *Current Directions in Biomedical Engineering* 7.2 (2021), pp. 219–222.
- [141] Sang-Eun Song et al. “Design evaluation of a double ring RCM mechanism for robotic needle guidance in MRI-guided liver interventions”. In: *2013 IEEE/RSJ International Conference on Intelligent Robots and Systems*. 2013, pp. 4078–4083. DOI: 10.1109/IROS.2013.6696940.
- [142] Niravkumar Patel et al. “Body-Mounted Robotic System for MRI-Guided Shoulder Arthrography: Cadaver and Clinical Workflow Studies”. In: *Frontiers in Robotics and AI* 8 (2021).
- [143] Pedro Moreira et al. “In vivo evaluation of angulated needle-guide template for MRI-guided transperineal prostate biopsy”. In: *Medical physics* 48.5 (2021), pp. 2553–2565.
- [144] Carl S McGill et al. “Precision grid and hand motion for accurate needle insertion in brachytherapy”. In: *Medical physics* 38.8 (2011), pp. 4749–4759.
- [145] Niki Abolhassani and RajniV Patel. “Deflection of a flexible needle during insertion into soft tissue”. In: *2006 International Conference of the IEEE Engineering in Medicine and Biology Society*. IEEE. 2006, pp. 3858–3861.

-
- [146] Paulo A Garcia, John H Rossmeisl, and Rafael V Davalos. “Electrical conductivity changes during irreversible electroporation treatment of brain cancer”. In: *2011 Annual International Conference of the IEEE Engineering in Medicine and Biology Society*. IEEE. 2011, pp. 739–742.
- [147] Natalie Beitel-White et al. “Electrical characterization of human biological tissue for irreversible electroporation treatments”. In: *2018 40th Annual International Conference of the IEEE Engineering in Medicine and Biology Society (EMBC)*. IEEE. 2018, pp. 4170–4173.
- [148] Sabrina Campelo et al. “An evaluation of irreversible electroporation thresholds in human prostate cancer and potential correlations to physiological measurements”. In: *APL bioengineering* 1.1 (2017), p. 016101.
- [149] Julie Gehl et al. “In vivo electroporation of skeletal muscle: threshold, efficacy and relation to electric field distribution”. In: *Biochimica et Biophysica Acta (BBA)-General Subjects* 1428.2-3 (1999), pp. 233–240.
- [150] Damijan Miklavčič et al. “A validated model of in vivo electric field distribution in tissues for electrochemotherapy and for DNA electrotransfer for gene therapy”. In: *Biochimica et Biophysica Acta (BBA)-General Subjects* 1523.1 (2000), pp. 73–83.
- [151] Davorka Sel et al. “Sequential finite element model of tissue electroporomeabilization”. In: *IEEE Transactions on Biomedical Engineering* 52.5 (2005), pp. 816–827.
- [152] Yongji Yang et al. “Development of a statistical model for cervical cancer cell death with irreversible electroporation in vitro”. In: *PLoS One* 13.4 (2018), e0195561.
- [153] G Long et al. “Histological and finite element analysis of cell death due to irreversible electroporation”. In: *Technology in cancer research & treatment* 13.6 (2014), pp. 561–569.

- [154] Paulo A Garcia et al. “Intracranial nonthermal irreversible electroporation: in vivo analysis”. In: *The Journal of membrane biology* 236 (2010), pp. 127–136.
- [155] Christopher C Fesmire et al. “Temperature dependence of high frequency irreversible electroporation evaluated in a 3D tumor model”. In: *Annals of Biomedical Engineering* 48 (2020), pp. 2233–2246.
- [156] Peter GK Wagstaff et al. “Irreversible electroporation of the porcine kidney: temperature development and distribution”. In: *Urologic Oncology: Seminars and Original Investigations*. Vol. 33. 4. Elsevier. 2015, 168–e1.
- [157] Bing Zhang et al. “An in vivo study of a custom-made high-frequency irreversible electroporation generator on different tissues for clinically relevant ablation zones”. In: *International Journal of Hyperthermia* 38.1 (2021), pp. 593–603.
- [158] Michael B Sano et al. “Production of spherical ablations using non-thermal irreversible electroporation: a laboratory investigation using a single electrode and grounding pad”. In: *Journal of Vascular and Interventional Radiology* 27.9 (2016), pp. 1432–1440.
- [159] Yanpeng Lv, Chenguo Yao, and Boris Rubinsky. “A conceivable mechanism responsible for the synergy of high and low voltage irreversible electroporation pulses”. In: *Annals of Biomedical Engineering* 47 (2019), pp. 1552–1563.
- [160] Eliel Ben-David et al. “Characterization of irreversible electroporation ablation in in vivo porcine liver”. In: *American Journal of Roentgenology* 198.1 (2012), W62–W68.
- [161] Natanel Jourabchi et al. “Irreversible electroporation (NanoKnife) in cancer treatment”. In: *Gastrointestinal Intervention* 3.1 (2014), pp. 8–18.
- [162] Helena Cindrič et al. “Retrospective study for validation and improvement of numerical treatment planning of irreversible electroporation ablation for treatment of liver tumors”. In:

-
- IEEE Transactions on Biomedical Engineering* 68.12 (2021), pp. 3513–3524.
- [163] Prashanth Lakshmi Narasimhan et al. “Global sensitivity study for irreversible electroporation: Towards treatment planning under uncertainty”. In: *Medical Physics* (2023).
- [164] Chad R Tracy, Wareef Kabbani, and Jeffrey A Cadeddu. “Irreversible electroporation (IRE): a novel method for renal tissue ablation”. In: *BJU international* 107.12 (2011), pp. 1982–1987.
- [165] JJ Wendler et al. “Why we should not routinely apply irreversible electroporation as an alternative curative treatment modality for localized prostate cancer at this stage”. In: *World journal of urology* 35 (2017), pp. 11–20.
- [166] Behnaz Abdollahi, Naofumi Tomita, and Saeed Hassanpour. “Data augmentation in training deep learning models for medical image analysis”. In: *Deep learners and deep learner descriptors for medical applications* (2020), pp. 167–180.
- [167] Weicheng Chi et al. “Deep learning-based medical image segmentation with limited labels”. In: *Physics in Medicine & Biology* 65.23 (2020), p. 235001.
- [168] Laith Alzubaidi et al. “Novel transfer learning approach for medical imaging with limited labeled data”. In: *Cancers* 13.7 (2021), p. 1590.
- [169] Maayan Frid-Adar et al. “Synthetic data augmentation using GAN for improved liver lesion classification”. In: *2018 IEEE 15th international symposium on biomedical imaging (ISBI 2018)*. IEEE. 2018, pp. 289–293.
- [170] Ioannis Lavdas et al. “Fully automatic, multiorgan segmentation in normal whole body magnetic resonance imaging (MRI), using classification forests (CF s), convolutional neural networks (CNN s), and a multi-atlas (MA) approach”. In: *Medical physics* 44.10 (2017), pp. 5210–5220.

- [171] Supriti Mulay et al. “Liver segmentation from multimodal images using HED-mask R-CNN”. In: *Multiscale Multimodal Medical Imaging: First International Workshop, MMMI 2019, Held in Conjunction with MICCAI 2019, Shenzhen, China, October 13, 2019, Proceedings 1*. Springer. 2020, pp. 68–75.
- [172] Kang Wang et al. “Automated CT and MRI liver segmentation and biometry using a generalized convolutional neural network”. In: *Radiology: Artificial Intelligence* 1.2 (2019), p. 180022.
- [173] Jelmer M Wolterink et al. “Deep MR to CT synthesis using unpaired data”. In: *Simulation and Synthesis in Medical Imaging: Second International Workshop, SASHIMI 2017, Held in Conjunction with MICCAI 2017, Québec City, QC, Canada, September 10, 2017, Proceedings 2*. Springer. 2017, pp. 14–23.
- [174] Xiao Han. “MR-based synthetic CT generation using a deep convolutional neural network method”. In: *Medical physics* 44.4 (2017), pp. 1408–1419.
- [175] Eduardo L Latouche et al. “Irreversible electroporation for the ablation of pancreatic malignancies: A patient-specific methodology”. In: *Journal of surgical oncology* 115.6 (2017), pp. 711–717.
- [176] Shaoping Huang et al. “An MR safe rotary encoder based on eccentric sheave and FBG Sensors”. In: *2021 IEEE International Conference on Robotics and Automation (ICRA)*. IEEE. 2021, pp. 9410–9416.
- [177] Hoseok Song, Kiyoun Kim, and Jungju Lee. “Development of optical fiber Bragg grating force-reflection sensor system of medical application for safe minimally invasive robotic surgery”. In: *Review of Scientific Instruments* 82.7 (2011), p. 074301.
- [178] Wanyu Liu et al. “Mechanics of tissue rupture during needle insertion in transverse isotropic soft tissue”. In: *Medical & Biological Engineering & Computing* 57 (2019), pp. 1353–1366.

-
- [179] Ranjit Barua et al. “Study and experimental investigation of insertion force modeling and tissue deformation phenomenon during surgical needle-soft tissue interaction”. In: *Proceedings of the Institution of Mechanical Engineers, Part C: Journal of Mechanical Engineering Science* 237.5 (2023), pp. 1007–1014.
- [180] Akira Bekku et al. “A body-mounted surgical assistance robot for minimally invasive spinal puncture surgery”. In: *5th IEEE RAS/EMBS International Conference on Biomedical Robotics and Biomechatronics*. IEEE. 2014, pp. 19–23.

Acknowledgments

Alhamdulillahi Rabbil Alamin

All praise is due to Allah, Lord of the universe.

In December 2018, I started my PhD program at the University of Twente. From the start, I knew it would be a challenging project due to my limited experience in the medical field. Fortunately, I met some people who provided me with the strength to persevere and the motivation to keep pushing forward. Their support and encouragement were crucial to my success. Without them, I would not have been able to achieve this significant milestone. I am deeply grateful to have had them with me on this journey, and I will always appreciate their kindness and generosity.

First of all, I would like to express my sincere gratitude to Prof. Dr. Jürgen Futterer for accepting me into this amazing PhD project. The opportunity to work at both the University of Twente and Radboud UMC has expanded my perspective on how engineering and the medical field can synergize to create a meaningful contribution to society. I deeply appreciate your invaluable constructive feedback and unwavering support throughout my research journey. Sometimes I felt like I could not handle the problems I had, but I am grateful that you were there to offer advice and encouragement. With your help, I was able to overcome the issues and successfully make significant progress.

In addition, I would like to express my sincere gratitude to my daily supervisor, Dr. Ir. Momen Abayazid. It was a pleasure to work and learn under your guidance, both inside and outside the university. I appreciate your advice and support, which has not only helped me to grow professionally but also personally and spiritually. I remember our discussion about my future plans on the top floor of the building during the IPCAI conference in Japan. It provided me with valuable insights into possibilities that I had never considered before, and I am deeply grateful for that.

I would like to express my appreciation to the members of the graduation committee, Prof. Dr. Ir. S. Stramigioli, Prof. Dr. Ir. H. van der Kooij, Prof. Dr. J. Dankelman, Prof. Dr. M.R. Meijerink, and Dr. J.M. Wolterink, for dedicating their time to review my manuscript. Their feedback was invaluable and greatly contributed to the improvement of the final version of my dissertation. I am honored to have had them on my committee.

As a member of the Robotics and Mechatronics Department, I feel fortunate to have the opportunity to interact with many wonderful and inspiring individuals. I am extremely grateful to Jolanda Boelema for her exceptional support and guidance throughout my PhD journey. She has been like a mother to me, always there to lend a hand whenever I had any problems. I would like to extend my appreciation to all the senior staff members for the enjoyable moments we have shared both in the office and during our social events. I would also like to express my gratitude to the technician teams. This book would not have been possible without the support from you. Specifically, I want to thank Sander, Artur, and Quentin for their superb assistance in fulfilling my 3D printing requests. Additionally, I would like to acknowledge Henny for his assistance from the project's beginning until its completion in constructing the experimental setup. Finally, I would like to express my appreciation to Marcel for his invaluable support with the software system. I am also thankful to my colleagues from the same office, Ammar, Ayham, Manuel, Yousef, Yaolei, Tim, Reinaldo, Hem, Anna, and Mostafa, for the good times we shared during lunch, dinner, and sports. I appreciate every moment that we have passed. Furthermore, I enjoyed the time spent with other colleagues, such as Vincent, who kindly shared his work on pneumatic motors, Toon, Chiara, Ramy, Federico, Sihao, Gerjan, Yi, Alexander, Fleur, Luuk, Elfi, Heime, Dimitris, Riccardo, Christophe, Yannik, Nils, and many others whom I cannot mention one by one.

A special appreciation goes out to Yoeko, who served as my first paranymp. We have spent time together since our first meeting during my master's thesis, and I am grateful for him being a great friend. I would also like to express my gratitude to Youssef, my second paranymp, for being a thoughtful friend and sharing many great times together. I wish them both all the best in their lives and careers.

Enschede is a small city in the eastern Netherlands, but it already feels like our second home, thanks to the Indonesian and Islamic communities. I would like to express my gratitude to the following individuals and families: Mas Okky, Mas Aulia, Mas Imam, Mas Wibi, Dadi, Darius, Ihrom, DBL family (Ambu, Mas Zul, Teh Cui, Kak Niswa, Kak Manda, Kak Vania, Mas Dimas, Eva, and Pak Ridwan), Mbak Dewi, Mbak Eli, Mbak Pipit, Wildan and family, Nazahra and family, Bang Nasrul and family, Bang Wan and family, Mas Adit and family, Mas Aji and family, Mas Aufar and family, Pak Dwi and family, Mas Edo and family, Mas Ega and family, Mas Fajar and family, Mas Ilman and family, Mas Iqbal and family, Mas Isom and family, Mas Khafid and family, Mas Nova and family, Mas Pesi and family, Mas Yan and family, Mas Yasir and family, and the extended families of IMEA and PPIE.

Additionally, I would like to express my gratitude to my fellow Muslim brothers and sisters in the UT Muslims community. Specifically, I would like to thank Anas, Muhammad Saleem, Tafheem, Ege, Boutaina, Sabrina, and the rest of the UT Muslims family. As a minority in a foreign country, practicing Islam can be challenging. But, the community has made it easier by organizing Islamic activities and providing extensive support, which allows me to practice my faith with ease. *Jazakumullah khairan.*

Furthermore, I would like to thank Minzi, Ramesh, Timo, Jeroen, Niek, Wesley, Wujun, Ren, Rose, Wouter, Rizki, Ani, Carlos, Mas Charles, Ivan, and many other players for playing badminton with me. Your friendship and support have made my time in Enschede so much more enjoyable. Through our games and conversations, I've learned so much about multiple cultures, multiple languages, and various ways of thinking, which helped me to adapt quickly to Enschede. So, thank you for everything and I look forward to playing many more games of badminton with you in the future.

I am very grateful to my wife, Nuzul Hesty Pranita, and my daughter, Giazura Aisyah Wardhana, for accompanying me on this journey. Nearly half of my PhD was completed during the COVID-19 pandemic, which was a challenging time, especially for my work. However, with your support, I am thankful that we were able to overcome this together. I am looking forward to our next journey with additional members joining our small family.

I would like to express my sincere gratitude to my dear parents, Mahmuza and Gustina Dewi, who brought me into this world and have always supported me in my studies. They have been a constant source of motivation, inspiring me to never give up no matter how difficult the challenges may be and to always strive towards my goals.

I would also like to thank my little sister, Dwiza Andari, and my little brother, Maulana Ginanjar Insani, for taking care of our parents while I am away from home. Additionally, I extend my thanks to my father-in-law and mother-in-law for giving their blessings and allowing Hesty and me to pursue our dreams.

The book marks the end of my journey as a PhD researcher, but it certainly does not mean the end of my journey as a researcher. I intend to continue my studies and use the knowledge I gain to create a more meaningful impact on society.

Girindra Wardhana
Enschede
1 June 2023

About the author



Girindra Wardhana was born on November 27, 1992, in Praya, Indonesia. In March 2014, he received his Bachelor of Engineering degree from Telkom University, Indonesia. His thesis was on the "Design and Construction of Total Dissolve Solution Measurement System using ATmega32 Microcontroller," which was supervised by Dr. M. Rokhmat and Dr. E. Wibowo. After graduation, he worked for several private companies on electrical and home automation projects.

In 2015, he received a scholarship from the Indonesian government through Indonesia Endowment Fund for Education (LPDP) to pursue his MSc degree in Embedded Systems. He completed his thesis in the Robotics and Mechatronics Group at the University of Twente, The Netherlands. His thesis, "Automatic Segmentation and 3D Reconstruction of Liver and Tumor," was supervised by Dr. Ir. M. Abayazid.

After completing his MSc, he was offered a Ph.D. position in the Robotics and Mechatronics Group at the University of Twente. Since December 2018, he has been working on the "MRI Guided Irreversible Electroporation" project, which is supervised by Prof. Dr. J.J. Fütterer and Dr. Ir. M. Abayazid. His research interests include developing computational models to predict tumor ablation outcomes and designing medical robotics for tumor treatment.

During his studies, he was involved in various student associations, including the Indonesian Student Association in Enschede (PPIE) and UT Muslims. He also actively participated in activities with the Muslim Society in Indonesia Muslims Enschede Association (IMEA). In his free time, he enjoys playing badminton, taking photographs, cycling, and walking in nature.

Irreversible Electroporation:

Maximizing Treatment Efficacy Through Optimization Strategies and Robotic Assistance

Girindra Wardhana

This thesis proposes the use of computational models and robotic systems to enhance the effectiveness of irreversible electroporation (IRE) treatment for tumors. IRE is a non-thermal ablation technique that selectively destroys tumor cells while preserving the surrounding tissue. The computational models investigate the effects of pulse parameters and electrode configurations on ablation and thermal damage, and determine the optimal parameters for treatment. To improve simulation results, an automatic segmentation method utilizing deep learning is proposed to accurately segment tissue shapes for model simulation. Subsequently, robotic tools are employed to improve electrode placement accuracy, resulting in better treatment efficacy. Together, these advancements have the potential to enhance IRE treatment planning and ultimately lead to better patient outcomes.

ISBN: 978-90-365-5674-3

DOI: 10.3990/1.9789036556750

UNIVERSITY
OF TWENTE.

